Towards Smart THz Integration Leveraging Silicon Passive Functions

Abdu Subahan Mohammed

PHD THESIS

To obtain the degree of doctor in **Micro and Nanotechnologies, acoustics and telecommunications**

Specialization: Electronics and photonics

From the University of Lille

ENGSYS doctoral school

Abdu Subahan MOHAMMED

Towards Smart THz Integration Leveraging Silicon Passive Functions

Prepared at IEMN, THz Photonics group
Defended on July 8, 2024

Jury:

Reviewers:	Pr. Anne-Laure. Billabert	CNAM – Esycom
	Pr.Olivier Lafond	Université de Rennes -IETR
Thesis Director:	Pr. Guillaume Ducournau	IEMN, University of Lille
Thesis Co-director:	Dr. Marc Faucher, CNRS Research Director	IEMN, University of Lille
Examinators:	Stéphane Blin, Lecturer	University of Montpellier – IES
	Pr.Gaëtan Lévêque	IEMN, University of Lille
Guests	Pascal Szriftgiser, CNRS Research Director	PhLAM, University of Lille
	Alberto Amo, CNRS Research Director	PhLAM, University of Lille

THÈSE DE DOCTORAT

Pour obtenir le grade de docteur en **Micro et Nanotechnologies, acoustique et télécommunications**

Spécialisation : Electronique et photonique

De l'Université de Lille

ENGSYS école doctorale

Abdu Subahan MOHAMMED

Vers une intégration intelligente THz exploitant les fonctions passives du silicium

Préparé à l'IEMN, groupe THz Photonics
Soutenue le 8 juillet 2024

Jury:

Rapporteurs :	Pr.Anne-Laure Billabert	CNAM– Esycom
	Pr.Olivier Lafond	Université de Rennes-IETR
Directeur de thèse :	Pr. Guillaume Ducournau	IEMN, Université de Lille
Co-directeur de thèse:	Dr Marc Faucher, directeur de recherche CNRS	IEMN, Université de Lille
Examinateurs :	Stéphane Blin, Maître de conférences	Université de Montpellier – IES
	Pr. Gaëtan Lévêque	IEMN, Université de Lille
Invités:	Pascal Szriftgiser, directeur de recherche CNRS	PhLAM, Université de Lille
	Alberto Amo, directeur de recherche CNRS	PhLAM, Université de Lille

To my parents
Mohammed and Hameeda

Acknowledgement

I want to thank my supervisors, Professor Guillaume Ducournau, and all the folks in Team TOPOTERA for their amazing support and guidance during my PhD journey. Professor Ducournau was always there to help with any scientific or technical problems, right from day one. He made the environment great for learning and teamwork, teaching me a lot about research and how to be a sincere and hardworking researcher. He's been a big inspiration to me.

I'm really thankful to Team TOPOTERA, especially Alberto Amo, Gaetan, Pascal, and Yan Pennec, for letting me be part of the project and helping me understand the theory behind my work. They were patient with my questions and gave me really helpful feedback on my dissertation. Also, big thanks to Co-Professor Marc Faucher for showing me the ropes in the cleanroom. His focus on understanding cleanroom processes well has been super important for getting good results.

I owe a lot to my colleagues too, especially Soukaina Bensalk and Edouard, for their support and teaching during the fabrication process.

Being part of the Marie Curie Training Network was a great experience. Thanks to Guillaume for giving me that chance. The training workshops and conferences organized by TERAOPTICS were awesome, and I'm grateful to Andreas Stohr, Guillaume, and all the professors involved for getting me involved to create such a good project. Huge thanks to our Project Coordinator, Andreas Kelin, for being such a great friend and supporter.

Shoutout to my fellow Co-ESRs for making our workshop days so memorable. Thanks to Ezgi, Aritrio, Surya, Shuya, Ashish, Krishna, Kalliopi, Javier, Faisal, Inigo, and Yimaz for their support and friendship. Aritrio, in particular, made my time at IEMN really enjoyable and helped me a lot during our IEMN and TERAOPTICS days. His guidance was crucial in getting me started in THz photonics.

Lastly, I want to thank RAL Space, UK, for letting me work there for a while as a . Thanks to Peter Huggard, Himanshu, and Hui for teaching me HFSS and hosting me during my time there.

I thank my wife to supporting me and bearing me all in our companionship. You are always the best. I specially thank you for resigning an excellent job for us and coming to me and creating a beautiful life in Belgium. I love you.

My father and My Mother I dedicate my work to you. I won't be here if you did not support me. I truly believe that your prayers are the reason I'm now. My brothers for being my brothers. In my family there are so many motivated me, My uncles, Grandparents I thank for the memories with you. Also, Thanks to all the past experiences nurturing me.

Finally, Thanks to almighty for everything. الحمد لله.

Résumé et contenu de la thèse

La réalisation de systèmes intégrés, à faible perte et efficaces pour des applications consommatrices en données telles que la réalité augmentée et virtuelle, nécessite des circuits photoniques intégrés sur puce, qui présentent un grand potentiel pour les technologies de l'information et de la communication avancées, y compris les réseaux sans fil 6G et les systèmes de communication intra et inter-puces. Une plateforme prometteuse pour réaliser ces systèmes intégrés est celle des guides topologiques, ou guides « VPCs », pour Valley Photonics Crystal. Les VPCs permettent la construction d'interfaces topologiques, qui permettent la propagation des ondes E.M. avec des pertes minimales et une rétrodiffusion réduite grâce à des modes de bord unidirectionnels. Les interfaces topologiques interfaciales et le degré de protection topologique expérimenté par ces modes de bord robustes constituent une perspective relativement nouvelle qui mérite d'être explorée.

De plus, la demande croissante de débits de données pour des applications telles que la réalité augmentée et virtuelle nécessite l'exploration de fréquences au-delà de la bande conventionnelle des 300 GHz. De plus, la bande des 300 GHz qui offre une largeur de bande d'environ 120 GHz, atteindre le Tbit/s est difficile sauf à recourir à des modulations très complexes. En raison de la largeur de bande importante disponible autour de la fenêtre atmosphérique des 650 GHz, la bande des 600~700 GHz a attiré une attention significative. Dans ces travaux, sont conçus, fabriqués et caractérisés expérimentalement des guides VPC qui démontrent plusieurs fonctions passives THz telles que des guides d'ondes et des guides d'ondes courbés, des filtres et des résonateurs pour la plage de fréquences de 600 GHz.

En utilisant différents designs de résonateurs (variations des géométries de trous d'air appropriées), nous introduisons des variations dans la protection topologique pour les dispositifs fonctionnels passifs. Nous montrons que la rupture partielle de la protection topologique peut être un atout pour la conception de fonctionnalités passives sur puce. Nous nous concentrons sur différentes géométries de trous d'air appropriées pour les cellules unitaires VPC. Pour vérifier expérimentalement la mise à l'échelle de la protection topologique, nous démontrons les performances de résonateurs topologiques térahertz (THz) en anneau et de résonateurs à double cavité THz conçus pour fonctionner à 600 GHz. Cette démonstration montre comment la mise à l'échelle de la protection topologique peut être

réalisée en utilisant une combinaison de géométrie de trous d'air et de degrés de liberté interfaciaux, offrant un réglage fonctionnel des dispositifs au niveau de la puce.

Nous avons également proposé dans ces travaux des filtres topologiques pour la bande des 600 GHz. Après la conception et la fabrication sur SOI, le filtre a été entièrement caractérisé et validé à l'intérieur d'un système de communication dans la bande 600 GHz. Nous montrons expérimentalement que jusqu'à 3x40 Gbit/s peuvent être manipulés dans la structure proposée. L'utilisation d'une approche topologique pour la bande des 600 GHz semble prometteuse pour les futurs systèmes de communication de la bande des 600 GHz.

Summary and thesis content

The realization of integrated, low-loss, and efficient systems for data-intensive applications such as augmented and virtual reality requires on-chip integrated photonic circuits, which have great potential for advanced information and communication technologies, including 6G wireless networks and intra- and inter-chip communication systems. A promising platform for achieving this revolution is Valley Photonic Crystals (VPCs). VPCs enable the construction of topological interfaces, which facilitate the propagation of light with minimal losses and backscattering through unidirectional edge modes. Interfacial topological interfaces and the degree of topological protection experienced by these robust edge modes is a relatively new perspective worth exploring. The ever-increasing demand for faster data rates in data-intensive applications like augmented and virtual reality necessitates the exploration of frequencies beyond the conventional 300 GHz band. Moreover, the 300 GHz band offers approximately 120 GHz bandwidth, making it difficult to pave the way towards Tbit/s. Due to the large bandwidth available around the 650 GHz atmospheric window, the 600~700 GHz band has garnered significant attention. In our thesis, we successfully designed simulated fabricated and experimentally demonstrated several THz passive functions like waveguides, and bent waveguides, Filters, resonators for the 600GHz frequency range.

Using the different designs in resonators by considering different interfacial designs and suitable air-hole geometries, we introduce variations in topological protection for passive functional devices. We show that the partial breakup of topological protection can be an asset for the design of on-chip passive functionalities. We focus on bearded and zigzag junctions and appropriate air hole geometries for VPC unit cells. To experimentally verify the scalability of topological protection, we demonstrate the performance of terahertz (THz) topological ring resonators and THz double cavity resonators designed for operation in the 600 GHz frequency region. This demonstration showcases how the scaling of topological protection can be achieved by utilizing a combination of air hole geometry and interfacial degrees of freedom, providing functional tuning of devices at the chip level.

We also proposed in this thesis topological filters for the 600 GHz band. After design and fabrication on SOI, the filter was fully characterized and validated inside a 600 GHz communication system. We experimentally show that up to 3x40 Gbit/s can be manipulated in

the proposed structure. The use of a topology approach for the 600 GHz band seems to be promising for the future.

Table of contents

List of abbreviations

1D - One-Dimensional
2D - Two-Dimensional
3D - Three-Dimensional
6G - Sixth Generation
BD - Bearded
BZ - Brillouin Zone
CW - Continuous Wave
DRIE - Deep Reactive Ion Etching
EIA - Electronic Industries Alliance Standards
EM - Electromagnetic
EO - Electro-optic
GMM - Guided Metallic Media
HR-Si - High-resistivity Silicon
IEEE - Institute of Electrical and Electronics Engineers
IR - Infrared
IR - IR Infrared
MMW - Millimeter Wave
NDC - Negative Differential Conductance
PBG - Photonic Bandgap
PC - Photoconductive
PEEK - Polyether Ether Ketone
PhC - Photonic Crystal
PML - Perfectly Matched Layers
PTIs - Photonic Topological Insulators
QHE - Quantum Hall Effect
RTD - Resonant Tunneling Diode
SB - Supporting Beams
SIIG - Substrate Integrated Image Guides
Si - Silicon
TEM - Transverse Electromagnetic
TE - Transverse Electric
THz - Terahertz
THz-TDS - THz Time Domain Spectroscopy
TIR - Total Internal Reflection
TM - Transverse Magnetic
TPEWs - Topologically Protected Edge Waves
TRS - Time Reversal Symmetry
TW-UTC-PDs - Travelling-wave Uni-travelling-carrier Photodiodes
UTC-PDs - Uni-travelling-carrier Photodiodes
VPCs - Valley Photonic Crystals
WR - Rectangular Waveguides
YIG - Yttrium-Iron-Garnet
ZZ - Zigzag

List of Figures

List of tables

Chapter I:

Introduction

I.1 Introduction to Terahertz (THz) waves

Various frequencies are spaced along the extensively used electromagnetic spectrum, encompassing microwaves, infrared radiations, visible light, ultraviolet, and X-rays. Terahertz (THz) radiation occupies the space between microwave and infrared frequencies (Fig I.1). These waves can be characterized by their wavelength (mm, µm, nm) primarily in the photonic realm (infrared (IR), visible), wavenumber (cm^{-1}) for spectroscopy, frequency (Hz) for electrical engineering/telecommunications, and occasionally by energy (eV or Joules). Within the electromagnetic spectrum, radiation at 1 THz represents a period of 1 ps, a wavelength of 300 µm, a wave number of 33 cm^{-1}, a photon energy of 4.1 meV, and an equivalent temperature of 47.6 K.

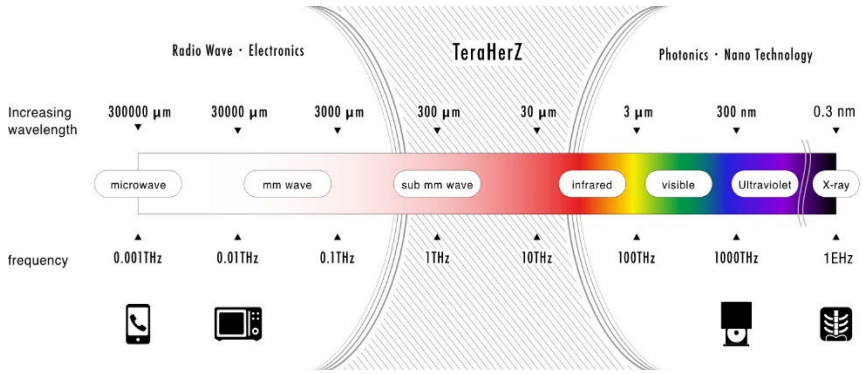

Figure I.1 : Electromagnetic Spectrum [1]

Much like visible light capturing a photograph, radio waves can be used to carry and transmit sound, and X-rays revealing shapes within the human body, terahertz waves (also known as T-rays) also feature the ability to generate images and convey information. An illustration of Electromagnetic radiation showing THz radiation in the mid is shown in Fig I.1.There are numerous sources of THz radiation around us, such as cosmic background radiation and blackbody radiation from objects at any temperature (some examples are given in Figure I.2). However, most of these natural sources are incoherent and not very useful for all applications. Until recently, the THz portion of the electromagnetic spectrum was known as the 'THz gap' because there were no suitable emitters to send out controlled THz signals and no efficient detectors to collect them and record information for sensing or any other physical measurements using THz. Now with the development of such technology, the THz portion of

the spectrum is becoming easier to reach and useful for practical applications. At the end of the 19th century, scientists discovered electromagnetic waves in the THz frequency range.

Initially, they referred to it as obscure radiation, as described in Nicholas' study [3]. The term "Terahertz" appeared in the first scientific publications 80 years later [4]-[7]. Due to the limited scientific discoveries in this domain and the initial difficulty in producing efficient passive and active components operating at these frequencies, this frequency range was considered a "gap" in the spectrum. However, researchers made tremendous efforts over the past decades to fill this gap [8-25] owing to the unique properties of THz waves and their multiple applications in several fields.

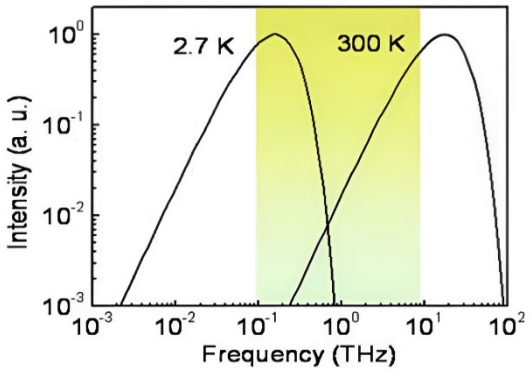

Figure I.2: Cosmic background radiation and blackbody radiation from room temperature object. Shadow area indicates THz band [2].

The non-ionizing property of THz waves due to their low photon energy (0.41-41.5 meV) and their capability to penetrate different types of materials, including some opaque ones in the visible range, make them useful for medicine, biosensors, and imaging [8]-[11]. Furthermore, the presence of several molecules with vibrational and rotational transitions in this frequency region allows THz waves to act as a unique spectroscopic tool [12]-[16]. Apart from these, several other applications exist where THz waves play a crucial role, such as food examination and quality control [17]-[20], communication [21], [22], and astronomy [23]-[25]. There has been a lot of interest in this THz band, for the development of the next generation of cellular networks - 6G. The reason for this is the high potential benefits of the large spectral resources available in this band. The research on 6G technologies has consistently suggested the use of carriers at THz frequencies [26]-[30]. For many of these applications, the availability of efficient passive and active THz components such as sensors, sources, detectors, waveguides, resonators, etc., is to be essentially developed. The primary objective of this doctoral research is to devise and implement innovative techniques for developing highly integrated photonic circuits in the higher unexplored THz frequency range beyond the 300 GHz central frequency

range, employing high-resistivity silicon (HR-Si) platforms. Our research aims to construct passive functions within photonic crystals based on silicon, utilizing topological degrees of freedom. These advanced photonic circuits and components have the potential to accelerate the emerging 6G and beyond technology in the coming years. Before delving into our background studies and proposed designs, it is important to introduce the methods employed to generate and detect terahertz frequencies and understand their manipulation in a terahertz electronics/photonics laboratory.

I.2 Methods to Generate and Detect THz Waves

Terahertz (THz) radiation lies in between the microwave and far-infrared regions and has the advantage of the use of either electronics or optics approaches, or a combination of both, for its generation and detection [31,32]. Two general categories of optical THz radiation generation exist. The first involves producing an ultrafast photocurrent in a photoconductive switch or semiconductor [33, 34]. The second category employs nonlinear optical effects, such as optical rectification [35, 36], difference-frequency generation [37], or optical parametric oscillation [38], to generate THz waves. Based on the lasers utilized to generate THz signals, these technologies can also be classified into pulsed and continuous wave (CW) THz technologies. Pulsed THz radiation offers wide bandwidth and fast measurement capabilities. Its frequency resolution, however, is relatively limited, typically in the range of several GHz using typical ns-level delay lines. CW THz is generated by mixing two laser beams with varying frequencies, providing exact frequency tuning, high resolution, and greater suitability for high-speed THz communication.

A typical technique for generating and detecting pulsed THz waves is through a pump and probe setup, as depicted in Figure I.3 In this method, a femtosecond (fs) laser beam is split into two parts following two different paths, one for the pump and the second for the probing beam. The pump beam generates the THz pulse, whereas the probe beam samples the receiver within a specific relative (to the source) time delay and thus enables to obtain the pulse profile as pump and probe are periodic. Detecting of the THz field is performed by mixing the probe pulse with the THz field, in other words, the receiver is realizing a time-domain sampling of the incoming THz pulse, the sample being defined by the time of arrival of the optical probe

pulse on the receiver. A mechanical delay line is utilized to adjust the relative time delay between the THz pulse and the probe pulse, from which the THz waveform can be obtained by scanning this time delay. To enhance sensitivity, the pump beam is modulated by an optical chopper, and the THz-induced modulation on the probe beam is extracted by a lock-in amplifier. The pulse information obtained in the time domain is transformed into the frequency domain using the Fourier transform, from which spectral information can be derived.

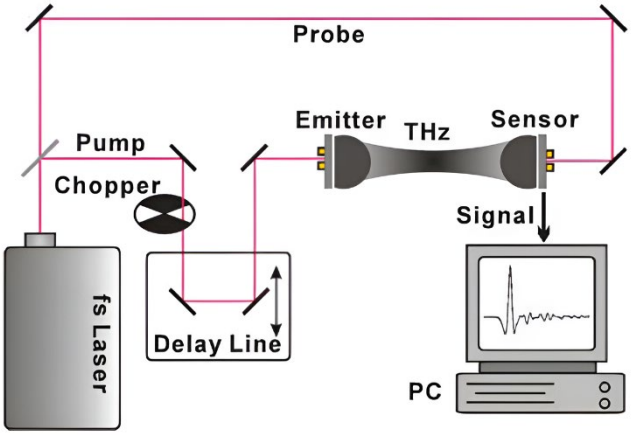

Figure I.3: Pulsed THz wave generation and detection setup [2]

I.2.1 Photoconductive Antenna

The photoconductive (PC) antenna is a widely utilized component for both the generation and detection of terahertz (THz) pulses. Its operation relies on the transient generation of photocarriers induced by ultrafast laser pulses, these photo-induced carriers being further creating a THz wave, thanks to an antenna connected to the PC. Illustrated in Figure I.4 is the schematic representation of a PC antenna and the underlying principle of THz pulse generation employing such an an

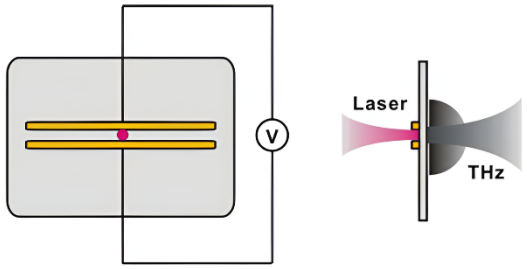

Figure I.4: PC antenna and THz emission from PC antenna [2]

Comprising two metal electrodes deposited on a semi-insulating semiconductor substrate with a gap between them, the PC antenna operates by applying a voltage across these electrodes. As the substrate is semi-insulating, electric energy becomes stored within the gap region.

Ultrafast laser pulses serve as transient switches, effectively releasing this stored electric energy in the form of THz pulses.

The generated free carriers, driven by the bias field across the gap, result in photocurrent. Due to the typically higher mobility of electrons compared to holes, the contribution of holes is often negligible. The current density generated $J(t)$ can be described as [2],

$$J(t) = N(t)e\mu E_b \tag{I.1}$$

where N is the density of photocarriers, e denotes the elementary charge, μ is the mobility of electrons, and E_b is the bias electric field. The photocarrier density N is a function of time, which is determined by the laser pulse shape and the carrier lifetime. Since the photocurrent varies in time, it generates an electromagnetic pulse, whose electric field is approximately [2]

$$E_{\mathrm{THz}} = \frac{1}{4\pi\epsilon_0}\left(\frac{A}{c^2 z}\right)\frac{\partial J(t)}{\partial t}$$

$$= \frac{Ae}{4\pi\epsilon_0 c^2 z}\frac{\partial N(t)}{\partial t}\mu E_b \tag{I.2}$$

where A is the area in the gap illuminated by the laser light, ε_0 is the vacuum permittivity,c is the speed in a vacuum, and z is the distance between the field point and the THz source. To derive Equation (I.2), the field point is assumed located at normal to the PC antenna, and the distance between the field point and the source is much larger than the dimension of the PC antenna.

I.2.2 Generation of THz Continuous Waves

One of the most popular methods to generate continuous wave (CW) terahertz (THz) radiation currently is by using photomixing technique, which entails mixing two lasers with closely spaced emission frequencies in an ultrafast semiconductor photodetector or PC antenna to generate a photocurrent with a frequency equal to their frequency difference in the THz region [39]. This photocurrent is then used to drive an antenna, resulting in the emission of THz waves.

Photo mixing allows for easy tuning of the frequency of THz waves by adjusting the spacing of the lasers, and suitable photomixer devices include PC antennas, uni-travelling-carrier photodiodes (UTC-PDs), travelling-wave uni-travelling-carrier photodiodes (TW-UTC-PDs), or n-i-p-n-i-p superlattice photo mixers [41-45]. The UTC-PD is a common device used in current THz wireless communication systems, and the maximum CW output power achieved is 10.9 μW at 1.04 THz, with good linearity, pumping by laser diodes operating at 1.55 μm [46]. The efficiency of the UTC-PD is typically at frequencies up to 1.5 THz [46]. One of the latest work compares the performance of two typical commercially available photomixers: UTC-PD and PIN-PD [47]. The UTC-PD emits ~100 μW at 250 GHz, and the PIN-PD produces 30 μW [47]. Apart from the PD or PC antenna, another photonics-based way of generating CW THz radiation is to exploit a nonlinear medium in which incident electromagnetic waves undergo nonlinear frequency conversion [14]. Tunable lasers and photomixers are important for CW THz generation, and the advantage of CW THz generation over broadband THz pulse generation is its simple optical source. Only two single-mode CW lasers are needed, with at least one of them being tunable. Especially at the telecom wavelength of 1.55 um, a large variety of compact, tunable, and low-cost semiconductor lasers are already available.

I.2.3 Detection of THz Continuous Waves

There are two types of techniques used for detecting THz waves: coherent and incoherent. The main difference between these two techniques is that coherent detection measures both the amplitude and phase of the field, while incoherent detection only measures the intensity. Coherent detection techniques are closely linked with generation techniques, as they both share the same mechanisms and components. Coherent optically-driven THz techniques can rely on the same light source for both generation and detection. THz detection can be divided into pulsed and continuous wave detection. To measure the actual electric field of broadband THz pulses in the time domain, sensing can be done either with a PC antenna or electro-optic (EO) sampling techniques [48]. When there is no bias field present, a THz field induces a current in the PC gap when an optical probe pulse injects photocarriers. The photocurrent induced is proportional to the amplitude of the THz field. To map out the shape of the THz pulse in the time domain, the photocurrent is measured while the time delay between the THz pulse and optical probe is varied. On the other hand, EO sampling techniques depend on the Pockels effect, on which a THz field induces a refractive index change proportional to the field

amplitude. The entire waveform is then determined by an optical probe that measures the field-induced birefringence as a function of the relative time delay between the THz and optical pulses. The basic experimental setup for generating and detecting THz pulses using a femtosecond laser is similar to the pump-probe technique. Figure I.5 shows the schematic of the typical setup. THz time domain Spectroscopy (THz-TDS) works on the principle of a femtosecond laser producing an optical-pulse train. The optical beam is divided into two paths. One part illuminates the THz emitter, which could be a PC antenna or nonlinear crystal, where the THz pulses are generated.

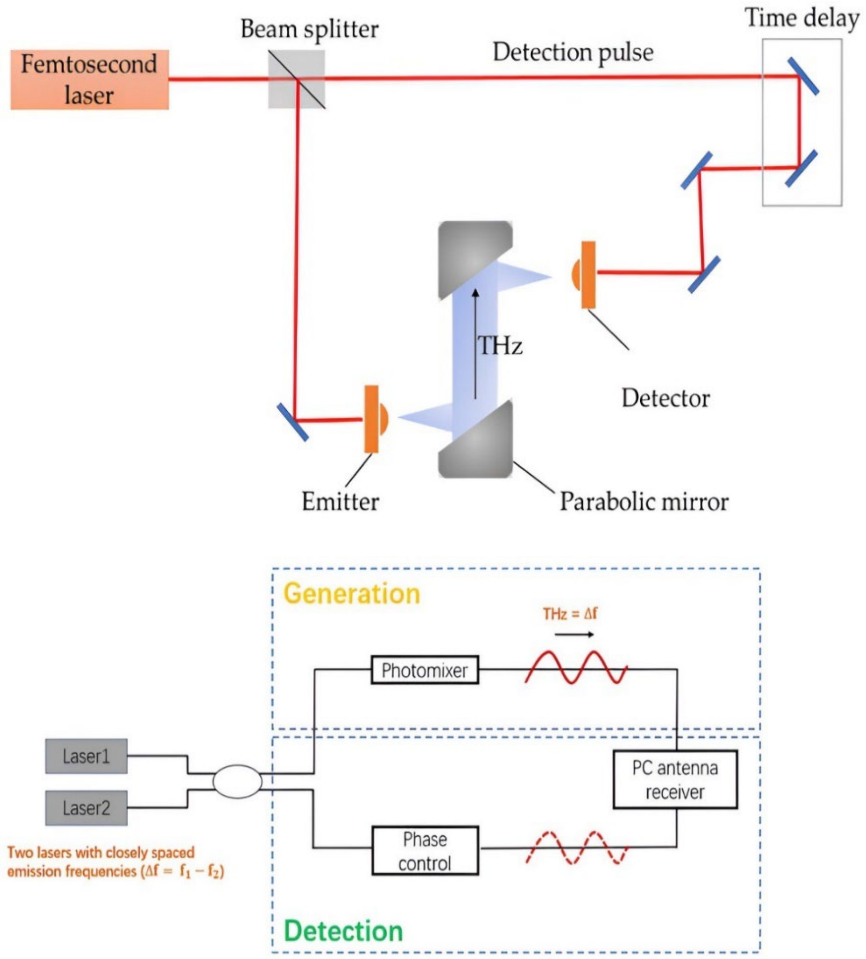

Figure I.5: The figure shows a schematic representation of the common setups used for generating and detecting THz pulses (top) and CW THz waves (bottom) using femtosecond optical pulses [53].

These pulses then propagate in free space and are focused onto a probe-pulse-gated detector, such as a PC antenna or an EO crystal. The other part of the pulse is also directed toward the detector after passing through a time-delay stage. A 10-fs-laser allows the components of

waves exceeding a frequency of 100 THz to be detected by either EO sampling [49] or a PC antenna [50]. In this ultra-band coherent detection system, the scanning range and speed of the time-delay stage are crucial. Compared to the THz-TDS system, the CW THz system based on photonics can take advantage of low-cost, compact, and well-established fiber-optic telecom technologies. In general, CW THz systems exhibit high-resolution frequency selectivity across a wide frequency range [48–50]. These systems use coherent detection techniques that utilize a PC antenna or EO sampling receiver to measure CW THz radiation. The commonly used coherent detection scheme for CW THz systems based on a PC antenna is shown in Figure I.5. The photocurrent produced in this scheme shows a sinusoidal dependence on the relative phase between the optical beat and the THz radiation.

Different types of electronic detectors, including Schottky diodes, which operate through rectification mechanisms of electromagnetic signals, can also serve in incoherent detection scenarios [51,52]. These rectification-based detectors are known for their speed, primarily constrained by parasitic elements and readout electronics. Consequently, they find extensive application due to their fast reponse time (GaAs Schotkky diodes can have cutt-off frequencies beyond several THz).

I.3 THz Integrated Photonics

As previously mentioned in section I.1, the THz frequency range holds immense potential for various applications such as communication, medicine, imaging, and astronomy, among others. To enable such applications, THz components such as sources, detectors, waveguides, cavities, and modulators are necessary. Therefore, it is essential to develop components, devices, and integrated circuits that operate within this frequency range to fully realize the potential of THz technology. Since THz frequencies bridge the gap between microwave and optical frequencies, electronics and photonics can be replicated to an extent in this frequency region. In this section, we intend to explore waveguides and generations of integrated systems for the THz range. This includes metallic hollow waveguides, planar transmission lines, dielectric THz fibers, photonic crystal waveguides, High resistivity silicon-based waveguides, and functions. As per [69], first and second generations of silicon-based THz integrated photonics, and newly emerged waveguides and functions based on topological photonics. We look into the performances of each waveguide in terms of key metrics including bandwidth, loss, and integrability for the realization of THz-range integrated components and systems.

I.3.1. THz waveguides Introduction

Waveguides play a crucial role in advancing the THz field. They can help solve the challenges of THz energy transfer and spectroscopy. This section will cover the evolution of THz waveguides, from the initial times of bulky metallic ones to the latest advanced silicon-based highly integrable THz waveguides, systems highlighting significant breakthroughs along the way. In integrated circuits, the transmission of electromagnetic (EM) waves between passive and active components requires low-loss waveguides. These waveguides are also crucial in ensuring the transition from off-chip to on-chip.

I.3.1.1 Metallic THz rectangular waveguide

Metallic waveguides are commonly used in high-frequency guided-wave systems, especially in the microwave band. They are preferred due to their ability to support an efficient waveguide: limit radiation/losses and no dielectric loss (hollow-core waveguide) in comparison with transmission lines. However, hollow metallic waveguides with only one conductor lack a transverse electromagnetic (TEM) mode with a zero-cutoff frequency. This restricts the range of possible modes to transverse electric (TE) and transverse magnetic (TM) modes with non-zero cutoff frequencies, which depend on the waveguide's transverse dimensions. Figure I.6 shows the cross-section of a rectangular metallic waveguide.

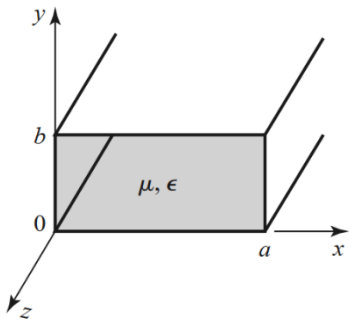

Figure I.6: Cross-section view of a rectangular waveguide.

Single-mode transmission is only feasible for frequencies higher than the cutoff frequency of the dominant mode and lower than that of the next higher mode.

Therefore, metallic waveguides are suitable for the microwave band in practical applications, particularly in the centimeter and millimeter wave bands.

Metallic hollow waveguides have also been scaled with smaller dimensions to operate in the THz frequency band. For a long time, metallic waveguides such as hollow waveguides have been a standard for interconnecting with external power sources, testing, and packaging for the THz range [54-56]. However, their physical size in this range is significantly reduced, making fabrication highly challenging due to the extreme accuracy required for manufacturing. Additionally, the physical size of metallic waveguides in the THz range poses difficulties in interconnecting with planar components of a different scale, often leading to a modal mismatch at the interface with the hollow waveguide.

The ohmic loss caused by the relatively small skin depth of metal at high frequencies defined by:

$$\delta_s = \frac{2}{\sqrt{\omega\mu(\omega)\sigma}} \tag{I.3}$$

where $\omega = 2\pi f$ is the wave angular frequency, $\mu(\omega)$ the permeability (usually μ_0), and σ metal conductivity. The roughness of the internal surfaces of the waveguide is also contributing to the losses. The cut-off frequency of a rectangular metallic waveguide is related to its cross-section dimensions via the relation below:

$$f_{cmn} = c\sqrt{\left(\frac{m}{2a}\right)^2 + \left(\frac{n}{2b}\right)^2} \tag{I.4}$$

where $c = 3 \times 10^8\ m/s$ is the speed of light, a, and b the horizontal and vertical dimensions of the guiding channel, and m, n the modes indexes. For a single-mode operation at high frequencies, waveguides with very small dimensions are necessary. These small dimensions create the fabrication of these waveguides a complex process and complicated assembly. The cut-off frequency is the minimum frequency beyond which electromagnetic waves can propagate within the waveguide. As the frequency increases, the skin depth decreases, indicating that electromagnetic waves penetrate less deeply into the metallic waveguide. The cut-off frequency is influenced by the waveguide's dimensions, including its width and height, and this relationship helps characterize the waveguide's ability to support specific modes of electromagnetic wave propagation based on its geometry.

In practical terms, engineers use this relationship to design and optimize rectangular metallic waveguides for specific frequency ranges, ensuring efficient waveguide performance in guiding electromagnetic signals. Despite the inherent complexity in fabrication, these

waveguides find practical applications in commercial settings for frequencies up to 3 THz [58].,Figure I.7(b) gives the view of an example [57] of WR-1.5 MWG, which covers the 500-750 GHz frequency range. The reported propagation losses for this WR-1.5 waveguide range from 0.73 to 1.05 dB/cm. However, the substantial size of these commercially available waveguides precludes their integration into compact integrated circuits. In response to this limitation, a miniaturized MWG was proposed by [59] and [60], leveraging the deep reactive ion etching (DRIE) technique. This innovative approach involves etching the waveguide channel inside a silicon wafer using DRIE and subsequently adding a metal layer through sputter coating. Figure I.7(a) provides both a photograph and a schematic of the micromachined WR-1.5 MWG. Despite these advancements, the micromachined designs reported by [59] and [60] still exhibit quite high ohmic losses, even with the utilization of thin reflective metal layers. The measured propagation loss for these micromachined waveguides is 1.5 dB/cm at 570 GHz and 4 dB/cm at 380 GHz.

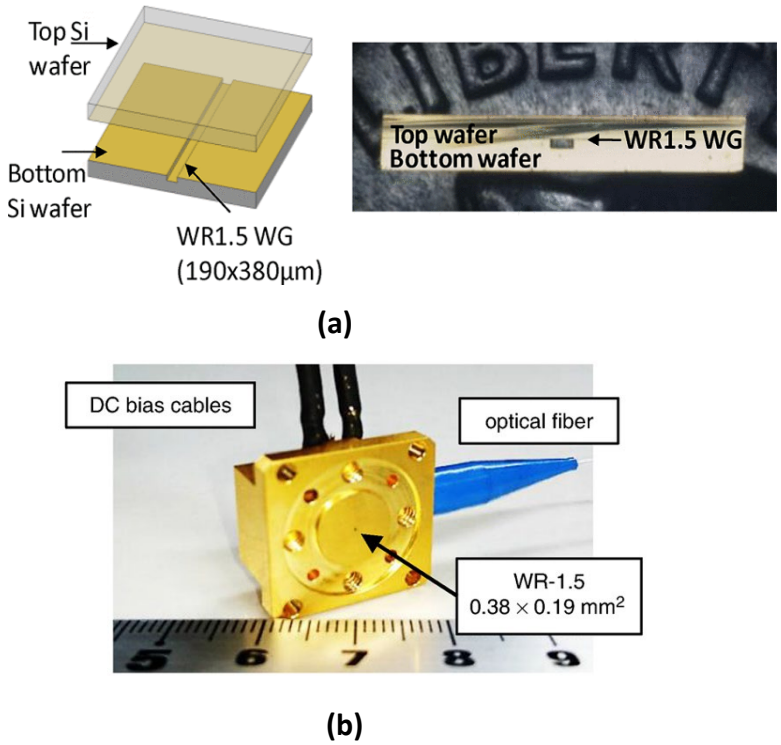

Figure I.7 : (a) Micromachined metallic WR-1.5 waveguide [58], (b) Example of WR-1.5 waveguide [57]

These findings underscore the ongoing challenges in achieving both miniaturization and low propagation losses in microwave waveguide designs, despite notable advancements in fabrication techniques. The references [57], [58], and [59] provide critical insights into the

development and evaluation of these waveguides, contributing to the broader understanding of high-frequency applications in integrated circuits.

Various organizations, such as IEEE, MIL, EIA, and IEC, publish waveguide standards to establish a connection between the size and shape of a waveguide and to generalize its dimensions globally. These standards mainly concentrate on the waveguide dimensions that correspond to specific shapes along with the interfaces to be used for each standard waveguide and frequency band. The primary waveguide standards are IEEE standards and IEC standards, while manufacturers also use Electronic Industries Alliance Standards (EIA) and United States Military (MIL) standards. Alphanumeric letters are utilized in waveguide standards for identifying the waveguide size. The standard designation usually comprises two letters that signify the type of waveguide, followed by numerals indicating the waveguide width. The letters used in designators correspond to the series of standards associated with a specific waveguide shape. The two commonly used series of waveguide standards are "WG" and "WR" which refer to waveguide transmission line and waveguide rectangular, respectively.

The WR series of waveguide standards provide detailed information on dimensions and other crucial parameters, such as cut-off frequency and propagation modes, associated with rectangular waveguides. Within the WR standards, valuable insights are offered regarding frequency bands and the internal dimensions of rectangular waveguides.

Waveguide Frequency Bands with Internal Dimensions		
Waveguide Standard	Frequency range in GHz	Internal dimensions in mm
WR-4	170-260	1.0922 x 0.5461
WR-3	220-325	0.8636 x 0.4318
WR-2	325-500	0.508 x 0.254
WR-1.5	500-750	0.38 x 0.19

Table I.1: Frequency bands and Waveguide standards

Additionally, the WR series facilitates the selection of an equivalent double rigid rectangular waveguide, known as the WG equivalent, for any standard rectangular waveguide. Table I.1 shows the WR the frequency bands and the waveguide standard we use in during the course of our experiments.

I.3.1.2 Dielectric Coated Metallic waveguides

Hollow-core metallic waveguides encounter heightened ohmic losses in the THz range, which can be mitigated by incorporating a dielectric coating on the inner metallic waveguide walls, as documented in [56, 62]. The reported propagation loss of 0.01 cm^{-1} was successfully achieved according to [56]. The dielectric coating facilitates a gradual vanishing of electric fields at the interface with the wall. In contrast, for metallic rectangular and circular waveguides, the fields penetrate the metal wall, leading to absorption. Further reduction of loss involves optimizing the dielectric cladding thickness, achieved by decreasing the inner diameter. This optimization enables modal matching with THz pulses, enhancing the coupling between the dominant mode and propagating THz waves [63]. The increase in coupling efficiency with the dominant mode is balanced by reduced efficiency with higher-order modes. This eventually results in the suppression of higher modes, leading to a desirable single-mode operation ideal for waveguides.

I.3.1.3 An Overview of Several Other Waveguides

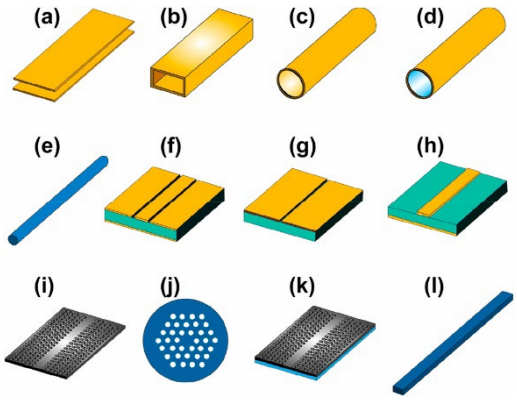

Figure I.8: Low-loss waveguides for the THz range, (a) parallel plates waveguide, (b) metallic rectangular waveguide, (c) metallic circular waveguide, (d) circular waveguide with dielectric coating, (e) polymer fiber, (f) coplanar showing substrate in aquamarine color, (g) slot line, (h) stripline, (i) photonic crystal waveguide, (j) photonic crystal fiber, (k) SIIG with dielectric substrate, (l) ribbon waveguide. The colors gray, yellow, and blue represent silicon metal, and low-index dielectric material, respectively. [69]

Polymer fibers, see Fig I.8 (e) share a circular profile with dielectric hollow waveguides but differ in diameter, being subwavelength, i.e., smaller than the operating wavelength. Waveguiding in polymer fiber involves radiation loss due to nonuniform diameter variations and material absorption, with a reported propagation loss as low as 0.01 cm^{-1} at 300 GHz [64].

Achieving a uniform diameter in the THz range for such fibers is particularly challenging, with diameters in the tens of microns scale for mid to higher THz frequencies. THz waveguides with a planar profile, including coplanar, microstrip, and stripline transmission lines, have been extensively utilized. However, their adoption for the THz range is limited due to high dispersion and attenuation [65]. Propagation loss for coplanar, microstrip, and stripline waveguides can be as high as 10 dB/cm, 15 dB/cm, and 6 dB/cm, respectively [66].

Photonic crystal waveguides, see Fig I.8(i), showcasing a planar profile for the THz range, distinguish themselves by lacking a substrate, thus suppressing substrate absorption loss. Strong in-plane confinement is achieved through the PBG effect, resulting in minimal leakage into the air and extremely low reported propagation losses [67-69]. The significance of photonic crystal waveguides, especially for THz integrated circuits, is extensively covered, including notable structures like photonic crystal fibers and substrate-integrated image guides (SIIG).

Reference	Waveguide Type	Frequency (GHz)	Propagation Loss (dB/cm)	Confinement Principle	Integrability
[63]	Parallel Plates Waveguide	100–4000	<0.3	GMM	No
[57]	Hollow Rectangular Waveguide	750–1100	1.92–1.35	GMM	No
[56]	Circular Coated Hollow Waveguide	–	0.01	GMM	No
[64]	Polymer Fiber	320–350	<0.01	TIR	Yes
[74]	Microstrip Line	Up to 1000	43.4	GMM	Yes
[75]	Coplanar Waveguide	Up to 1000	65	GMM	Yes
[76]	Slot Line	Up to 1200	26	GMM	Yes
[77]	Photonic Crystal	324–361	<0.1	PBG	Yes
[78]	Photonic Crystal Fiber	171–352	~18	PBG	Yes
[73]	Ribbon	100–140	0.087	TIR	No
[72]	SIIG	85–105	0.35	TIR	Yes

Table I.2: Performances of various THz waveguides.

Photonic crystal fibers, see Fig I.8 (j), that are like optical fibers with a photonic crystal core, exploit the PBG effect for guiding, dating back to early reports in 1996 [70] and proving efficient THz waveguiding [71]. SIIG structures, see Fig I.8(k), featuring a dielectric core and two low refractive index porous walls on each side of the core, demonstrate TIR as the guiding mechanism, reporting propagation losses as low as 0.35 dB/cm [72]. Ribbon waveguides, relying on TIR, have a simple structure comprising a high-index dielectric core such as a graphene core, with reported propagation losses of 0.087 dB/cm in the 100–130 GHz range

[73]. Illustrations are provided for these waveguides in Figure I.8 and Table I.2 briefly summarizes the performance of each of these waveguides.

In recent years, HR-Si has gained significant attention for THz applications due to its low absorption coefficient and large non-dispersive refractive index [79], [80]. The guiding channel for mm-waves can be created by bonding Si and glass together, which results in refractive index contrast. Ranjkesh et al. presented a design of Silicon-on-glass waveguides, shown in Figure I.9. The extracted propagation loss of this design was 0.63, 0.28, and 0.53 dB/cm for 55-65, 90-110, and 140-170 GHz bands, respectively [81]. However, beyond 400 GHz, the absorption of the glass substrate material increases dramatically, making it unsuitable for guiding purposes [80], [82]. To overcome this limitation, [83] proposed a layout where the glass is etched locally and the guiding layer is suspended by Silicon supporting beams (SB). A schematic of this suspended Si waveguide on a glass substrate is presented in Figure I.9(b). The suspended waveguide has an average loss of 0.54 dB/cm over the 440-550 GHz frequency band. The process is laborious, and the scattering losses increase due to roughness at the SB edges. Furthermore, bonding of HR-Si/Glass followed by glass etching steps is still required.

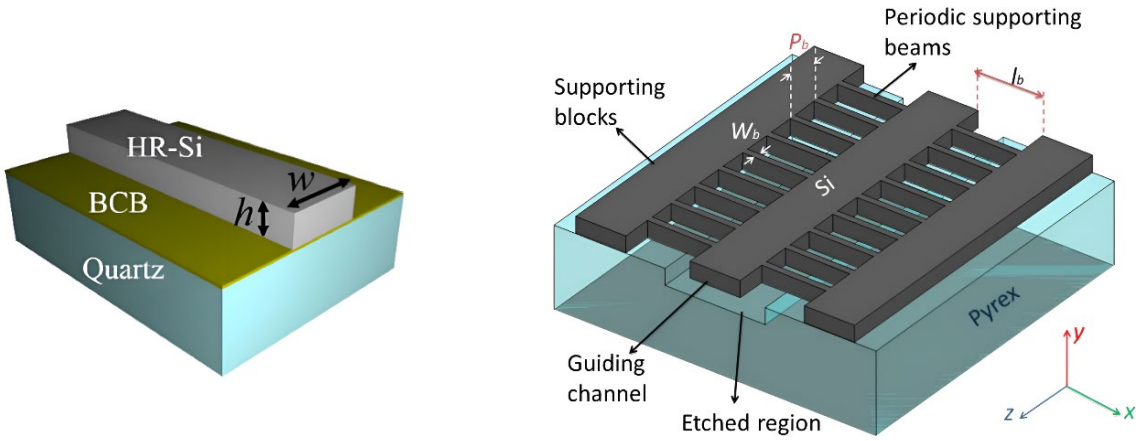

Figure I.9: Schematics of the different available designs of HR-Si waveguides. (a) silicon on glass waveguide [81], (b) silicon suspended waveguide [83].

I.3.1.4 Photonic Crystals

Photonic crystals are periodic structures that are designed to manipulate electromagnetic wave propagation, inspired by solid-state crystals controlling electronic waves. The periodic variation in the refractive index gives rise to a region of forbidden frequency known as the photonic band gap (PBG), resulting from interference in periodic materials. The term "photonic

band gap" was introduced by Eli Yablonovitch [84] in 1987 and encompasses 1D, 2D, and 3D structures. Lord Rayleigh had envisioned a 1D band gap back in 1887 [85]. While the experimental realization of a complete 3D PBG has been achieved in mmW structures [86], higher frequencies (THz, IR, visible) present challenges due to complex 3D fabrication techniques. However, 2D and 1D photonic crystal geometries, known as slab photonic crystals, have been extensively explored, featuring air hole etching. In the quest to generate, manipulate, and transmit THz waves, which possess extensive spectral bandwidth, researchers face challenges. To address this, they have turned to photonic crystal slabs, which are 2D structures made of semiconductor material and perforated holes that create a stop-band or PBG where transverse-electric (TE) fields are forbidden. The size of the bandgap is controlled by hole arrangements, allowing the creation of tailored photonic crystal waveguides. The concept of photonic crystals has evolved to engineer PBGs that block THz waves in specific frequency ranges. PBGs are instrumental in controlling and manipulating THz waves, as demonstrated by Fujita et al. who inhibited and redistributed spontaneous light emission in photonic crystal slabs [87-88].

Manipulating slab and vertical modes enables the control of spontaneous light emission. Kakimi et al. further showcased the trapping of THz waves in photonic crystal slabs using resonance states, with confinement dependent on material absorption [89]. Controlled absorption prevents wave leakage, showcasing another avenue for manipulating trapped THz waves. Photonic crystal slabs have emerged as a promising solution for THz integrated circuit components. Fabricating entire THz integrated circuit components on an all-Si platform from a single etch process reduces production costs. However, the integration of advanced components like waveguides into photonic crystal slabs is crucial for achieving all-Si THz integrated circuits and systems. A schematic of the photonic crystal in 1D, 2D and 3 D are shown in Figure I.10.

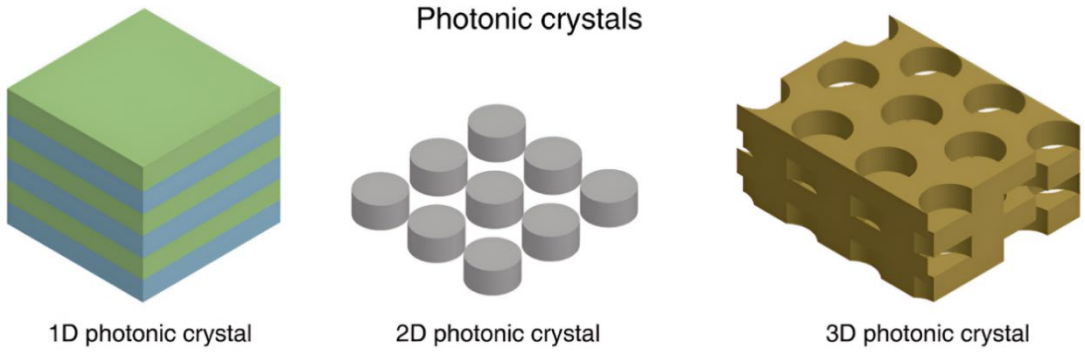

Figure I.10: 1D,2D, and 3D photonic crystal structures [90]

I.3.1.5 Silicon-based Photonic Crystal Waveguides in THz

Photonic crystal waveguides are a type of waveguide that is created by introducing a line defect into photonic crystal slabs. They work by filling an entire row of through-holes with semiconductor material to create a path for the waves to propagate. The waveguide's field confinement depends on photonic bandgap (PBG), which inhibits the propagation of THz waves with in-plane polarization in the TE bandgap region. Early reports on photonic crystal waveguides date back to 1999 when light transmission in photonic crystal waveguides at the light-wave region was first observed [19]. Since then, linear waveguides and waveguide bends were introduced in 2000 [91-94]. Until 2006, the pioneering work on 2D photonic crystal waveguides for fluid sensing by Hasek et al. demonstrated their potential for practical applications such as sensing [95, 96]. Photonic bandgap (PBG) has been extensively explored for manipulating THz waves, but there is not as much literature on their proof of concept for real-life applications. However, Hasek et al. provided experimental proof of concept to theories on measurement methods for fluids and DNA for sensing applications in the healthcare industry using a 2D photonic crystal waveguide implemented in a high-density polyethylene [97]. Parallel plates photonic crystal waveguides are another type of structure that is widely used. These structures are metallic and are bounded by parallel plates in the vertical direction and by a square lattice of holes in the horizontal axis. They have been used to demonstrate efficient guiding of THz waves with little distortion; however, they are less efficient at a higher level of integration, and their losses are quite significant due to being made of metal. The issue of loss in photonic crystal waveguides was

addressed in 2009 by Li and Zhao when they reported a Si photonic crystal waveguide with the lowest propagation loss of 9.9 dB/cm at 280 GHz in 270-330 GHz [98]. In 2013, Tsuruda et al. demonstrated a photonic crystal waveguide with reported loss as low as 0.2 dB/cm for both straight waveguides and waveguide bends for 0.315-0.329 THz [13, 56]. Such low loss was achieved by employing a 200 μm-thick high resistivity (20 kΩ.cm) Si combined with proper lattice constant and hole diameter values. Variable attenuators and resonators were introduced into the photonic crystal waveguide in 2015 by Otter et al. [99]. By illuminating the waveguide with laser light to generate free carriers in the Si waveguide, the propagation loss of a photonic crystal waveguide can be increased so that it behaves as an attenuator. Other defects, such as L3 defects, which involve removing three adjacent air holes, can create a compact cavity in photonic crystal slabs. Such cavity resonators are essential for applications such as sensing,

which has been a key target application for the THz range [100-104].

PhC Cavity Design	Q (factor)	Frequency (GHz)
Au-coated Si 2D PhC [124]	20	914
Au-coated Si 2D PhC [123]	133	1460
HR-Si 2D PhC [128]	1000	1000
HR-Si 2D PhC [125]	5800	100
HR-Si 2D PhC [127]	9000	100
HR-Si 2D PhC [126]	10800	318
HR-Si 1D wire PhC [129]	11900	100

Table I.3: A comparative table showing different quality factors obtained for some of the available THz PhCs cavities

I.3.1.6 Photonic Crystal Cavities

One of the key benefits of a photonic crystal (PhC) is its ability to act like an optical cavity, capturing photons at a specific energy for an extended period. A PhC cavity is created by introducing a point defect into the structure of a perfectly periodic PhC, which can be accomplished in various ways, such as removing a hole, changing the hole's filling material, or shifting the hole's position as shown in Fig I.11. This breaks the periodicity and produces a resonant cavity mode in the photonic bandgap.

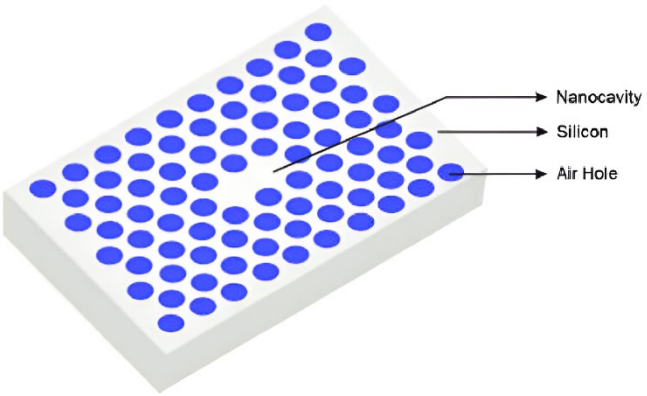

Figure I.11: Schematic of the cavity created in a photonic crystal slab. A cavity can be created in a photonic crystal by introducing the aperiodicity in the lattice [163].

2D slab (etched membrane) and 1D wire (etched waveguide) photonic crystal cavities are highly studied in the visible, near, and mid-infrared [105]– [117]. Because of the fabrication simplicity at the millimeter wavelength scale, 2D and 3D PhC cavities were reported in the 10-110 GHz frequency range [118]– [122]. At THz frequencies, high Q PhC cavities are less explored, due to the limited availability of low-loss material in this frequency range and fabrication challenges. 2D metal-coated dielectric slab photonic crystal cavities were reported in [123], [124]. These structures suffer from high metal ohmic losses and present low-quality factors of less than 140. Thanks to the low loss of high resistivity silicon several 2D slab PhC cavities with highest quality factors up to Q≈10800 were presented in [125]– [128]. Aside from [129], 1D wire photonic crystal cavities were very little investigated in the THz region. In [129] a Q of 11900 was measured for a resonant defect mode at a frequency of 100 GHz. A review of some available THz photonic crystal cavities and their performances is presented in Table I.3.

I.3.2 The first attempts of THz integrated circuits coupled to all-Si platform

High-resistivity all-Si photonic crystal slabs have been successfully used for the integration of THz range components such as straight waveguides, waveguide bends, grating couplers, attenuators, and resonators [130]. The combination of these components can lead to more advanced devices for novel applications. For instance, a multichannel transceiver that implements photonic crystal waveguides and waveguide bends has been realized, which enables multiple input-output transceivers with each waveguide corresponding to a distinct carrier channel. The carrier frequency of each channel can be adjusted using a resonant cavity tailored to operate at the desired carrier [103, 131]. All channels can be connected using waveguide bends, making it possible to create multi-component integrated systems for simultaneous sensing/probing for industry-level testing and targeted broadcasting. Further integration with oscillators and detectors can enable even more novel applications. One of the most promising devices for this purpose is the resonant tunneling diode (RTD). RTDs are very compact and can operate as oscillators and detectors at THz bands [132]. The current-voltage graph of RTD exhibits a negative differential conductance (NDC) region.

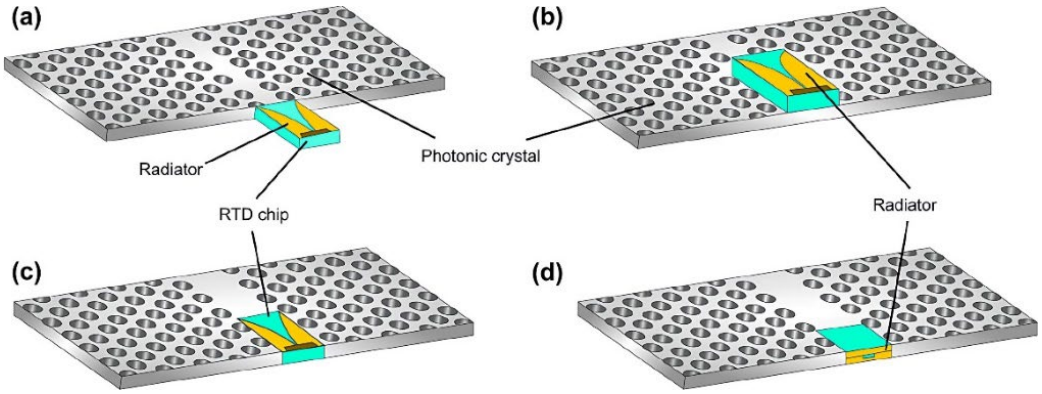

Figure I.12: Coupling schemes for hybrid integration with RTD, (a) end-fire coupling, (b) parallel coupling, (c) embed coupling, and (d) backside coupling.THz integrated systems.

Biasing the RTD with a voltage at the beginning of the NDC makes the RTD device operate as a detector. In contrast, choosing a bias voltage inside the NDC makes the RTD device operate as a fundamental THz oscillator. Suminokura et al. reported the integration of RTD with THz photonic crystal waveguides, including a tapered slot antenna integrated RTD chip [89]. Different schemes for integrating RTD chips into the photonic crystal waveguide include end-fire and parallel coupling (Figure I.12) [133]. End-fire coupling and parallel coupling have reported coupling efficiencies lower than 10%, which means that there is a lot of power loss and there is a need for better coupling schemes. At this stage, there have been reports of THz integrated systems with passive devices (waveguides, grating couplers) but also active devices (RTDs) built in an all-Si platform.

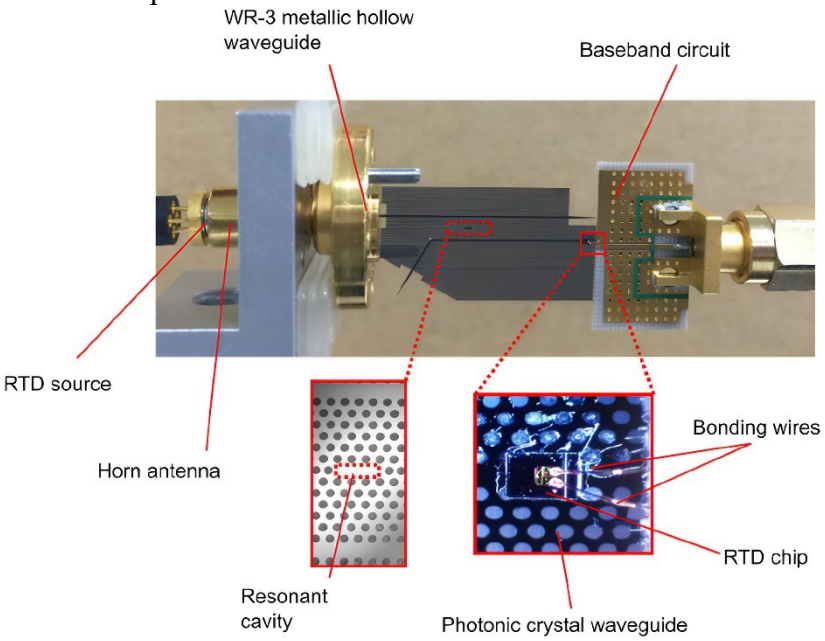

Figure I.13: Terahertz sensor realized in all-Si platform. Photonic crystal cavity acts as sensor. This device is representative of the 1G THz integrated systems.

In 2017, Okamoto et al. reported a THz sensor based on a photonic crystal platform integrated with waveguides, a high Q (~10,000) cavity, an RTD source, and a detector [134]. This sensor is representative of 1G THz systems and is illustrated in Figure I.13. Key issues to address for 2G THz integrated circuit components include the limited bandwidth of photonic crystal platforms, the low coupling efficiency of active device integration, and practical packaging.

I.3.3 Second Generation Waveguides and Integrated systems

In the previous section, we discussed the importance of THz-integrated systems that use photonic crystal components made of all-Si material. However, these integrated systems had a limited operating bandwidth, which rise a challenge to push forward their development. Therefore, this section focuses on more advanced components that build upon the previous work on photonic crystal slabs and components. These advanced components include Effective Medium (EM) waveguides, uncladded Si wire waveguides, and packaging technologies, which have helped to establish the second generation of THz integrated systems.

I.3.3.1 EM Waveguides

Dielectric effective medium (EM) waveguides consist of a composite material with properties derived from the combination of constituents, namely the dielectric material and air. The construction of EM structures involves introducing an array of through-holes into a dielectric slab. The schematic of an effective-medium-cladded dielectric waveguide is shown in Fig. I.14. All-Si EM waveguides have become popular due to their reduced transmission loss and wideband operation, as reported by Gao et al. in [135]. In their study, a waveguide core cladded with EM was presented. In contrast to photonic crystal waveguides, the in-plane guiding mechanism in EM waveguides relies on total internal reflection (TIR) rather than photonic band gap (PBG).

The small dimensions of hole diameters and perforation periods result in a structure behaving homogeneously shown in Fig. I.14, leading to enhanced bandwidth and low dispersion [135]. The design of EM structures often employs a hexagonal lattice with a lattice constant smaller than the guided wavelength. Since the EM structure comprises intrinsic Si and air, the effective refractive index falls between Si's refractive index and that of air [136, 137]. Larger holes yield an EM structure with an effective index closer to air, while smaller holes result in an effective index closer to Si. This creates a 2D index contrast that confines waves within the waveguide core through TIR. The guiding mechanism of EM waveguides relies solely on TIR, facilitated by the high index contrast in both transverse dimensions. However, due to the low cladding index in both planes (EM cladding and air cladding), EM waveguides typically support two fundamental modes: one parallel to the slab (TE mode) and another perpendicular to the slab (transverse magnetic or TM mode). These modes are associated with electric fields having distinct relative permittivities, which can be approximated using the Maxwell–Garnett approximations. The corresponding equations for these approximations are given by, [138]

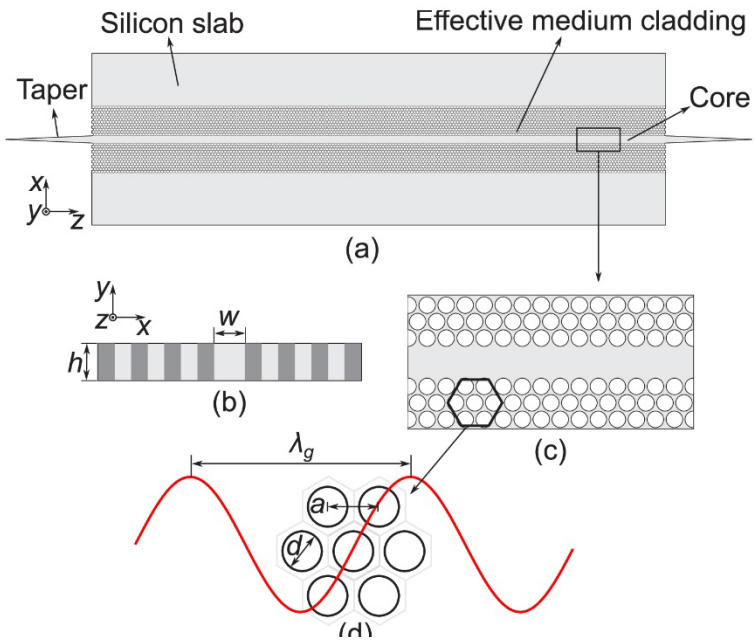

Fig. I.14. Schematic representation of an effective-medium-cladded dielectric waveguide. (a) Depicts the top view, (b) provides a magnified cross-sectional view, (c) offers an enlarged view of the waveguide core and claddings, and (d) illustrates the hexagonal lattice of the effective medium cladding with perforation period a and hole diameter d. The period a corresponds to a quarter of the shortest guided wavelength λg, distinguishing it from photonic crystal cladding that necessitates a periodicity close to half a guided wavelength. This characteristic classifies the waveguide as a dielectric waveguide rather than a photonic crystal waveguide. Tapers serve as coupling structures for insertion into hollow metallic waveguides during simulations and measurements. It's important to note that the lateral unperforated silicon regions are designed for handling purposes and do not interfere with the guided modes.[135]

$$\varepsilon_x = \varepsilon_{\mathrm{Si}} \left(\frac{(\varepsilon_0 + \varepsilon_{\mathrm{Si}}) + (\varepsilon_0 - \varepsilon_{\mathrm{Si}})\zeta}{(\varepsilon_0 + \varepsilon_{\mathrm{Si}}) - (\varepsilon_0 - \varepsilon_{\mathrm{Si}})\zeta} \right)$$

$$\varepsilon_y = \varepsilon_{\mathrm{Si}} + (\varepsilon_0 - \varepsilon_{\mathrm{Si}})$$

The permittivity values, ε_0 for air and ε_{Si} for silicon, are crucial parameters, and ζ represents the filling factor denoting the proportion of air in silicon. The specific value of ζ is influenced by the arrangement of the holes in the lattice. For instance, in a square lattice with holes arranged in square patterns, the lattice constant is approximated as $\pi d^2/(4a^2)$, where d is the hole diameter, and a is the lattice constant, representing the distance between the centers of adjacent holes.

In contrast, for a hexagonal lattice, the filling factor values can be estimated as $(\pi d^2)/(2\sqrt{3}a^2)$. These filling factor values are deducible through algebraic considerations of the lattice patterns. The choice of lattice design is motivated by considerations of robustness, with the isosceles lattice being preferred over other options [68].

In the context of electromagnetic (EM) cladded dielectric waveguides, additional considerations arise. Careful attention is required for selecting the lattice pattern, considering the desired propagation mode and the degree of confinement, which directly influences waveguide transmission. The isosceles lattice, in particular, has been favored over other lattice types for its robustness [68]. For EM waveguides, particularly those cladded with EM, it is essential to carefully consider the propagation mode to achieve the desired waveguide transmission. The choice of relative permittivity plays a critical role in enabling single-mode propagation. Lower relative permittivity results in a lower propagation constant, shifting the cutoff frequencies of higher modes to higher frequencies within the operational band. Therefore, selecting the appropriate relative permittivity is crucial for achieving the desired performance. The realization of broadband terahertz (THz) integrated systems, utilizing EM structures, relies on the effective integration of functional components. Following the development of highly broadband EM waveguides, subsequent research has explored the implementation of Bragg filters [139], planar lenses [140–143], and beam splitters [144, 145].

I.3.3.2 Uncladded Waveguides

Despite the promising performance of electromagnetic (EM) waveguides and their potential application in Terahertz (THz) integrated circuits, their practical use is impeded by the challenging fabrication process associated with the small size of the holes constituting the EM structure. The fabrication of subwavelength hole diameters demands high-precision machining, posing a significant hurdle. To address this challenge, Headland et al. introduced unclad waveguides in 2020, where "unclad" signifies the absence of cladding, making these waveguides substrateless and entirely air-cladded [146].

Before the advent of unclad structures, Si on insulator technology was employed for THz range waveguides, wherein the waveguide core was situated on an insulator substrate, commonly Si dioxide (SiO_2) [147, 148]. However, SiO_2 tends to be more absorbent than high-resistivity Si, resulting in increased absorption loss of the substrate material and making such waveguides more lossy. The concept of suspended waveguides arose to reduce losses by removing a portion or the entire substrate [149, 150]. While suspended waveguides are entirely substrates at a micro-scale, they lack self-support, making physical handling impractical. To address this, photonic crystal structures are often utilized to provide support for suspended waveguides. Despite this, photonic crystal structures typically exhibit limited bandwidth and increased dispersion in the Photonic Band Gap (PBG) region, making suspended waveguides narrowband and dispersive.

Efforts were then directed towards Si on glass waveguides [73, 149], but for THz integrated systems, a preference for all-Si components emerged. This preference led to the development of recent uncladded waveguides, an extension of EM waveguides, involving the removal of an in-plane EM cladding structure and the introduction of a protective Si frame [146]. Unclad waveguides offer simplicity and greater freedom in choosing design parameters like waveguide thickness, leading to faster analysis, simulations, design, and fabrication. Similar to EM waveguides, uncladded waveguides can be fabricated in all intrinsic Si, enabling monolithic integration with various functional devices and supporting elements entirely made of Si. The appearance of the supporting element can be tailored to fit physical packaging requirements and facilitate handling and testing [146].

All-Si uncladded waveguides provide a versatile platform for integrating Y-branches, couplers, and multiplexers. The absence of EM cladding eases hybrid integration, with a reported transmission loss of less than 0.1 dB/cm, enabling the realization of more complex designs with higher and more intricate bending. Specific structures such as 90-degree-bends Y-branches and evanescent couplers have been successfully implemented based on unclad structures [146]. Resonators were also reported in suspended waveguides using a single period of photonic crystal structure [151].

I.3.3.3 Advancements in Second Generation THz Integrated Systems

Integrated Terahertz (THz) systems have undergone significant evolution, with the first generation (1G) demonstrating the potential of compact configurations relying on photonic crystal components. However, 1G faced challenges such as limited bandwidth and low coupling efficiency for active devices like Resonant Tunneling Diodes (RTD). The emergence of novel devices has driven the transition to the second generation (2G), characterized by improved bandwidth performance.Efforts in the development of Electromagnetic (EM) waveguides and unclad waveguides have run parallel to initiatives aimed at enhancing RTD integration with all-silicon (Si) platforms to boost coupling efficiency. Hybrid integration with active components has become crucial due to the challenge of insufficient available power in THz systems.

In 2018, Yu et al. introduced compact Yagi–Uda and tapered-slot coupling structures on InP substrate, significantly enhancing coupling efficiency and achieving a 5 GHz bandwidth improvement [134, 152, 103].

The improved coupling efficiency, reaching ~56% and 50% for Yagi–Uda and tapered slot antenna, respectively, was attributed to advancements in the exponential profile of the taper. A mode converter, reported in [153], further increased the coupling efficiency to 90%, with a 3-dB bandwidth improvement to 50 GHz. Enhanced coupling schemes, notably embed coupling, played a role in these improvements.

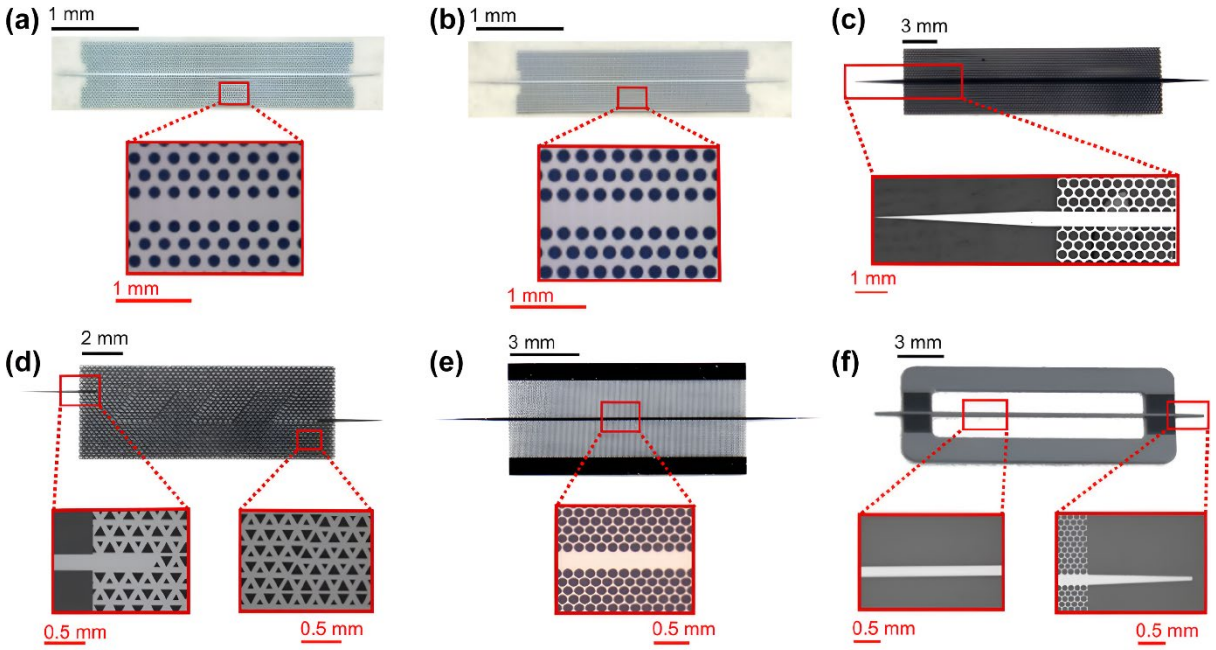

Figure I.15 : Planar all-Si waveguide platforms and respective simulated field distribution, (a) photonic crystal waveguide with equilateral lattice [68], (b) photonic crystal waveguide with isosceles lattice [68], (c) Bragg-mirror suppressed waveguide [159], (d) topological waveguide [160], (e) EM waveguide [135], (f) unclad waveguide [146].

The application of these advancements led to the realization of THz range integrated communication modules, incorporating dielectric tapers for versatile coupling options with hollow metallic waveguides, facilitating testing, and wired/wireless THz fiber communications. Additional THz communication applications showcased straight photonic crystal waveguides, a horn antenna and RTD module, and a dielectric rod array antenna. Silicon-integrated mixers on a Si photonic-crystal platform for the 0.3-THz and 0.2-THz bands using RTD and Schottky diode, respectively, were reported as well [154, 155]. Compact packaging structures are essential for THz integrated systems, even with improved passive components and highly efficient THz sources. Sturdy metal-based packaging structures have been reported for THz range waveguide platforms, offering ease of manufacturing with high-precision machining [156, 157]. Although alternative materials like Polyether Ether Ketone (PEEK) are gaining attention for environmental considerations, their development is in the early stages and presents challenges in achieving accurate machining. This marks the advent of the second generation of THz range integrated systems, offering possibilities that could revolutionize various fields such as healthcare, transportation, and security. The exploration of these applications represents the next frontier for THz integrated systems.

A comprehensive comparison of all Si waveguides and their performances is detailed in Table I.4, and Figure I.15 provides visual representations of reported all-Si planar waveguides [67, 140, 153, 154, 155].

Reference	Waveguide type	Frequency range (GHz)	Relative Bandwidth	Propagation Loss	Applications Demonstrated
[97],[103]	Photonic Crystal	97-109	~11.6	_	Communications (1.5 Gbit/s), HD video transmission, sensing
[101]	Photonic Crystal	100	_	_	Liquid sensing
[68]	Photonic Crystal	324-361	~10	<0.1	Communications (36 Gbit/s)
[135]	EM	260-400	>40	0.05	Communications (30 Gbit/s), 4K video transmission
[158]	EM	500–750	~40%	–	Communications (10 Gbit/s)
[146]	Uncladded	260–390	~40	0.059	Communications (30 Gbit/s), sensing
[151]	Suspended	500–750	~40%	0.065	–

Table I.4: Comparison of planar all-Si dielectric waveguides [69].

I.4 Towards THz Topological Photonics

The most recent advancement comes in the form of uncladded waveguides, showcasing improved bandwidth, low loss, and enhanced versatility. With their enhanced performance attributes, these structures have been instrumental in the realization of second-generation (2G) THz integrated circuits. Looking forward, the third generation (3G) of THz integrated components is envisioned to center around large-scale integration. Upcoming technologies driving this evolution are robust topological waveguides [160] and backside coupling for active devices [162], as depicted in Figures Figure I.15 (d).

THz topological photonics originates from the topological phase of light. Initial reports on topological photonics showcased photonic topological insulators (PTIs), benefiting from the absence of backscattering.

Building upon PTIs, subsequent endeavors introduced valley Hall photonic crystals (VPCs) and explored their practical applications. VPCs represent ideal structures for reflection-less waveguides, particularly well-suited for THz integrated systems due to their potential for

reduced losses without backscattering and low dispersion. In 2020, Yang et al. conducted the first experimental demonstration of the topological phase of THz waves for on-chip communication using VPCs, achieving near-unity transmission over the operational band, even with the structure incorporating sharp bends. The exceptional performance of VPCs is attributed to topological valley kink states, enabling robust topological transport of THz waves, even around sharp bends. Additionally, these valley kink states exhibit linearity in the bandgap, translating into linear dispersion in VPCs, indicative of constant group delay at different frequencies and facilitating broadband operation. VPCs also support single-mode operation, with observations revealing a singular kink state in the bandgap.

It is noteworthy that the topological bandgap and photonic crystal bandgap are distinct, with the former originating from Bragg reflections, and the latter originating from the breakage of inversion symmetry. The difference between photonic crystals and topological photonics like VPC extends beyond the origin of their respective bandgaps. The structure of the photonic crystal involves introducing an array of through-holes arranged mostly in a triangular pattern into a Silicon (Si) slab. In contrast, VPC is created using holes of different sizes arranged in a hexagonal pattern.

Valley kink states in topological waveguides, characterized by linear dispersion and single-mode operation, have surpassed the performance of typical photonic crystal waveguides in terms of operational bandwidth and overall loss. Notably, record data rates of 108 Gbit/s were reported in 2021 by Webber et al. for 10-mm topological waveguides, underscoring the potential of topological structures for high-data-rate communication applications. To achieve even higher data rates, a crucial future focus will be on increasing the bandwidth of the PBG of VPC. A recent study on interfacial topological photonics in the context of Si-VPC waveguides, has demonstrated lossless THz wave propagation through sharp bends, typically designed with standard zigzag interfaces.

The study introduces a novel approach by designing a composite interface junction for an air-slot-like VPC waveguide with a 60° bend and an unchanging bearded interface, enabling topologically protected THz wave propagation over a 20% relative bandwidth. Through particle swarm optimization, the geometry of the bearded-interface silicon VPC waveguide is optimized, achieving a significant 42% relative bandgap and supporting a broadband topological edge state spanning a usable 25% relative bandwidth. The scalability of this design

method across the electromagnetic spectrum, from microwave to optical regimes, emphasizes its potential applications in broadband silicon topological waveguides. The study underscores the prospects and challenges of interfacial topological photonics, showcasing its relevance in developing silicon waveguide technologies for various applications, including on-chip THz sixth-generation (6G) communication. Additionally, the comprehensive analysis explores the impact of air hole geometry on the relative bandgap and relative bandwidth of topological edge states in silicon VPC waveguides with a bearded interface. The findings highlight the emergence of interfacial topological photonics as a promising avenue for designing broadband silicon waveguides, offering insights for potential integration into THz topological integrated devices for 6G communications and topological waveguide cavities for THz sensing applications.

Conclusion of this chapter

This chapter provides an overview of the evolution of THz range techniques, waveguides and their recent evolution towards future potential road for THz integration. Traditional metal-based waveguides have resulted in bulky THz systems with relatively high insertion and ohmic losses while being quite easy to use. Hence, research has focused on all-dielectric waveguide platforms as a replacement for metal-based waveguides to reduce losses. All-silicon (Si) waveguides have gained significant attention in recent years, influenced by the progress of THz-photonics using silicon. Specifically, recent advances in planar all-Si platforms, known as "THz silicon photonics", have focused on waveguides platforms. The starting point was a photonic crystal slab, which allowed for the trapping and control of THz waves, leading to photonic crystal waveguides. Photonic crystal waveguides with low propagation loss and low dispersion but limited bandwidth have been reported. Subsequently, EM waveguides have been developed to increase the limited bandwidth of photonic crystal waveguides, leading to waveguides with over 40% relative bandwidth. Recently, uncladded waveguides have demonstrated enhanced bandwidth, low loss, and versatility, and have been utilized for THz integrated components, establishing 2G THz integrated circuits. The third generation (3G) of THz integrated components will focus on large-scale integration, driven by robust topological waveguides and backside coupling for active devices.

Looking on the state-of-the-art and trends on waveguiding approaches, we can highlight that the next-generation waveguides and integrated platforms can make use of valley photonic

crystals, a platform that utilizes the topological phases of light. Topological photonics is an emerging field that has garnered significant interest for its innovative ways of engineering the flow of light. With the aid of topological protection, the surface modes of topological photonic systems possess intriguing properties, such as unidirectional propagation and robust transmission against defects and disorders, which meet the rapidly growing demands for information processing. Therefore, this thesis work primarily focuses on designing, fabricating, and experimentally demonstrating several passive functions on the 600 GHz central frequency region. Initially, we demonstrate robust valley edge modes using straight waveguides at the 600 GHz frequency region. We then exploit several parameters in the VPC unit cell, such as air hole geometry and interfacial terminations between two VPC types, to manipulate or modify topological protection. We introduce variations in topological protection by considering different interfacial designs and suitable air-hole geometries for passive functional devices. We show that the partial breakup of topological protection could be an asset for designing on-chip passive functionalities. To this end, we focused on bearded and zigzag junctions and appropriate air-hole geometries for VPC unit cells. To experimentally verify the scalability of topological protection, we demonstrate the performance of THz topological ring resonators and THz double-cavity resonators designed for operation in the 600 GHz frequency region. This work showcases how the scaling of topological protection can be achieved by utilizing a combination of air hole geometry and interfacial degrees of freedom, providing functional tuning of devices at the chip level. In addition, we demonstrate for the first time datacom measurement in the 600 GHz frequency range using the developed topological devices.

Thus, this thesis is focused on the THz fields and applications as well as the topological photonics community, providing contributions to next-generation high-speed 6G communications and beyond.

Chapter 2 is dedicated to the theoretical and numerical studies of topological photonics. We will elaborate on the concepts behind the emergence of valley edge modes and introduce our designs, such as waveguides, resonators, filters, and double-cavity resonators using various designs.

Chapter 3 is dedicated to fabrication techniques. We make use of a high-resistivity SOI wafer to fabricate our devices, primarily employing photolithography and DRIE as the key processes.

The last one, Chapter 4 is entirely dedicated to experimental methods and experimental results. We performed VNA-based measurements, mainly measuring transmission and group delay for our devices, and a datacom experiment, which is a first-time demonstration at 600 GHz, to the best of our knowledge.

References

[1] NICT, "About Terahertz," [Online]. Available: https://www2.nict.go.jp/ttrc/thz-sensing/about_Thz
[2] X. C. Zhang and J. Xu, "THz Wave Near-Field Imaging" in Introduction to THz Wave Photonics, Boston, MA: Springer US, pp. 149-174, 2010.
[3] E. F. Nichols, "A Study of the Transmission Spectra of Certain Substances in the Infra-Red," Phys. Rev. Ser. I, vol. 1, no. 1, pp. 1–18, Jul. 1893, doi: 10.1103/PhysRevSeriesI.1.1.
[4] J. R. Ashley and F. M. Palka, "Transmission Cavity and Injection Stabilization of an X-Band Transferred Electron Oscillator," in 1973 IEEE G-MTT International Microwave Symposium, Jun. 1973, pp. 181–182, doi: 10.1109/GMTT.1973.1123140.
[5] J. W. Fleming, "High-Resolution Submillimeter-Wave Fourier-Transform Spectrometry of Gases," IEEE Trans. Microw. Theory Tech., vol. 22, no. 12, pp. 1023–1025, Dec. 1974, doi: 10.1109/TMTT.1974.1128419.
[6] A. J. Kerecman, "The Tungsten - P Type Silicon Point Contact Diode," in 1973 IEEE G-MTT International Microwave Symposium, Boulder, CO, USA, 1973, pp. 30–34, doi: 10.1109/GMTT.1973.1123080.
[7] D. H. Auston and M. C. Nuss, "Electrooptical generation and detection of femtosecond electrical transients," IEEE J. Quantum Electron., vol. 24, no. 2, pp. 184–197, Feb. 1988, doi: 10.1109/3.114.
[8] E. Pickwell-MacPherson and V. P. Wallace, "Terahertz pulsed imaging—A potential medical imaging modality?," Photodiagnosis Photodyn. Ther., vol. 6, no. 2, pp. 128–134, Jun. 2009, doi: 10.1016/j.pdpdt.2009.07.002.
[9] S. J. Oh, Y.-M. Huh, J.-S. Suh, J. Choi, S. Haam, and J.-H. Son, "Cancer Diagnosis by Terahertz Molecular Imaging Technique," J. Infrared Millim. Terahertz Waves, vol. 33, no. 1, pp. 74–81, Jan. 2012, doi: 10.1007/s10762-011-9847-9.
[10] T. Hasebe, S. Kawabe, H. Matsui, and H. Tabata, "Metallic mesh-based terahertz biosensing of single- and double-stranded DNA," J. Appl. Phys., vol. 112, no. 9, p. 094702, Nov. 2012, doi: 10.1063/1.4761966.
[11] X. Yang et al., "Biomedical Applications of Terahertz Spectroscopy and Imaging," Trends Biotechnol., vol. 34, no. 10, pp. 810–824, Oct. 2016, doi: 10.1016/j.tibtech.2016.04.008.
[12] L. Ho, M. Pepper, and P. Taday, "Signatures and fingerprints," Nat. Photonics, vol. 2, no. 9, Art. no. 9, Sep. 2008, doi: 10.1038/nphoton.2008.174.
[13] S. L. Dexheimer, Terahertz Spectroscopy: Principles and Applications. CRC Press, 2017.
[14] M. C. Kemp, "Explosives Detection by Terahertz Spectroscopy—A Bridge Too Far?," IEEE Trans. Terahertz Sci. Technol., vol. 1, no. 1, pp. 282–292, Sep. 2011, doi: 10.1109/TTHZ.2011.2159647.
[15] J. B. Baxter and G. W. Guglietta, "Terahertz Spectroscopy," Anal. Chem., vol. 83, no. 12, pp. 4342–4368, Jun. 2011, doi: 10.1021/ac200907z.
[16] M. Theuer, S. S. Harsha, D. Molter, G. Torosyan, and R. Beigang, "Terahertz Time-Domain Spectroscopy of Gases, Liquids, and Solids," ChemPhysChem, vol. 12, no. 15, pp. 2695–2705, Oct. 2011, doi: 10.1002/cphc.201100158.
[17] F. Hindle et al., "Monitoring of food spoilage by high resolution THz analysis," Analyst, vol. 143, no. 22, pp. 5536–5544, Nov. 2018, doi: 10.1039/C8AN01180J.
[18] A. Redo-Sanchez et al., "Assessment of terahertz spectroscopy to detect antibiotic residues in food and feed matrices," Analyst, vol. 136, no. 8, pp. 1733–1738, Mar. 2011, doi: 10.1039/C0AN01016B.

[19] G. Ok, H. J. Kim, H. S. Chun, and S.-W. Choi, "Foreign-body detection in dry food using continuous sub-terahertz wave imaging," Food Control, vol. 42, pp. 284–289, Aug. 2014, doi: 10.1016/j.foodcont.2014.02.021.
[20] G. Ok, K. Park, H. J. Kim, H. S. Chun, and S.-W. Choi, "High-speed terahertz imaging toward food quality inspection," Appl. Opt., vol. 53, no. 7, pp. 1406–1412, Mar. 2014, doi: 10.1364/AO.53.001406.
[21] T. Nagatsuma, G. Ducournau, and C. C. Renaud, "Advances in terahertz communications accelerated by photonics," Nat. Photonics, vol. 10, no. 6, Art. no. 6, Jun. 2016, doi: 10.1038/nphoton.2016.65.
[22] G. Ducournau et al., "THz Communications using Photonics and Electronic Devices: the Race to Data-Rate," J. Infrared Millim. Terahertz Waves, vol. 36, no. 2, pp. 198–220, Feb. 2015, doi: 10.1007/s10762-014-0112-x.
[23] C. K. Walker, Terahertz Astronomy. CRC Press, 2015.
[24] A. V. Smirnov et al., "Space mission Millimetron for terahertz astronomy," in Space Telescopes and Instrumentation 2012: Optical, Infrared, and Millimeter Wave, Sep. 2012, vol. 8442, p. 84424C, doi: 10.1117/12.927184.
[25] C. Kulesa, "Terahertz Spectroscopy for Astronomy: From Comets to Cosmology," IEEE Trans. Terahertz Sci. Technol., vol. 1, no. 1, pp. 232–240, Sep. 2011, doi: 10.1109/TTHZ.2011.2159648.
[26] T. S. Rappaport et al., "Wireless communications and applications above 100 GHz: Opportunities and challenges for 6G and beyond," IEEE Access, vol. 7, pp. 78729-78757, 2019.
[27] P. Yang, Y. Xiao, M. Xiao and S. Li, "6G Wireless communications: Vision and potential techniques," IEEE Netw., vol. 33, no. 4, pp. 70-75, Jul./Aug. 2019.
[28] P. Heydari, H. Wang, H. Mohammadnezhad and P. Nazari, "Energy efficient 100+ GHz transceivers enabling beyond-5G wireless communications," IEEE Wireless Commun., vol. 28, no. 1, pp. 144-151, Feb. 2021.
[29] I. F. Akyildiz, A. Kak and S. Nie, "6G and beyond: The future of wireless communications systems," IEEE Access, vol. 8, pp. 133995-134030, 2020.
[30] S. Dang, O. Amin, B. Shihada and M.-S. Alouini, "What should 6G be?," Nature Electron., vol. 3, no. 1, pp. 20-29, Jan. 2020.
[31] R.A. Lewis, "A review of terahertz sources," J. Phys. D Appl. Phys., vol. 47, 374001, 2014. [CrossRef]
[32] R. Safian, G. Ghazi, N. Mohammadian, "Review of photomixing continuous-wave terahertz systems and current application trends in terahertz domain," Opt. Eng., vol. 58, pp. 1–28, 2019. [CrossRef]
[33] P. Uhd, R.H. Jepsen, S. Jacobsen, R. Keiding, "Generation and detection of terahertz pulses from biased semiconductor antennas," Opt. Soc. Am. B, vol. 13, pp. 2424–2436, 1996.
[34] N.M. Burford, M.O. El-Shenawee, "Review of terahertz photoconductive antenna technology," Opt. Eng., vol. 56, 010901, 2017. [CrossRef]
[35] A. Rice, Y. Jin, X.F. Ma, X.-C. Zhang, "Terahertz optical rectification from zinc-blende crystals," Appl. Phys. Lett., vol. 64, 1324, 1994. [CrossRef]
[36] X.C. Zhang, X.F. Ma, Y. Jin, T.M. Lu, E.P. Boden, P.D. Phelps, K.R. Stewart, C.P. Yakymyshyn, "Terahertz optical rectification from a nonlinear organic crystal," Appl. Phys. Lett., vol. 61, pp. 3080–3082, 1992. [CrossRef]
[37] Y.J. Ding, "Progress in terahertz sources based on difference-frequency generation [Invited]," J. Opt. Soc. Am. B, vol. 31, pp. 2696–2711, 2014. [CrossRef]
[38] R. Sowade, I. Breunig, I.C. Mayorga, J. Kiessling, C. Tulea, V. Dierolf, K. Buse, "Continuous-wave optical parametric terahertz source," Opt. Express, vol. 17, pp. 22303–22310, 2009. [CrossRef]
[39] BURFORD, Nathan M. et EL-SHENAWEE, Magda O. Review of terahertz photoconductive antenna technology. *Optical Engineering*, 2017, vol. 56, no 1, p. 010901-010901.
[40] R. Safian, G. Ghazi, N. Mohammadian, "Review of photomixing continuous-wave terahertz systems and current application trends in terahertz domain," Opt. Eng., vol. 58, pp. 1–28, 2019. [CrossRef]
[41] E.R. Brown, K.A. Mcintosh, K.B. Nichols, C.L. Dennis, "Photomixing up to 3.8 THz in low-temperature-grown GaAs," Appl. Phys. Lett., vol. 66, pp. 285, 1995. [CrossRef]

[42] H.-J. Song, N. Shimizu, T. Furuta, K. Suizu, H. Ito, "Broadband-frequency-tunable sub-terahertz wave generation using an optical comb, AWGs, optical switches, and a uni-traveling carrier photodiode for spectroscopic applications," J. Lightw. Technol., vol. 26, pp. 2521–2530, 2008. [CrossRef]
[43] R. Efthymios, C.C. Renaud, D.G. Moodie, M.J. Robertson, A.J. Seeds, "Traveling-wave uni-traveling carrier photodiodes for continuous wave THz generation," Opt. Express, vol. 18, pp. 11105–11110, 2010. [CrossRef]
[44] S. Preu, F.H. Renner, S. Malzer, G.H. Doehler, L.J. Wang, M. Hanson, A.C. Gossard, T.U. Wilkinson, E.R. Brown, "Efficient terahertz emission from ballistic transport enhanced n-i-p-n-i-p superlattice photomixers," Appl. Phys. Lett., vol. 90, 2128, 2007. [CrossRef]
[45.]BECK, Alexandre, DUCOURNAU, Guillaume, ZAKNOUNE, Mohammed, *et al.* High-efficiency uni-travelling-carrier photomixer at 1.55 µm and spectroscopy application up to 1.4 THz. *Electronics Letters*, 2008, vol. 44, no 22, p. 1320-1322.
[46] H. Ito, F. Nakajima, T. Furuta, T. Ishibashi, "Continuous THz-wave generation using antenna-integrated uni-travelling-carrier photodiodes," Semicond. Sci. Technol., vol. 20, pp. S191–S198, 2005. [CrossRef]
[47] S. Nellen, T. Ishibashi, A. Deninger, R.B. Kohlhaas, L. Liebermeister, M. Schell, B. Globish, "Experimental comparison of utcand pin-photodiodes for continuous-wave terahertz generation," J. Infrared Millim. Terahertz Waves, vol. 41, pp. 343–354, 2020. [CrossRef]
[48] M. Tonouchi, "Cutting-edge terahertz technology," Nat. Photonics, vol. 1, pp. 97–105, 2007. [CrossRef]
[49] C. Kübler, R. Huber, A. Leitenstorfer, "Ultrabroadband terahertz pulses: Generation and field-resolved detection," Semicond. Sci. Technol., vol. 20, pp. S128–S133, 2005. [CrossRef]
[50] C. Fattinger, D. Grischkowsky, "Point source terahertz optics," Appl. Phys. Lett., vol. 53, pp. 1480–1482, 1988. [CrossRef]
[51] T. Nagatsuma, G. Ducournau, C.C. Renaud, "Advances in terahertz communications accelerated by photonics," Nat. Photonics, vol. 10, pp. 371–379, 2016. [CrossRef]
[52] A.J. Seeds, H. Shams, M.J. Fice, C.C. Renaud, "TeraHertz Photonics forWireless Communications," J. Lightw. Technol., vol. 33, pp. 579–587, 2015. [CrossRef]
[53] Xie, Jingya, Wangcheng Ye, Linjie Zhou, Xuguang Guo, Xiaofei Zang, Lin Chen, and Yiming Zhu. 2021. "A Review on Terahertz Technologies Accelerated by Silicon Photonics" *Nanomaterials* 11, no. 7: 1646. https://doi.org/10.3390/nano11071646
[54] D.J. Harris, "Waveguides for the 100–1000 GHz frequency range," Radio Electron. Eng., vol. 49, pp. 389–394, 1979.
[55] G. Gallot, S.P. Jamison, R.W. McGowan, D. Grischkowsky, "Terahertz waveguides," J. Opt. Soc. Am. B, vol. 17, pp. 851–863, 2000.
[56] O. Mitrofanov, R. James, F. A. Fernández, T. K. Mavrogordatos, and J. A. Harrington, "Reducing transmission losses in hollow THz waveguides," IEEE Trans. Terahertz Sci. Technol., vol. 1, no. 1, pp. 124–132, 2011.
[57] T. Kurokawa et al., "Over 300 GHz bandwidth UTC-PD module with 600 GHz band rectangular-waveguide output". Electron. Lett., vol. 54: pp. 705-706, 2018. https://doi.org/10.1049/el.2018.0932.
[58] "Virginia Diodes, Inc - Your Source for Terahertz and mm-Wave Products." https://www.vadiodes.com/en/.
[59] K. M. K. H. Leong et al., "WR1.5 Silicon Micromachined Waveguide Components and Active Circuit Integration Methodology," IEEE Trans. Microw. Theory Tech., vol. 60, no. 4, pp. 998–1005, Apr. 2012, doi: 10.1109/TMTT.2012.2184296.
[60] J. Hu, S. Xie, and Y. Zhang, "Micromachined Terahertz Rectangular Waveguide Bandpass Filter on Silicon-Substrate," IEEE Microw. Wirel. Compon. Lett., vol. 22, no. 12, pp. 636–638, Dec. 2012, doi: 10.1109/LMWC.2012.2228179.
[61]. Title: IEEE Standard for Rectangular Metallic Waveguides and Their Interfaces for Frequencies of 110 GHz and Above—Part 1: Frequency Bands and Waveguide Dimensions URL: https://ieeexplore.ieee.org/stamp/stamp.jsp?arnumber=6471987
[62]Y. Matsuura and E. Takeda, "Hollow optical fibers loaded with an inner dielectric film for terahertz broadband spectroscopy," J. Opt. Soc. Am. B, vol. 25, no. 12, pp. 1949–1954, 2008.

[63]H. Zhan, R. Mendis, and D. M. Mittleman, “Terahertz energy confinement in finite-width parallel-plate waveguides,” in Joint Int. Symp. Photoelectron. Detect. Imaging and Terahertz High Energy radiat Detect. Technol. Appl., 2009, pp. 1–2. https://doi.org/10.1117/12.836722.
[64] L.-J. Chen, H.-W. Chen, T.-F. Kao, J.-Y. Lu, and C.-K. Sun, “Lowloss subwavelength plastic fiber for terahertz waveguiding,”Opt. Lett., vol. 31, no. 3, pp. 308–310, 2006.
[65]. M. Y. Frankel, S. Gupta, J. A. Valdmanis, and G. A. Mourou, “Terahertz attenuation and dispersion characteristics of coplanar transmission lines,” IEEE Trans. Microw. Theor. Tech., vol. 39, no. 6, pp. 910–916, 1991.
[66] D. R. Grischkowsky, “Optoelectronic characterization of transmission lines and waveguides by terahertz time-domain spectroscopy,” IEEE J. Sel. Top. Quant. Electron., vol. 6, no. 6, pp. 1122–1135, 2000.
[67]. K. Tsuruda, M. Fujita, and T. Nagatsuma, “Extremely low-loss terahertz waveguide based on silicon photonic-crystal slab,”Opt. Express, vol. 23, no. 25, pp. 31977–31990, 2015.
[68]. X. Yu, M. Sugeta, Y. Yamagami, M. Fujita, and T. Nagatsuma, “Simultaneous low-loss and low-dispersion in a photoniccrystal waveguide for terahertz communications,” APEX, vol. 12, no. 1, pp. 012005–012009, 2019.
[69]. Koala, R. A., Fujita, M., & Nagatsuma, T. (2022). Nanophotonics-inspired all-silicon waveguide platforms for terahertz integrated systems. *Nanophotonics*, *11*(9), 1741-1759.
[70] J. C. Knight, T. A. Birks, P. S. J. Russell, and D. M. Atkin, “Allsilica single-mode optical fiber with photonic crystal cladding:errata,” Opt. Lett., vol. 21, no. 19, pp. 1547–1549, 1996. https://doi.org/10.1364/OL.21.001547.
[71] A. Argyros, “Microstructures in polymer fibres for optical fibres, THz waveguides, and fibre-based metamaterials,” ISRN Opt., vol. 2013, pp. 1–22, 2013.
[72] A. Patrovsky and K. Wu, “Substrate integrated image guide (SIIG) - a planar dielectric waveguide technology for millimeterwave applications,” IEEE Trans. Microw. Theor. Tech., vol. 54, no. 6, pp. 2872–2879, 2006.
[73] N. Ranjkesh, M. Basha, A. Taeb, and S. Safavi-Naeini, “Siliconon-glass dielectric waveguide-Part II: for THz applications,” IEEE Trans. Terahertz Sci. Technol., vol. 5, no. 2, pp. 280–287, 2015
[74] H.-M. Heiliger, M. Nagel, H. G. Roskos, et al., “Low-dispersion thin-film microstrip lines with cyclotene (benzocyclobutene) as dielectric medium,” Appl. Phys. Lett., vol. 70, no. 17, pp. 2233–2235, 1997.
[75] F. Meng, X. Huang, and B. Jia, “Bi-directional evolutionary optimization for photonic band gap structures,” J. Comput. Phys., vol. 302, pp. 393–404, 2015.
[76] C. Elachi and C. Yeh, “Periodic structures in integrated optics,” J. Appl. Phys., vol. 44, no. 7, pp. 3146–3152, 1973.
[77] E. Yablonovitch, “Inhibited spontaneous emission in solidstate physics and electronics,” Phys. Rev. Lett., vol. 58, no. 20,pp. 2059–2062, 1987.
[78]Y. Y. Wang, N. V. Wheeler, F. Couny, P. J. Roberts, and F. Benabid, “Low loss broadband transmission in hypocycloidcore Kagome hollow-core photonic crystal fiber,” Opt. Lett., vol. 36, no. 5, pp. 669–671, 2011.
[79] J. Dai, J. Zhang, W. Zhang, and D. Grischkowsky, “Terahertz time-domain spectroscopy characterization of the far-infrared absorption and index of refraction of high-resistivity, float-zone silicon,” *JOSA B*, vol. 21, no. 7, pp. 1379–1386, Jul. 2004, doi: 10.1364/JOSAB.21.001379.
[80] D. Grischkowsky, S. Keiding, M. van Exter, and C. Fattinger, “Far-infrared time-domain spectroscopy with terahertz beams of dielectrics and semiconductors,” *JOSA B*, vol. 7, no. 10, pp. 2006–2015, Oct. 1990, doi: 10.1364/JOSAB.7.002006.
[81] N. Ranjkesh, M. Basha, A. Taeb, A. Zandieh, S. Gigoyan, and S. Safavi-Naeini, “Silicon-on-Glass Dielectric Waveguide—Part I: For Millimeter-Wave Integrated Circuits,” *IEEE*

Trans. Terahertz Sci. Technol., vol. 5, no. 2, pp. 268–279, Mar. 2015, doi: 10.1109/TTHZ.2015.2399693.
[82] M. Naftaly and R. E. Miles, "Terahertz Beam Interactions with Amorphous Materials," in Terahertz Frequency Detection and Identification of Materials and Objects, Dordrecht, 2007, pp. 107–122.
[83] N. Ranjkesh, M. Basha, A. Taeb, and S. Safavi-Naeini, "Silicon-on-Glass Dielectric Waveguide—Part II: For THz Applications," IEEE Trans. Terahertz Sci. Technol., vol. 5, no. 2, pp. 280–287, Mar. 2015, doi: 10.1109/TTHZ.2015.2397279.
[84] E. Yablonovitch, "Inhibited Spontaneous Emission in Solid-State Physics and Electronics," Phys. Rev. Lett., vol. 58, no. 20, pp. 2059–2062, May 1987, doi: 10.1103/PhysRevLett.58.2059.
[85] Lord Rayleigh, "XVII. On the maintenance of vibrations by forces of double frequency, and on the propagation of waves through a medium endowed with a periodic structure," Lond. Edinb. Dublin Philos. Mag. J. Sci., vol. 24, no. 147, pp. 145–159, Aug. 1887, doi: 10.1080/14786448708628074.
[86] E. Yablonovitch, "Photonic band structure: the face-centered-cubiccase," p. 9.
[87] S. Noda, A. Chutinan, and M. Imada, "Trapping and emission of photons by a single defect in a photonic bandgap structure," Nature, vol. 407, no. 6804, pp. 608–610, 2000.
[88] M. Fujita, S. Takahashi, Y. Tanaka, T. Asano, and S. Noda,
"Applied physics: simultaneous inhibition and redistribution of spontaneous light emission in photonic crystals," Science, vol. 308, no. 5726, pp. 1296–1298, 2005
[89] R. Kakimi, M. Fujita, M. Nagai, M. Ashida, and T. Nagatsuma, "Capture of a terahertz wave in a photonic-crystal slab," Nat. Photonics, vol. 8, no. 8, pp. 657–663, 2012.
[90]. Deng, Ruhuan, Liu, Wenzhe and Shi, Lei. "Inverse design in photonic crystals" *Nanophotonics*, 2024. https://doi.org/10.1515/nanoph-2023-0750
[91] A. Chutinan and S. Noda, "Waveguides and waveguide bends in two-dimensional photonic crystal slabs," Phys. Rev., vol. 62, no. 7, pp. 4488–4492, 2000.
[92] S. G. Johnson, P. R. Villeneuve, S. Fan, and J. D. Joannopoulos, "Linear waveguides in photonic-crystal slabs," Phys. Rev. BCondens. Matter, vol. 62, no. 12, pp. 8212–8222, 2000.
[93] M. Lončar, J. Vučković, and A. Scherer, "Methods for controlling positions of guided modes of photonic-crystal waveguides,"J. Opt. Soc. Am. B, vol. 18, no. 9, pp. 1362–1368, 2001.
[94] W. T. Lau and S. Fan, "Creating large bandwidth line defects by embedding dielectric waveguides into photonic crystal slabs,"Appl. Phys. Lett., vol. 81, no. 21, pp. 3915–3917, 2002.
[95] H. Kurt and D. S. Citrin, "Photonic crystals for biochemical sensing in the terahertz region," Appl. Phys. Lett., vol. 87, no. 4, pp. 1–4, 2005.
[96] T. Hasek, R. Wilk, H. Kurt, D. Citrin, and M. Koch, "Sub-terahertz 2D photonic crystal waveguides for fluid sensing applications,"in Joint Int. Conf. Infrared, Millimeter, Terahertz Waves.
[97] T. Hasek, H. Kurt, D. S. Citrin, and M. Koch, "Photonic crystals for fluid sensing in the subterahertz range," Appl. Phys. Lett., vol. 89, no. 17, pp. 87–90, 2006.
[98] J. Li and X. Zhao, "Terahertz waveguides based on photonic crystal," Opt. InfoBase Conf. Pap., pp. 4–5, 2009. https://doi.org/10.1364/acp.2009.tuv4.
[99] W. J. Otter, S. M. Hanham, N. M. Rider, A. S. Holmes, N. Klein, S. Lucyszyn. "Terahertz photonic crystal technology," in Proc. Workshop on THz, 2015, pp. 3–4.
[100] W. J. Otter, S. M. Hanham, N. M. Ridler, et al., "100 GHz ultrahigh Q-factor photonic crystal resonators," Sens. Actuators, A, vol. 217, pp. 151–159, 2014.
[101] S. M. Hanham, C. Watts, W. J. Otter, S. Lucyszyn, and N. Klein, "Dielectric measurements of nanoliter liquids with a photonic crystal resonator at terahertz frequencies," Appl. Phys. Lett., vol. 107, no. 3, pp. 032903–032907, 2015.
[102] S. M. Hanham, M. M. Ahmad, S. Lucyszyn, and N. Klein, "LED-Switchable high-Q packaged THz microbeam resonators," IEEE Trans. Terahertz Sci. Technol., vol. 7, no.2,pp. 199–208, 2017.

[103] K. Tsuruda, K. Okamoto, S. Diebold, S. Hisatake, M. Fujita, and T. Nagatsuma, "Terahertz sensing based on photonic crystal cavity and resonant tunneling diode," in Prog. Electromagn. Res. Symp. PIERS 2016 - Proc., 2016, pp. 3922–3926. https://doi.org/10.1109/PIERS.2016.7735476.
[104] K. Okamoto, K. Tsuruda, S. Diebold, S. Hisatake, M. Fujita, and T. Nagatsuma, "Terahertz sensor using photonic crystal cavity and resonant tunneling diodes," J. Infrared, Millim. Terahertz Waves, vol. 38, no. 9, pp. 1085–1097, 2017.
[105] P. B. Deotare, M. W. McCutcheon, I. W. Frank, M. Khan, and M. Lončar, "High quality factor photonic crystal nanobeam cavities," *Appl. Phys. Lett.*, vol. 94, no. 12, p. 121106, Mar. 2009, doi: 10.1063/1.3107263.
[106] Y. Akahane, T. Asano, B.-S. Song, and S. Noda, "High- Q photonic nanocavity in a two-dimensional photonic crystal," *Nature*, vol. 425, no. 6961, pp. 944–947, Oct. 2003, doi: 10.1038/nature02063.
[107] W. Xie *et al.*, "High-Q Photonic Crystal Nanocavities on 300 mm SOI Substrate Fabricated With 193 nm Immersion Lithography," *J. Light. Technol.*, vol. 32, no. 8, pp. 1457–1462, Apr. 2014.
[108] D. Yang, X. Chen, X. Zhang, C. Lan, and Y. Zhang, "High-Q, low-index-contrast photonic crystal nanofiber cavity for high sensitivity refractive index sensing," *Appl. Opt.*, vol. 57, no. 24, pp. 6958–6965, Aug. 2018, doi: 10.1364/AO.57.006958.
[109] P. Lalanne, C. Sauvan, and J. P. Hugonin, "Photon confinement in photonic crystal nanocavities," *Laser Photonics Rev.*, vol. 2, no. 6, pp. 514–526, 2008, doi: 10.1002/lpor.200810018.
[110] Q. Quan, P. B. Deotare, and M. Loncar, "Photonic crystal nanobeam cavity strongly coupled to the feeding waveguide," *Appl. Phys. Lett.*, vol. 96, no. 20, p. 203102, May 2010, doi: 10.1063/1.3429125.
[111] D. Yang, C. Wang, and Y. Ji, "Silicon on-chip 1D photonic crystal nanobeam bandstop filters for the parallel multiplexing of ultra-compact integrated sensor array," *Opt. Express*, vol. 24, no. 15, pp. 16267–16279, Jul. 2016, doi: 10.1364/OE.24.016267.
[112] E. Kuramochi, H. Taniyama, T. Tanabe, K. Kawasaki, Y.-G. Roh, and M. Notomi, "Ultrahigh-Q one-dimensional photonic crystal nanocavities with modulated mode-gap barriers on SiO2 claddings and on air claddings," *Opt. Express*, vol. 18, no. 15, pp. 15859–15869, Jul. 2010, doi: 10.1364/OE.18.015859.
[113] D. Englund *et al.*, "Deterministic Coupling of a Single Nitrogen Vacancy Center to a Photonic Crystal Cavity," *Nano Lett.*, vol. 10, no. 10, pp. 3922–3926, Oct. 2010, doi: 10.1021/nl101662v.
[114] A. Faraon, E. Waks, D. Englund, I. Fushman, and J. Vučković, "Efficient photonic crystal cavity-waveguide couplers," *Appl. Phys. Lett.*, vol. 90, no. 7, p. 073102, Feb. 2007, doi: 10.1063/1.2472534.

[115] Y. Akahane, T. Asano, B.-S. Song, and S. Noda, "High-Q photonic nanocavity in a two-dimensional photonic crystal," *Nature*, vol. 425, no. 6961, pp. 944–947, Oct. 2003, doi: 10.1038/nature02063.
[116] G. Manzacca, D. Paciotti, A. Marchese, M. S. Moreolo, and G. Cincotti, "2D photonic crystal cavity-based WDM multiplexer," *Photonics Nanostructures - Fundam. Appl.*, vol. 5, no. 4, pp. 164–170, Nov. 2007, doi: 10.1016/j.photonics.2007.03.003.
[117] Z. Zhang and M. Qiu, "Compact in-plane channel drop filter design using a single cavity with two degenerate modes in 2D photonic crystal slabs," *Opt. Express*, vol. 13, no. 7, p. 2596, Apr. 2005, doi: 10.1364/OPEX.13.002596.
[118] F. Gadot, A. de Lustrac, J.-M. Lourtioz, T. Brillat, A. Ammouche, and E. Akmansoy, "High-transmission defect modes in two-dimensional metallic photonic crystals," *J. Appl. Phys.*, vol. 85, no. 12, pp. 8499–8501, Jun. 1999, doi: 10.1063/1.370634.
[119] M. Bayindir, E. Cubukcu, I. Bulu, T. Tut, E. Ozbay, and C. M. Soukoulis, "Photonic band gaps, defect characteristics, and waveguiding in two-dimensional disordered dielectric and metallic photonic crystals," *Phys. Rev. B*, vol. 64, no. 19, p. 195113, Oct. 2001, doi: 10.1103/PhysRevB.64.195113.
[120] A. Serpenguzel, "Transmission characteristics of metallodielectric photonic crystals and resonators," *IEEE Microw. Wirel. Compon. Lett.*, vol. 12, no. 4, pp. 134–136, Apr. 2002, doi: 10.1109/7260.993292
[121] S. Lin, V. M. Hietala, S. K. Lyo, and A. Zaslavsky, "Photonic band gap quantum well and quantum box structures: A high-Q resonant cavity," *Appl. Phys. Lett.*, vol. 68, no. 23, pp. 3233–3235, Jun. 1996, doi: 10.1063/1.116558.

[122] E. Özbay, B. Temelkuran, M. Sigalas, G. Tuttle, C. M. Soukoulis, and K. M. Ho, "Defect structures in metallic photonic crystals," *Appl. Phys. Lett.*, vol. 69, no. 25, pp. 3797–3799, Dec. 1996, doi: 10.1063/1.117002.
[123] Y. Zhao and D. R. Grischkowsky, "2-D Terahertz Metallic Photonic Crystals in Parallel-Plate Waveguides," *IEEE Trans. Microw. Theory Tech.*, vol. 55, no. 4, pp. 656–663, Apr. 2007, doi: 10.1109/TMTT.2007.892798.
[124] A. L. Bingham and D. Grischkowsky, "Terahertz two-dimensional high-Q photonic crystal waveguide cavities," *Opt. Lett.*, vol. 33, no. 4, pp. 348–350, Feb. 2008, doi: 10.1364/OL.33.000348.
[125] S. M. Hanham, C. Watts, W. J. Otter, S. Lucyszyn, and N. Klein, "Dielectric measurements of nanoliter liquids with a photonic crystal resonator at terahertz frequencies," *Appl. Phys. Lett.*, vol. 107, no. 3, p. 032903, Jul. 2015, doi: 10.1063/1.4927242.
[126] K. Okamoto, K. Tsuruda, S. Diebold, S. Hisatake, M. Fujita, and T. Nagatsuma, "Terahertz Sensor Using Photonic Crystal Cavity and Resonant Tunneling Diodes," *J. Infrared Millim. Terahertz Waves*, vol. 38, no. 9, pp. 1085–1097, Sep. 2017, doi: 10.1007/s10762-017-0391-0.
[127] W. J. Otter, S. M. Hanham, N. M. Ridler, G. Marino, N. Klein, and S. Lucyszyn, "100GHz ultra-high Q-factor photonic crystal resonators," *Sens. Actuators Phys.*, vol. 217, pp. 151–159, Sep. 2014, doi: 10.1016/j.sna.2014.06.022.
[128] C. M. Yee and M. S. Sherwin, "High-Q terahertz microcavities in silicon photonic crystal slabs," *Appl. Phys. Lett.*, vol. 94, no. 15, p. 154104, Apr. 2009, doi: 10.1063/1.3118579.
[129] S. M. Hanham, M. M. Ahmad, S. Lucyszyn, and N. Klein, "LED-Switchable High-Q Packaged THz Microbeam Resonators," *IEEE Trans. Terahertz Sci. Technol.*, vol. 7, no. 2, pp. 199–208, Mar. 2017, doi: 10.1109/TTHZ.2016.2634547.
[130]A. Suminokura, T. Ishigaki, M. Fujita, and T. Nagatsuma, "Grating coupler for terahertz-wave integrated circuits using a
photonic-crystal slab," in Asia-Pacific Radio Science Conference (AP-RASC2013), Taipei, 2013, no. DJ2b-3, Sep. 6th.
[131]X. Yu, J. Y. Kim, M. Fujita, and T. Nagatsuma, "Highly stable terahertz resonant tunneling diode oscillator coupled to
photonic-crystal cavity," in Asia-Pacific Microw Conf. Proceedings (APMC), 2019, pp. 114–116.
[132]M. Asada, S. Suzuki, and N. Kishimoto, "Resonant tunneling diodes for sub-terahertz and terahertz oscillators," Jpn. J. Appl. Phys., vol. 47, no. 61, pp. 4375–4384, 2008.
[133] A. Suminokura, T. Ishigaki, M. Fujita, and T. Nagatsuma, "Grating coupler for terahertz-wave integrated circuits using a photonic-crystal slab," in Asia-Pacific Radio Science
[134] T. Ishigaki, M. Fujita, M. Nagai, M. Ashida, and T. Nagatsuma, "Photonic-crystal slab for terahertz-wave integrated circuits,"in IEEE Photonics Conf. IPC, 2012, pp. 774–775. https://doi.org/ 10.1109/IPCon.2012.6358852.
[135] W. Gao, X. Yu, M. Fujita, T. Nagatsuma, C. Fumeaux, and W. Withayachumnankul, "Effective-medium-cladded dielectric waveguides for terahertz waves," Opt. Express, vol. 27, no. 26, pp. 38721–38734, 2019.
[136] P. Cheben, R. Halir, J. H. Schmid, H. A. Atwater, and D. R. Smith, "Subwavelength integrated photonics," Nature, vol. 560,no. 7720, pp. 565–572, 2018.
[137] H. Mosallaei and Y. Rahmat-Samii, "Photonic band-gap (PBG) versus effective refractive index: a case study of dielectric nanocavities," in IEEE Antennas and Propagation Society International Symposium. Transmitting Waves of Progress to the Next Millennium. 2000 Digest. Held in conjunction with: USNC/URSI National Radio Science Meeting (Cat. No.00CH37118), 2000, pp. 338–341. https://doi.org/10.1109/APS.2000.873831.
[138] A. V. Subashiev and S. Luryi, "Modal control in semiconductor optical waveguides with uniaxially patterned layers," J. Lightwave Technol., vol. 24, no. 3, pp. 1513–1522, 2006.
[139] W. Gao, W. S. L. Lee, C. Fumeaux, and W. Withayachumnankul, "Effective-medium-clad Bragg grating filters," APL Photonics, vol. 6, no. 7, pp. 1–9, 2021.
[140] D. Headland, W. Withayachumnankul, R. Yamada, M. Fujita, and T. Nagatsuma, "Terahertz multi-beam antenna using photonic crystal waveguide and luneburg lens," APL Photonics, vol. 3, no. 12, pp. 126105–126122, 2018.
[141] D. Headland, M. Fujita, and T. Nagatsuma, "Half-Maxwell fisheye lens with photonic crystal waveguide for the integration of terahertz optics," Opt. Express, vol. 28, no. 2, pp. 2366–2380, 2020.

[142] D. Headland, A. K. Klein, M. Fujita, and T. Nagatsuma, “Dielectric slot-coupled half-Maxwell fisheye lens as octave bandwidth beam expander for terahertz-range applications,” APL Photonics, vol. 6, no. 9, pp. 096104–096115, 2021.
[143] R. A. S. D. Koala, D. Headland, Y. Yamagami, F. Masayuki, and T. Nagatsuma, “Broadband terahertz dielectric rod antenna array with integrated half-Maxwell fisheye lens,” in International Topical Meeting on Microwave Photonics (MWP), 2020, pp. 54–57.. 9314424.
[144] T. Sagisaka, Kaname R., Kikuchi M., et al., “Integrated terahertz optics with effective medium for 600-GHz-band imaging,” in International Topical Meeting on Microwave Photonics (MWP), 2020, pp. 62–65. https://doi.org/10.23919/mwp48676.2020. 9314570.
[145] L. Yi, Y. Nishida, T. Sagisaka, et al., “Towards practical terahertz imaging system with compact continuous-wave transceiver,” J. Lightwave Technol., vol. 39, no. 24, pp. 7850–7861, 2021.
[146]D. Headland, W. Withayachumnankul, X. Yu, M. Fujita, and T. Nagatsuma, “Unclad microphotonics for terahertz waveguides and systems,” J. Lightwave Technol., vol. 38, no. 24, pp. 6853–6862, 2020.
[147] H. T. Zhu, Q. Xue, J. N. Hui, and S. W. Pang, “Design, fabrication, and measurement of the low-loss SOI-based dielectric microstrip line and its components,” IEEE Trans. Terahertz Sci. Technol., vol. 6, no. 5, pp. 696–705, 2016.
[148] H. Amarloo, N. Ranjkesh, and S. A. Safavi-Naeini, “Terahertz silicon-BCB-quartz dielectric waveguide: an efficient platform for compact THz systems,” IEEE Trans. Terahertz Sci. Technol., vol. 8, no. 2, pp. 201–208, 2018.
[149] H. Amarloo and S. Safavi-Naeini, “Terahertz line defect waveguide based on silicon-on-glass technology,” IEEE Trans. Terahertz Sci. Technol., vol. 7, no. 4, pp. 433–439, 2017.
[150] N. Ranjkesh, S. Gigoyan, H. Amarloo, M. Basha, and S. Safavi-Naeini, “Broadband single-mode THz suspended silicon-on glass waveguide,” IEEE Microw. Wireless Compon. Lett., vol. 28, no. 3, pp. 185–187, 2018.
[151] E. Akiki, M. Verstuyft, B. Kuyken, et al., “High-Q THz photonic crystal cavity on a low-loss suspended silicon platform,” IEEE Trans. Terahertz Sci. Technol., vol. 11, no. 1, pp. 42–53, 2021.
[152] A. Suminokura, K. Tsuruda, T. Mukai, M. Fujita, and T. Nagatsuma, “Integration of resonant tunneling diode with terahertz photonic-crystal waveguide and its application to gigabit terahertz-wave communications,” in International Topical Meeting on Microwave Photonics (MWP), 2014
[153] X. Yu, J.-Y. Kim, M. Fujita, and T. Nagatsuma, “Efficient mode converter to deep-sub wavelength region with photonic-crystal waveguide platform for terahertz applications,” Opt. Express, vol. 27, no. 20, pp. 28707–287021, 2019.
[154] X. Yu, T. Ohira, J. Y. Kim, M. Fujita, and T. Nagatsuma, “Waveguide-input resonant tunnelling diode mixer for THz communications,” Electron. Lett., vol. 56, no. 7, pp. 342–344, 2020.
[155] A. E. Torres-Garcia, J. M. Perez-Escudero, J. Teniente, R. Gonzalo, and I. Ederra, “Silicon integrated subharmonic mixer on a photonic-crystal platform,” IEEE Trans. Terahertz Sci. Technol., vol. 11, no. 1, pp. 79–89, 2021.
[156] N. Shibata, Y. Uemura, Y. Kawamoto, L. Yi, M. Fujita, and T. Nagatsuma, “600-GHz-band silicon dielectric waveguide module,” Int. Conf. Infrared Millim. Terahertz Waves, pp. 1–2, 2021. https://doi.org/10.1109/IRMMW-THz50926.2021. 9567463
[157] Y. Kawamoto, N. Shibata, Y. Uemura, et al., “Integrated resonant tunneling diode with rectangular waveguide I/O using photonic crystal interface,” Int. Conf. Infrared Millim. Terahertz Waves, pp. 1–2, 2021. https://doi.org/10.1109/ IRMMW-THz50926.2021.956746310.1109/irmmw-thz50926. 2021.9567393.
[158] N. Shibata, Y. Uemura, Y. Kawamoto, L. Yi, M. Fujita, and T. Nagatsuma, “600-GHz-band silicon dielectric waveguide module,” Int. Conf. Infrared Millim. Terahertz Waves, pp. 1–2, 2021. https://doi.org/10.1109/IRMMW-THz50926.2021. 9567463.
[159] D. Headland, M. Fujita, and T. Nagatsuma, “Bragg-mirror suppression for enhanced bandwidth in terahertz photonic crystal waveguides,” IEEE J. Sel. Top. Quant. Electron., vol. 26, no. 2, pp. 1–9, 2019.
[160] Y. Yang, Y. Yamagami, X. Yu, et al., “Terahertz topological photonics for on-chip communication,” Nat. Photonics, vol. 14, no. 7, pp. 446–451, 2020.
[161] J. Webber, Y. Yamagami, G. Ducournau, et al., “Terahertz band communications with topological valley photonic crystal waveguide,” J. Lightwave Technol., vol. 39, no. 24, pp. 7609–7620, 2021.

[162] R. Koala, D. Headland, X. Yu, Y. Nishida, M. Fujita, and T. Nagatsuma, “Terahertz RTD chip backside-coupled to photonic-crystal waveguide,” Int. Conf. Infrared Millim. Terahertz Waves, pp. 1–2, 2021. https://doi.org/10.1109/ IRMMW-THz50926.2021.9567199
[163]. Rajan, R., Babu, P., & Senthilnathan, K. (2018, April 01). All-optical logic gates show promise for optical computing. Photonics Spectra, 52, 62-65.

Chapter II:

THz Topological Devices: Design and Numerical Studies

Topological photonics is a rapidly growing field that has gained significant attention for its innovative ways of manipulating the flow of light. Through topological protection, the surface modes of topological photonic systems offer unique properties, such as unidirectional propagation and robust transmission against defects and disorders, which have become increasingly important for information processing. Among the different Photonic topological insulator (PTI) systems, valley PTIs have gained particularly high interest as a type of topological photonic system that not only supports protected surface modes but is also amenable to micro-nano fabrication, making it highly suitable for miniaturized integrated photonic circuit designs. These advantages make Valley photonic crystals a promising platform for constructing high-performance photonic devices for future 6G data communication systems and beyond.

In this chapter, we will discuss the theory design and numerical simulations for our terahertz (THz) passive functional devices such as waveguides, resonators, and double cavity resonators based on valley photonic topological insulators (PTIs).

II.1 Emergence of topological photonics: A short introduction

PTIs are a subset of photonic crystals (PhCs), however, they take inspiration from solid-state physics but focus on electromagnetic waves instead of electrons [1-2]. PTIs find their origin from electronic topological insulators (TIs), which are insulators within the bulk but allow electrons to propagate along the edge of the system. The "topological" aspect of TIs comes from the global topology of their energy band structure, which can be categorized by an integer that does not depend on the fine details of the system. The quantum Hall effect (QHE), discovered in the 1980s, showed that the conductivity of a two-dimensional material is fundamentally discrete and can be explained by a special phase that each electron accumulates as it orbits in cyclotron motion in the reciprocal space [3]-[4]. The discrete nature of the conductance is highly robust to deformations to the bulk of the material and can be shown to be tied directly to the mathematical framework of topological invariants (see Fig.II. 1) [5]. This framework gives us a simple means to classify materials and results in the technologically useful effects that topological insulators can offer [6]-[7].

Non-trivial materials refer to substances that exhibit unique electronic or photonic properties, particularly in their band structure. In the context of PTIs, non-trivial materials are those with

non-zero topological invariants, leading to the presence of protected edge modes within their band gaps. These edge modes are highly robust transport channels where photons can propagate unidirectionally without scattering back, even in the presence of defects or disorder [16].

Highly robust transport modes, called edge modes, exist within the bandgap of non-trivial materials, and electrons moving along these boundaries must do so in one direction only, with no possibility of scattering back in the other direction [8]. The quantization of conductivity in the QHE gives rise to edge modes, which have been consistently observed in various material samples during multiple experiments, even in the presence of impurities [9]. These edge modes are topologically "protected" and guaranteed to exist so long as the invariant stays the same. This has to be related to the fact that topological phase transition must occur in order to change the topological invariant, and in QHE, the system is not invariant by time-reversal symmetry due to the applied. These discoveries have led to the Nobel Prize in Physics being awarded to Thouless, Haldane, and Kosterlitz in 2016. These systems with topological behavior are a consequence of the wave nature of the electrons, not specifically their quantum interactions [10]. As a result, it is possible in some cases to construct classical wave systems with analogous properties to their electronic counterparts. This opened the door to demonstrations that PTIs, can also have many of the features of TIs [2].

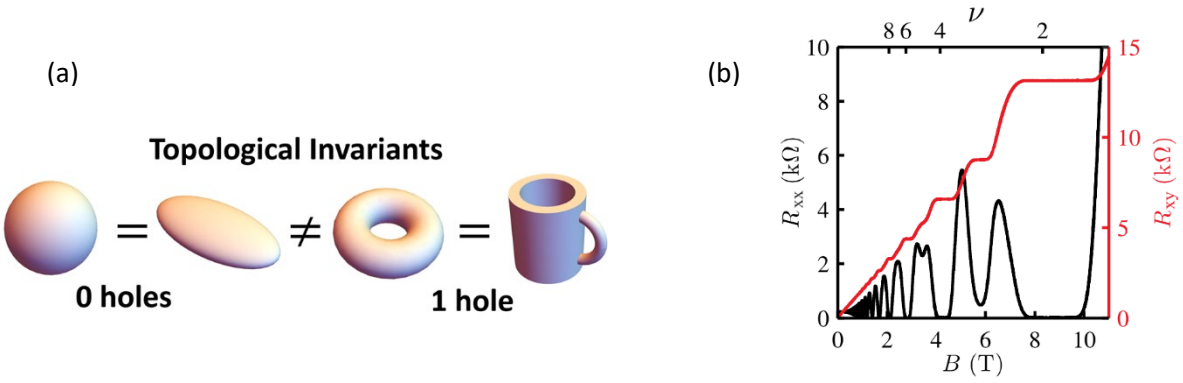

Figure.II.1: (a) Mathematical illustration of topological invariance concept [16]. (b) Graphical representation of the integer "Quantum Hall effect". As the average density is varied, the Hall conductance σH appears to form plateaus at integer filling fractions ν=1,2,3… [42].

This next section introduces the fundamental idea of the geometric phase and applies it to periodic systems, where topological properties can arise. The focus is on 2D PhCs and how the Chern numbers and topological transitions can have important physical implications. Furthermore, the formation of degeneracy points (Dirac points) in PhCs and the different mechanisms that introduce topological phases, can lead to various types of PTIs.

II.1.1 Geometric Phase

The fundamental concept underlying topological effects in diverse fields is the geometric phase. It arises universally when a system's parameter undergoes gradual variation within a closed cycle [11]. Pancharatnam initially introduced this phase in 1956 to explain the propagation of light through a series of polarizers [12], and later Berry extended and generalized it to the realm of quantum mechanics [13]. Many things in physics can be attributed to the geometric phase [14-15].

When a wave is characterized by its amplitude (denoted as E) and ordinary phase (ϕ) at a specific position and time, the expectation would be that upon slowly changing the values of position and time from $\boldsymbol{r}$ and t to distinct intermediate values $\boldsymbol{r}'$ and t', then smoothly reverting to $\boldsymbol{r}$ and t, the initial value of $E(\boldsymbol{r},t)$ would match the final value. However, in certain important cases, this intuition fails. For instance, when considering a tangent vector moved along a closed path on a sphere and returned to the starting position, its orientation no longer aligns with the initial direction. This discrepancy in orientation, illustrated in Figure II.2, results in a rotation angle ϕ, such as $\pi/2$ in the depicted scenario. This phenomenon arises due to the curvature of the closed loop, which encloses a geometric area (denoted as Ω) in parameter space, leading to the addition of a phase termed the "geometric phase.". In the context of a sphere representing wavevector $\boldsymbol{k}$ and the vector representing the $\boldsymbol{E}$ field, this parallel transport elucidates the change in polarization observed in helical and bent waveguides. For example, in a bent waveguide scenario where polarized light gradually shifts direction from z to $-x$, then from $-x$ to y, and finally back to z, the wave accumulates a geometric phase that modifies the phase difference between the two degenerate modes. In simpler terms, when the electric field vector follows a straight path without rotating as it moves along a curved surface, it adds a geometric phase. A geometric phase can arise when a state gradually varies in different types of parameter spaces, including the momentum space of periodic systems such as PhC [17]. The field of topological insulators extensively employs specialized terminology, much of which pertains to

mathematical constructs used to identify non-trivial topological invariants. Fortunately, these constructs often have parallels in standard electromagnetic theory, offering straightforward approaches to numerically computing topological properties of real systems.

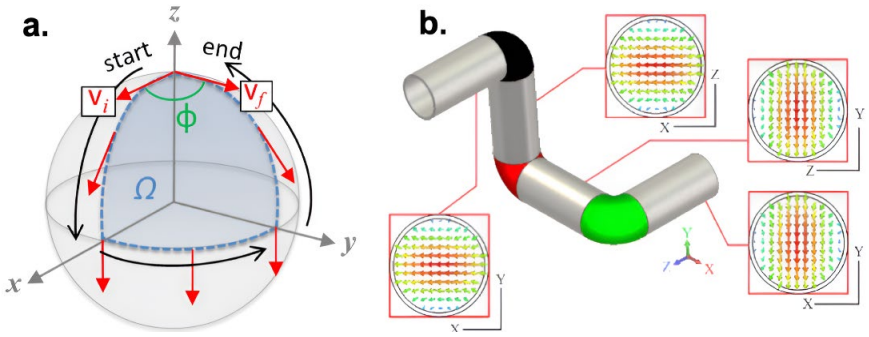

Figure: II.2 : (a) Geometric phase from parallel transport. b. The polarization (shown as the vector E field inset at different locations) in a bent circular waveguide shows that as the propagation path is varied, and then returned to its initial state, there can be a phase shift to the polarization state, which is due to the geometric phase [16].

II.1.2 Berry Phase

Consider a lattice described by a general eigenvalue problem in momentum space:

$$\mathrm{H}(\mathbf{k}) \cdot \mathbf{F_n}(\mathbf{k}) = \lambda_\mathrm{n}(\mathbf{k})\mathbf{F_n}(\mathbf{k}) \qquad \text{(II.1)}$$

Here, $\lambda_\mathrm{n}(\mathbf{k})$ represents the eigenenergy, and $\boldsymbol{F_n(k)}$ is the normalized eigenwave function of *H(k)* (commonly referred to as the "Hamiltonian" in literature). **k** for the nth band can be obtained via Bloch's theorem. A schematic representation is shown in Fig II.3. $\lambda_1, \lambda_2 and\ \lambda_3$ are the three eigen values corresponding to the three eigenenergy states that can be calculated from **H**. The shorthand notation for the inner product:

$$\langle \boldsymbol{A}(\mathbf{r}) | \boldsymbol{B}(\mathbf{r}) \rangle \equiv \int \boldsymbol{A}(\mathbf{r})^\dagger \cdot \boldsymbol{B}(\mathbf{r})\, d\mathrm{r} \qquad \text{(II.2)}$$

denotes the integration of two vector functions **A** and **B** over the variable **r**, with † representing Hermitian conjugation. Thus, "normalized" in this context implies

$$\langle\, \boldsymbol{F_n(k)} \mid \boldsymbol{F_n(k)} \,\rangle = 1$$

Gradually varying **k** along a given energy band induces a phase accumulation associated with the slow evolution of $\boldsymbol{F_n(k)}$. In most cases, when **k** returns to its initial point, this accumulation results in zero total phase. However, certain special cases, as illustrated in the previous section, may lead to a non-zero geometric phase.

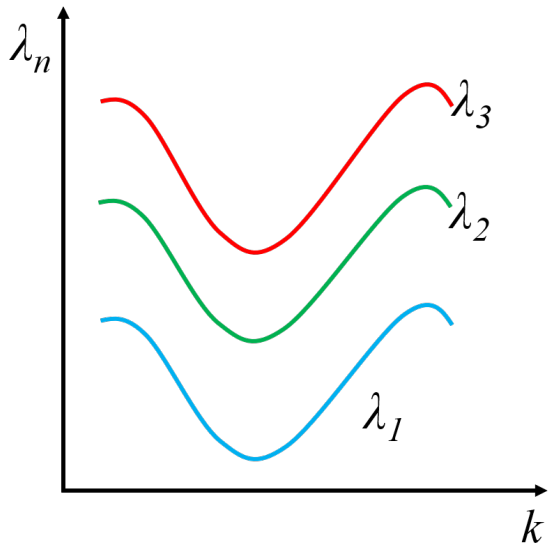

Figure II.3: Visualization of the relationship between the eigenvalue λ and the momentum vector k in a two-dimensional graph. The x-axis represents the components of the momentum vector k, while the y-axis represents the corresponding eigenvalues λ. The curves on the graph depict the relationship between λ and k, determined by the form of the Hamiltonian H(k) and the corresponding eigenvalue problem. Depending on the system's complexity, these curves may intersect or exhibit other interesting features.

In the literature on topological insulators, this geometric phase is commonly referred to as the Berry phase, reflecting Berry's formulation in quantum mechanics [13]. To compute the overall Berry phase, it's necessary to aggregate the phase contributions resulting from incremental changes in the wave function. The phase difference between two *F* states of the same band that is infinitesimally separated by Δk can be depicted through their inner product, shown in Fig.II.4 [16]. This inner product can be expanded into a low-order Taylor series, thus allowing us to approximate the phase shift,

The inner product $\langle \boldsymbol{F_n(k)} | \boldsymbol{F_n(k+\Delta k)} \rangle$ can be approximated as:

$$\langle \boldsymbol{F_n(k)} | \boldsymbol{F_n(k+\Delta k)} \rangle \approx 1 + \boldsymbol{\Delta k} \langle \boldsymbol{F_n(k)} | \nabla_{\mathbf{k}} | \boldsymbol{F_n(k)} \rangle$$

$$= \exp\left(-i \boldsymbol{\Delta k} \cdot \boldsymbol{A_F(k)}\right) \qquad \text{(II. 3)}$$

In this expression, $\boldsymbol{\Delta k} \cdot \boldsymbol{A_F(k)}$ represents the phase shift over $\boldsymbol{\Delta k}$, and $\boldsymbol{A_F(k)}$ is the rate of change of the phase shift.

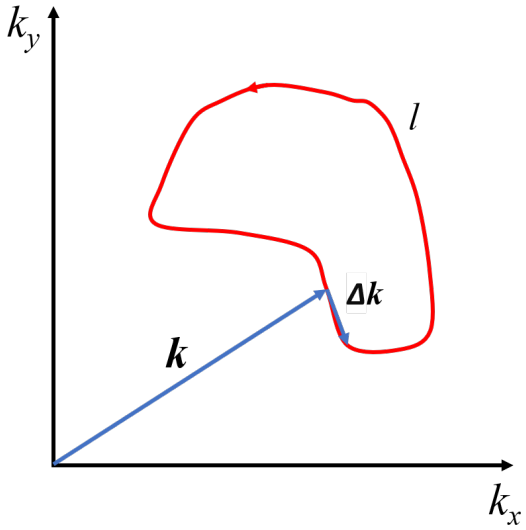

Figure II.4: Illustration showing the phase difference between two F states of the same band, infinitesimally separated by Δk.

$A_F(k)$ is commonly known as the Berry connection or Berry vector potential, defined as:

$$A_n(k) = i\langle F_n(k)|\nabla_k|F_n(k)\rangle \qquad \text{(II.4)}$$

The Berry phase for the n th band is defined as the integral of $\mathbf{A_n}(k)\big)$ over some closed path (l) in (k)-space, noted as

$$\phi(n) = \left(\oint_l A_n(k) \cdot dk\right) \qquad \text{(II.5)}$$

This integral encapsulates the geometric phase acquired by the wave function $F_n(k)$ as it traverses the Brillouin zone. It serves as a crucial descriptor in understanding the topological properties of quantum systems, providing insights into phenomena such as quantum Hall effects and topological insulators.

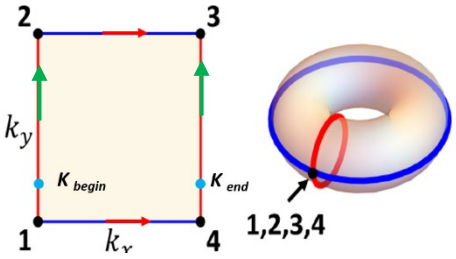

Figure. II.5. The Brillouin zone of a 2D can be considered as a torus by taking each periodic boundary (red and blue in the figure) and connecting them together lattice with the same orientation (no twist) [16].

The path (l) is simply a smooth curve of values over the Brillouin Zone (BZ), as illustrated by the blue and red lines in Fig. II.5. When we know a given wavefunction within the Brillouin zone, we can utilize this information to calculate the Berry phase along that path. However, the Bery connection ($\boldsymbol{A_F(k)}$) is not gauge-invariant means not uniquely defined. If we introduce a phase change ($\zeta(\boldsymbol{k})$) to the eigen wavefunction ($\boldsymbol{F(k)}$), where ($\zeta(\boldsymbol{k})$) is a periodic function satisfying $\zeta(\boldsymbol{k_{end}}) = \zeta\left(\boldsymbol{k_{begin}}\right) + 2m\pi$, the resulting new wavefunction $e^{i\zeta(\boldsymbol{k})}F(\boldsymbol{k})$ remains an eigen wavefunction of ($H(\boldsymbol{k})$). Where $\boldsymbol{k}_{\boldsymbol{begin}}$ and $\boldsymbol{k_{end}}$ are two different vecrors in reciprocal lattice. However, the Berry connection undergoes a transformation$\left(\boldsymbol{A_n(k)} \rightarrow \boldsymbol{A_n(k)} - \frac{d}{d\boldsymbol{k}}\zeta(\boldsymbol{k})\right)$, altering its formula with different choices of $\zeta(\boldsymbol{k})$. However, the Berry phase remains invariant modulo (2π), denoted as

$$\left(\oint_l d\boldsymbol{k}\cdot\boldsymbol{A_n(k)} \rightarrow \oint_l dk\cdot\boldsymbol{A_n(k)} - \oint_l dk\frac{\partial}{\partial\boldsymbol{k}}\zeta(\boldsymbol{k}) \rightarrow \oint_l d\boldsymbol{k}\cdot\boldsymbol{A_n(k)} - 2\mathrm{m}\pi\right) \quad (6)$$

This invariance can be qualitatively understood as the wavevector (k) slowly traverses the band loop, eventually returning to its starting point and acquiring a phase multiple of 2π, with most systems accumulating zero phase. Since the Berry connection depends on how the calculation is set up, yet the Berry phase should not, it is advantageous (particularly for numerical purposes) to define a quantity invariant to any arbitrary phase ($\zeta(\boldsymbol{k})$) added. This invariant quantity is the Berry curvature or Berry flux, constructed by taking the curl of the Berry connection.

$$\boldsymbol{\Omega_F(k)} = \boldsymbol{\nabla_k} \times \boldsymbol{A_n(k)} \quad (7)$$

Utilizing Stokes' theorem, the Berry phase can then be expressed as the integral of the Berry curvature over the surface bounded by the path (l).

$$\phi_F = \oint_s d^2\,\mathbf{k}\cdot\boldsymbol{\Omega_F(k)} \quad (8)$$

Here, ϕ_F represents the Berry phase, which is calculated as the line integral of the Berry curvature $\boldsymbol{\Omega_F(k)}$ over the surface bounded by the path (l) [16].

II.1.3 Chern Number

By using the Berry curvature, the existence of topological edge modes, can be understood from non-zero value of an invariant which is referred to as the Chern number, which was named after Shiing-Shen Chern, a Chinese-American mathematician [16]. The Chern number is always an integer value. If the Chern number is non-zero, it indicates that the 2D photonic system is topologically nontrivial. The Chern number of the nth band of a 2D lattice is simply the integral of Berry curvature phase over the full Brillouin zone normalized to 2π.

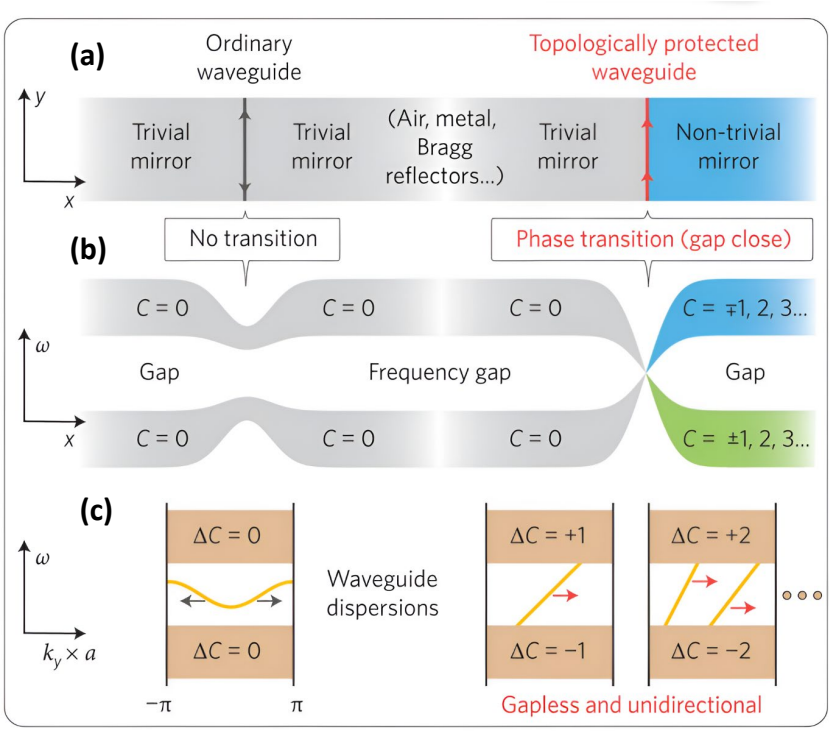

Figure II.6: Topological invariance interpretation using Chern number C (**a**) Two waveguides formed by mirrors of different (top right) and same (top-left) topologies. (**b**) Frequency bands of different topologies cannot transition into each other without closing the frequency gap. A topological phase transition takes place on the right, but not on the left. **(c)** Interfacial states have different connectivity with the bulk bands, depending on the band topologies of the bulk mirrors. Here, a is the period of the waveguide propagating along y, and ΔC is the change in Chern number between the corresponding bulk bands on the right and left of the waveguide. The magnitude of ΔC equals the number of gapless interfacial modes and the sign of ΔC indicates the direction of propagation [18]

The equation can be properly written as:

$$C_n = \frac{1}{2\pi}\int_{\text{Brillouin Zone}} d^2\, \boldsymbol{k\Omega_n}(k_x, k_y) \qquad \text{(II.9)}$$

The Chern number characterizes the topology of a band and describes topologically "protected" edge states that appear at the interface between two structures with unequal Chern numbers. When two ordinary insulators are connected to form a traditional photonic waveguide, a trivial edge state is formed with a Chern number of zero as shown in Fig II.6 left a, b, and c. However, when two topologically inequivalent structures are connected (at least one structure has a non-zero Chern number), a nontrivial edge waveguide is formed (Fig II.6 a, right) because when the two domains with different topological invariants are connected directly to form an interface, a topological phase transition must occur at the interface as shown in the Fig II.6 (b) [2] and the interface must be conductive. Moreover, those edge modes are in general immune to defects and backscattering at sharp bends which is not the case in trivial waveguides.

II.1.4 Topological Phase Transitions and Chern Numbers

A topological phase transition is a process by which a system changes its topological invariant [2,18]. Systems with different topological invariants cannot change into each other without a phase transition. In periodic systems, this occurs when a bandgap closes, which is marked by a change in the Chern number. In PhCs, a topological transition is usually induced by changes in symmetry or geometry of the PhC unit cell which will be detailed in the next section.

Essentially, the difference in topologies means that the respective bands in each bandgap material cannot be continuously transformed into one another. To transform one into the other, the frequency gap must first close at the interface and then reopen on the other side. This phase transition gives rise to the gapless edge states at the interface as demonstrated in Fig II.b, on the right.

To account for the jump in the Chern number's integer value, for example, from 1 to 0 or 1 to -1, etc., the number of gapless edge modes turns out to be the difference of the Chern numbers across the interface, refer to Fig II.4 [19]. This is known as the bulk-edge correspondence [2]. These gapless modes are tied to the bulk hern numbers, so they are robust and must always exist, regardless of the specific shape of the boundary (unlike conventional waveguides).

It's important to note that the modes in question are different from those found in regular PhC waveguides, which can also be highly robust with the primary difference being that their immunity to certain scatterings is a global property of bult not arise from any specific arrangement of PhC cells. [20].

II.1.5 Chern PTIs

In general, periodic structures like photonic crystals (PhCs) typically have a Chern number of zero [2]. This is related to time-reversal symmetry (TRS). In normal photonic crystals (PhCs), the Chern number, denoted as (C), quantifies the topological properties of the band structure. To establish that the Chern number is zero in such systems, we invoke the fundamental principle of time-reversal symmetry (TRS). Importantly, the Berry curvature, which governs the topology of the system, is odd under time reversal, i.e., $(\Omega(-k) = -\Omega(k))$. Consequently, when integrating the Berry curvature over the Brillouin zone, the contributions from positive and negative energy states cancel each other out pairwise due to TRS. Therefore, the integral of the Berry curvature, and consequently the Chern number (C), vanishes in normal PhCs. This rigorous proof underscores the profound influence of time-reversal symmetry on the topological properties of photonic crystal systems.

However, to engineer one with a non-zero Chern number, two key steps are essential: firstly, identifying a degenerate point between bands, and secondly, breaking a symmetry to open a bandgap near that point. This process is crucial for creating Chern Photonic Topological Insulators (PTIs). The first step involves finding degeneracies, which is significant because a material can only undergo a topological phase transition when two or more photonic bands degenerate at a point. This robustness of edge modes arises from the abrupt nature of the Chern number, where even small structural changes maintaining the bulk bandgap won't affect the mode. While finding degeneracies in PhCs is common, the second step, involving breaking symmetry to open a bandgap, imposes certain restrictions on the degeneracies useful for constructing a PTI [2].

The most relevant symmetry for Electromagnetic (EM) systems is Time Reversal Symmetry (TRS), where time reversal results in a reversal of the response $(t \rightarrow -t)$, (for example in the absence of an external magnetic field $\boldsymbol{H}$) and spatial inversion symmetry (SIS), where flipping the coordinate axes preserves the unit cell's shape and orientation $(\boldsymbol{r} \rightarrow -\boldsymbol{r})$. The simplest type

of degenerate point for PTIs is a linear crossing of two bands, often termed a "Dirac cone" [4]. Such a crossing can be achieved through a PhC in a honeycomb lattice (detailed in next section), where the degenerate point typically occurs at the K high symmetry point in the Brillouin Zone (BZ) [1]. However, it's not strictly necessary to form a linear-type degeneracy; other types like quadratic or accidental degeneracies can also suffice [21, 22].

To illustrate this process with a real device, we can examine the example of Wang et al. [23], which was later developed into the first experimental demonstration of a Chern PTI [24]. Initially, to establish the degenerate point, a square lattice of circular rods (chosen to be yttrium-iron-garnet, YIG) is employed, and the geometry is adjusted to achieve a quadratic crossing of the 2nd and 3rd bands at the M point [23]. Although there's also a degeneracy at the Γ point for the 3rd and 4th bands, the focus here is on the quadratic M point, shown in Fig II.7.

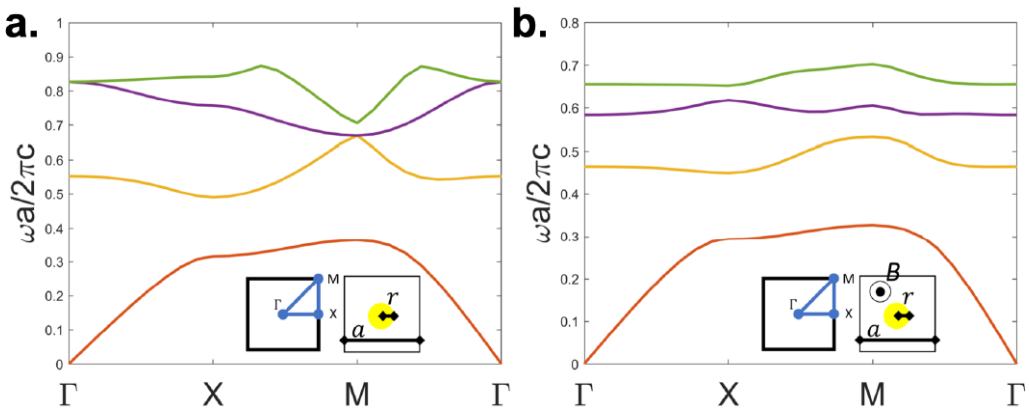

Figure II.7: Band diagram for the square lattice of (a.) un-magnetized, (b). magnetized YIG rods in air. Inset left: BZ path, right: unit cell with $r = 0.11a$ [16].

Subsequently, to open a complete bandgap near the degeneracy, a symmetry must be broken. The primary symmetries in the system are Time Reversal Symmetry (TRS) and Spatial Inversion Symmetry (SIS). Breaking either can induce a bandgap, but breaking TRS results in a non-zero Chern number of those bands, leading to the desired edge modes [25]. Following Wang et al.'s methodology, TRS is broken by applying a static magnetic field perpendicular to the 2D plane.

II.1.6 Honeycomb lattice and Brillouin zone

The honeycomb lattice, a unique variation of the hexagonal lattice, possesses a distinctive two-atom basis structure. Within this lattice, the hexagon centers form yet another hexagonal lattice, while the honeycomb lattice itself can be envisioned as the combination of two slightly offset triangular lattices. This lattice arrangement finds a remarkable manifestation in the natural world through the atomic configuration of graphene, a two-dimensional material where carbon atoms are intricately arranged in a honeycomb lattice pattern.

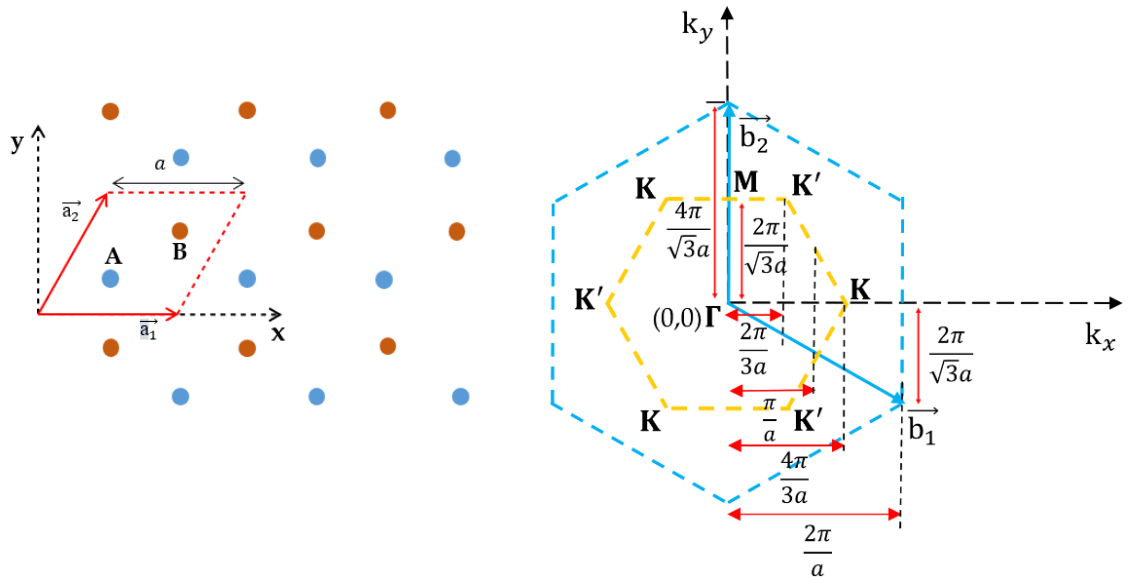

Figure II.8: (a) Schematic of honey comb hexagonal lattice in real space. (b) illustration of Brillouin zone and symmetry points k and K' represents symmetry points b1 and b2 are lattice vectors. Yellow short lines represent First Brillouin zone

In a hexagonal honeycomb lattice in real space shown in Fig II.8(a), the lattice parameters are typically described in terms of two lattice vectors, conventionally denoted as $\mathbf{a}_1$ and $\mathbf{a}_2$. These vectors represent the translation from one lattice point to its neighboring lattice points. These lattice vectors define the unit cell of the lattice. The lattice constant, denoted by a, represents the distance between neighboring lattice points within the unit cell.

Each unit cell contains two atoms, often distinguished as atom 1 and atom 2. These atoms are arranged in a repeating pattern within the lattice. In graphical representations here, atom 1 is depicted in blue color, while atom 2 is depicted in orange color. The lattice parameters, along with the arrangement of atoms within the unit cell, play a crucial role in determining the structural and electronic properties of materials with hexagonal honeycomb lattice structures, such as graphene. It is important to note that the Brillouin zone is defined as a Wigner-Seitz

primitive cell within the reciprocal lattice. Essentially, it is the smallest volume that is enclosed by planes formed by the perpendicular bisectors of the reciprocal lattice vectors originating from the center of the lattice shown in Fig II.8 (b). In simpler terms, the Brillouin zone of a honeycomb lattice is a hexagonal region in reciprocal space that encompasses all of the possible momentum states for particles within that lattice structure.

II.1.7 Valley PTIs

Like in Chern PTIs explained in the last section, the most common symmetry-breaking mechanism utilized is Time Reversal Symmetry (TRS), which is broken by gyrotropic materials under an applied magnetic field. However, the requirement for magneto-optical materials and external magnetic fields imposes practical limitations [26]. Valley PTIs offer an alternative approach. These PTIs retain similar robustness to disorder or sharp turns as Chern PTIs but remain reciprocal. Valley PTIs exploit an intrinsic degree of freedom in hexagonal lattices known as the "valley degree of freedom." In these structures, the angular rotation of the electric fields at high-symmetry points K or K' generates an intrinsic magnetic moment, mimicking the behavior observed in graphene-like materials. In most of the cases, the intrinsic magnetic moment is generated by breaking inversion symmetry. For example, consider the design of on-chip THz VPCs which was reported in 2021 [34] as shown in Fig II.9.

The VPC design is based on well well-known graphene-like lattice with lattice constant $a = 242.5$ μm Fig II.8. Unit cells comprise an equilateral triangular hole with a side length of l_1 and another inverted equilateral triangular hole with a side length of l_2. Here we only focus on transverse-electric modes, where electric fields lie within the plane. The modes propagate in the x–y plane but are confined in the z direction concerning total internal reflection. In the presence of inversion symmetry (for example, $l_1 = l_2 = 0.5a$), our VPC possesses C_6 symmetry that leads to a pair of degenerate Dirac points (at the K and K′ valleys) in the band diagram at 0.33 THz (Fig. II.9 b).

Upon breaking the inversion symmetry (for example, $l_1 = 0.65a$ and $l_2 = 0.35a$), the VPC structure reduces to C_3 symmetry, resulting in the lifting of degeneracy and the disappearance of Dirac points. More importantly, inversion symmetry breaking opens a bandgap (0.32 THz $< f <$ 0.35 THz) near the Dirac frequency as shown in Fig. II.9b. The distribution of the z-oriented magnetic field Hz and Poynting power flow of the modes at the K (K′) valley for both bands are shown in Fig. II.9c. It can be seen that four modes exhibit either left-handed circular

polarization (LCP) or right-handed circular polarization (RCP). Also, within the same band, the polarization of a mode at K′ is opposite to that of a mode at K.

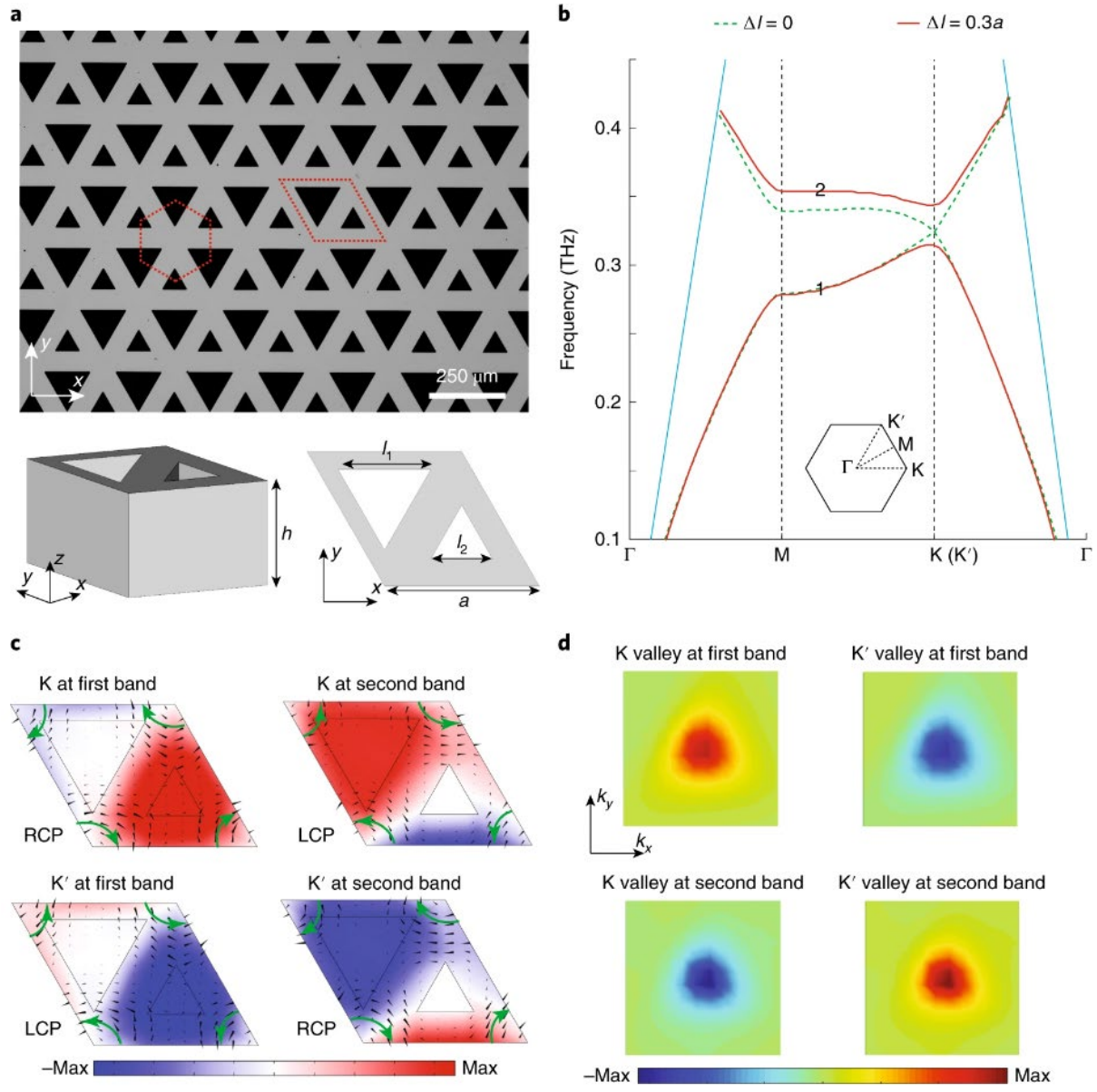

Figure II.9:(a) An optical image of the fabricated VPC. The red dashed lines show Wigner–Seitz and unit cells. Magnified views of the unit cell are presented below the optical image. (b), Band diagrams with and without inversion symmetry. The green, red and blue lines represent the dispersion of the VPC with and without inversion symmetry, and the light line of air, respectively. (c) Mode profiles at the K and K′ valleys for the first and second bands of the VPC. The colour scale shows the *z*-oriented magnetic field H_z, while the black and green arrows denote the Poynting power flow. (d) Normalized simulated Berry curvatures near the K and K′ valleys for both bands. The plotted range for each inset is $[-0.33\pi/a, 0.33\pi/a]^2$, centred at the K or K′ valleys [34]

Indeed, non-zero Berry curvatures that are localized around different valleys are shown in Fig. II.9d. Additionally, within the same band, these Berry curvatures are identical but opposite in sign for the K and K′ valleys. Therefore, the net integrated Berry curvature of any single band over the whole Brillouin zone is zero. Hence the TRS is preserved. Integrating Berry

curvatures around different valleys, valley Chern numbers are found to be different from zero, In the case of a very small gap (much smaller than the width), they are half-integers, that is in this case, $C\mathrm{K} = 1/2$ and $C\mathrm{K}' = -1/2$ for the first band and $C\mathrm{K} = -1/2$ and $C\mathrm{K}' = 1/2$ for the second band.

The evolution of eigenfrequencies at the K valley for both bands as a function of Δl ($\Delta l = l_1 - l_2$) was numerically obtained to visualize the valley Hall topological phase transition (Fig. II.10a). As seen in Fig. II.10a, the obtained results confirm that the polarization of the states gets reversed in the phase diagram when Δl crosses zero. On the left side, LCP is below and RCP is above ($\Delta l < 0$) in Fig. II.10a, whereas on the right side, the polarization inverts to LCP above and RCP below ($\Delta l > 0$). It is indicated by this inversion that two topologically different valley Hall phases are directly related to the sign of Δl.

'Kink'-type domain wall was constructed between two valley photonic crystals (VPCs) with opposite Δl values, as shown in Figure II.10(b). The difference of the valley Chern numbers across the domain wall at the K (K') valley was found to be $C\Delta = \pm 1$ (Figure II.10(c). According to the bulk-boundary correspondence, a pair of valley-polarized topological kink states appeared at the domain wall within the bandgap: one locked to the K valley propagated forward, while the other one, locked to the K' valley, propagated backward. As shown in Figure II.9(d), simulation results were consistent with this prediction. Furthermore, there was only a single kink state in the bandgap for a certain wavevector owing to the condition $|C\Delta| = 1$. The linear dispersion and single-mode properties of valley kink states were advantageous for THz communication. The linear dispersion indicated a negligible signal delay at different frequencies, which enabled a larger bandwidth. On the other hand, the single-mode feature precluded mode competition and provided additional advantages similar to those of a single-mode optical fiber. It was also revealed that the valley kink states were generally robust against fabrication imperfections, as long as these defects did not couple the states of the different valleys. Therefore, the present design had substantial advantages in comparison to the other existing THz waveguides It was worth noting that the relative size of the VPC bandgap could be tuned by changing the Δl parameter (Figure II.10(a)), and the operational frequency of the VPC could be tuned by a simple scaling of the unit cell.

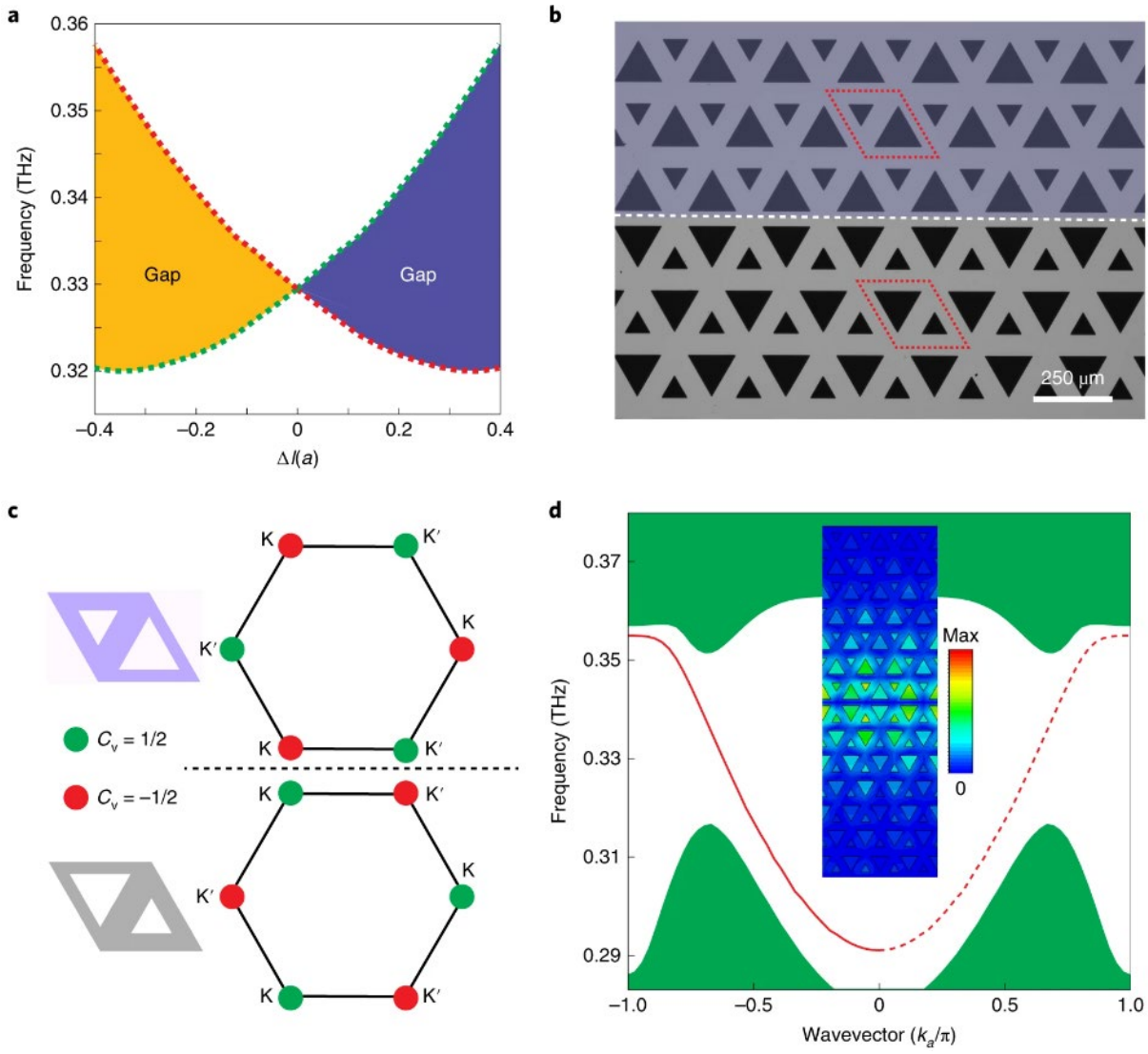

Figure II.10: (a) A phase diagram showing the variation of the gap as a function of Δl in the range $-0.4a$ to $0.4a$. The green and red dotted lines represent LCP and RCP, respectively. (b) An optical image of the fabricated domain wall with opposite Δl on each side. The white dashed line represents the interface between two domains. (c) Topological charge distribution and valley Chern number (C_v) on each side of the domain wall. The dashed line denotes the domain wall. (d) Dispersion of topological kink states at the domain wall. The red line and the green regions represent the edge dispersion and the projected bulk dispersion, respectively. The inset shows the intensity distribution (colour scale) of the magnetic field around the domain wall. The red dashed and solid lines represent the kink states locked to the K and K′ valleys, respectively. k_a denotes the wavevector along the domain wall [34].

Therefore, in short, designing a valley PTI typically begins with a graphene-like photonic crystal, featuring a "Dirac"-like degeneracy at the K (K') point. Breaking inversion symmetry in such structures can lead to a controllable bandgap by differentiating the properties of the constituent elements within the unit cell, typically denoted as A and B sites. This differentiation breaks the inversion symmetry and allows for the emergence of opposite Berry curvature at the K and K' points. Consequently, selective coupling to either K or K' valleys can result in

unidirectional topologically protected edge modes aligned with the direction from Γ to K or Γ to K' [16,26].

1. Our designs include straight and bent waveguides with VPC PTIs featuring triangular holes and zigzag terminations. We have also developed round waveguides with VPC PTIs featuring round holes and bearded terminations.
2. To analyze the degree of topological protection of the considered triangular topological resonator designs made of permuting round and triangular hole geometry with zigzag and bearded terminations, we have conducted 2D simulations using finite element simulations of the electromagnetic field inside the structures. To further refine our designs, we have conducted 3D simulations using COMSOL. The exact three-dimensional membranal devices, specifically for topological resonator designs, have been simulated after direct importation of the GDS (layout) files used for the fabrication.
3. As an example of our perspective topological protection, we have introduced the double cavity resonator design, which can also be used as a lobe to tune passive functions. Our dedication to pushing the boundaries of Terahertz research is evident in our innovative designs and rigorous numerical simulations.

**The entire project is a collaborative effort, and we have named our research project "TOPOTERA". Our collaborators from the PhlAM laboratory at the University of Lille have played a vital role in the theoretical and simulation part of the project. The project's design and simulations were carried out by Gaetan LEVEQUE, a Professor of Universities at the University of Lille - IEMN, and Pascal Szriftgiser, Director of Research CNRS - PhLAM. Alberto Amo, Director of Research CNRS - PhLAM, has also helped us with our theoretical understanding of the project.*

II. 2 Design of VPC unit cells

In our work, topological device chips are prepared on Silicon- on Insulator (SOI) wafers with 90 µm-thick high-resistivity silicon (HR-Si) of resistivity larger than 10 kΩ-cm and relative permittivity 11.7. HR-Si offers a CMOS-compatible platform with low absorption loss and a non-dispersive refractive index. Here, the VPC device layer is asymmetrically placed between the SiO_2 substrate and top air region.

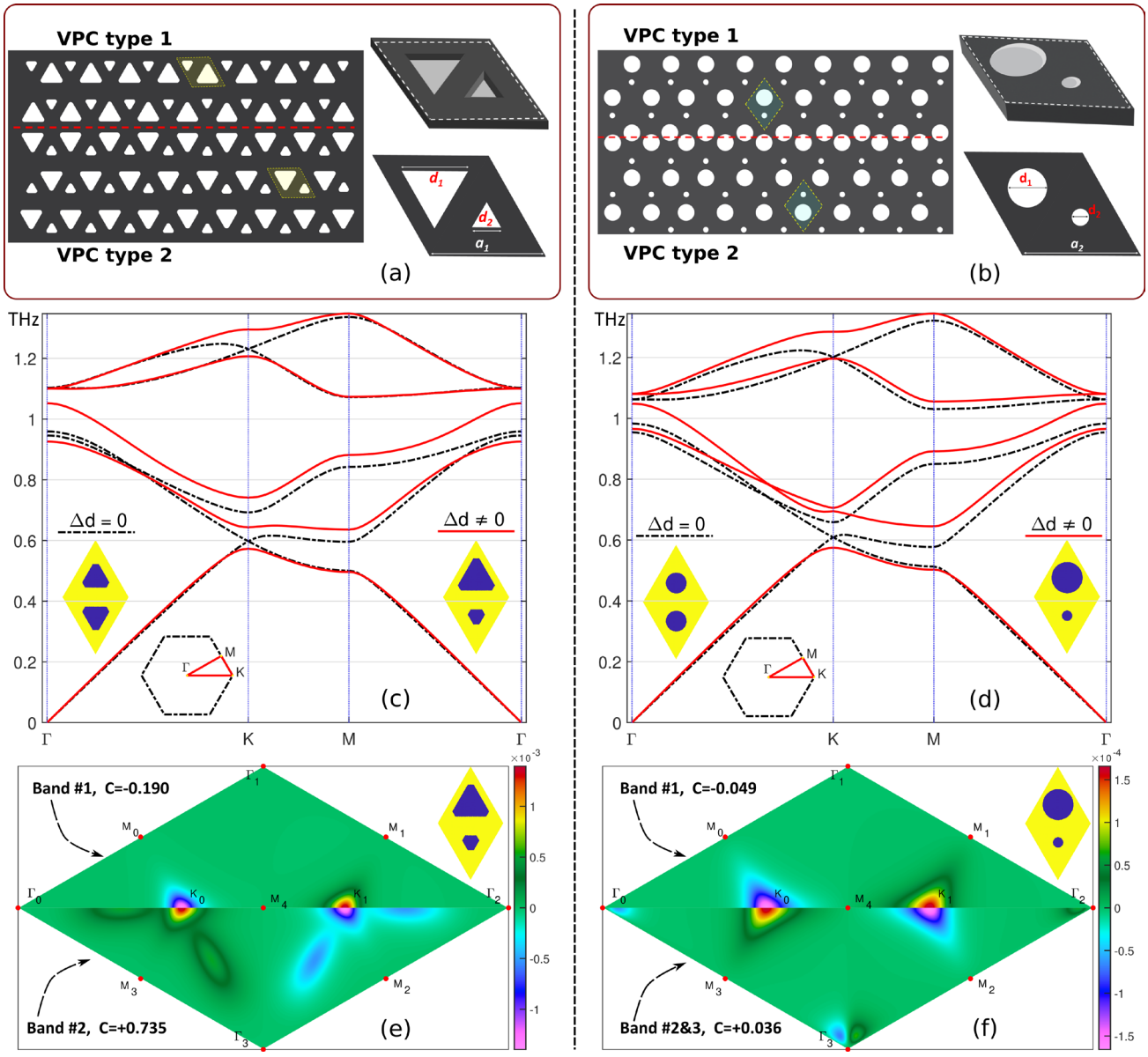

Figure II.11: (a, c, e) on the left: triangular holes structure. (b, d, f) on the right: circular holes structure. (a, b): Schematic representation of the fabricated sample. The yellow-shaded regions show unit cells. Magnified view of the unit cell in 3D before leveling of corners and in 2D after leveling off are presented at right side of the images. See Fig. S6 for images of actual samples. The red dashed lines indicate the zigzag interface. (c, d): Band diagrams with and without inversion symmetry used in bidimensional simulations. (e, f): Berry simulation curvatures (TE polarization) near the K and K′ valleys. In the case of circular holes, band 2 and 3 are degenerated, the Berry curvature calculation must be performed for both of them. Valley Chern number (C) are given for the half-left side (Γ0Γ1Γ2) of the diagram.

Fig. II.11 presents the schematics of two topologically distinct Si-VPC designs, composed of a well-known graphene-like honeycomb lattice with equilateral triangular or circular air holes. Here we assign a zigzag interface (zz) for the triangular hole design and a bearded interface (bd) for the circular holes. For 3D membranal simulations, lattice constants are a_1 = 137 µm

and a_2 = 126 µm (see Table II.2). For 2D simulations, in order to set the first gap at 600 GHz, lattice constant values have been adjusted to respectively a_1~113 µm and a_2~108 µm, see Table II.1

Holes	Period (µm)	d_1 (µm)	d2 (µm)
triangular	113	74	40
circular	108	51	17

Table II.1: Geometrical parameters of the bidimensional photonic crystals.

Holes	Period (µm)	d_1 (µm)	d2 (µm)
triangular	137	89	48
circular	126	54	18

Table II.2: Geometrical parameters of the membranal photonic crystals

Fig. II.11 (a, b) shows the schematics of two topologically distinct Si-VPC designs. Fig. II.11(a) comprises two oppositely facing inverted equilateral triangular holes with a side length of d_1 = 74 µm and d_2 =40 µm (rhombus-shaped shaded region in Fig. II.11(a).

The triangles are leveled off 10 micrometers before the vertex to reduce defects during the deep etching of the device). Similarly, each VPC unit cell in Fig. II.11(b) comprises two circular air holes with a diameter of d_1 = 51 µm and d_2 = 17 µm. For the triangular holed unit cell design, when the triangular holes have equal size d_0= (d_1+d_2)/2 = 0.5 a_1=57µm, the unit cell shows C_6 rotation symmetry that leads to a pair of degenerate Dirac points (at the K_0 and K_1 valleys) in the band as shown in Fig. II.11(c). Upon breaking the C_6 rotation symmetry to C_3 rotation symmetry by setting $d_1 \neq d_2$ (in our case (d_1 = 0.65 a_1 and d_2 = 0.35 a_1), inversion symmetry is broken and leads to a bandgap (0.57 THz < f < 0.64 THz, see red lines in Fig II.11(c)). A similar situation takes place for the VPCs with circular holes shown in Fig. II.11(b, d). In this case the lattice period is a_2 =108 µm, the larger circle diameter d_1 = 51 µm, the smaller circle diameter d_2 = 17 µm and d_0 = (d_1+d_2)/2= 34 µm. Here also band gap opens at the same frequency range when inversion symmetry is broken. It is well established that VPCs exhibit non-zero Berry curvatures localized at the K_0 and K_1 valleys. TE (Transverse Electric) polarization refers to a polarization state where the electric field vector of an electromagnetic wave is perpendicular to the direction of propagation. In the context of valley photonic crystals, TE polarization can be manipulated using the periodic arrangement of dielectric materials to control the propagation of light in specific valley states. Hence, the electric field is parallel to the plane xy of the lattice, and only the z component Hz of the magnetic field is non-zero. To quantify these Berry curvatures (in TE polarization), we employed a plane wave expansion

method implemented in MATLAB. The topological interfaces appear when using to VPC with opposite valley Chern index. The computational analysis confirms the presence of non-zero Berry curvatures around distinct valleys, as depicted in Fig. II.11(e, f). Furthermore, it is noteworthy that within the same band, these Berry curvatures are identical in magnitude but possess opposite signs for the K_0 and K_1 valleys. Consequently, the net integrated Berry curvature associated with any single band is zero. This phenomenon is additionally underpinned by the preservation of time-reversal symmetry within the VPC structure.

II.2.1 Interfacial Topological Designs

Interface terminations are the channels for valley modes that interface between the topologically distinct structures that is with valley chern numbers. Topologically Protected Edge Waves (TPEWs) are not solely confined to specific locations; various guided modes can also propagate in channels formed between any two photonic crystals that exhibit a bandgap around the desired wavelength. Utilizing topological interfaces, which not only possess a bandgap but also feature distinct signs of the valley-Chern index, offers a unique advantage. TPEWs resulting from such interfaces are inherently highly immune to back-scattering within the same valley, thus significantly diminishing inter-valley scattering. This topological protection presents an intriguing opportunity for low reflection out-coupling of TPEWs into the vacuum region. The key to achieving efficient out-coupling lies in terminating the photonic structure in a manner that prevents inter-valley scattering. Predicting the types of terminations that minimize inter-valley scattering involves calculating the field overlap between TPEWs from different valleys. Research indicates that inter-valley field overlap becomes negligible under certain types of perturbations, such as zigzag and bearded perturbations while remaining non-zero for armchair-type perturbations [27-28]. Consequently, it's anticipated that TPEWs encountering terminations along zigzag edges and bearded edges have low probabilities to into a different valley.

1. Triangular holes with zigzag interface	
2. Triangular holes with bearded interface	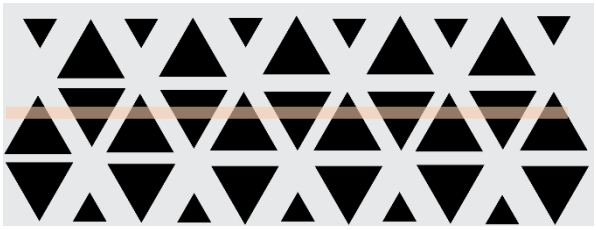
3. Round Holes with bearded interface	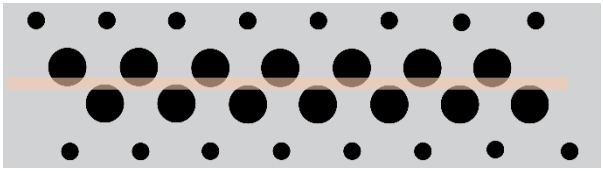
4. Round holes with zigzag interface	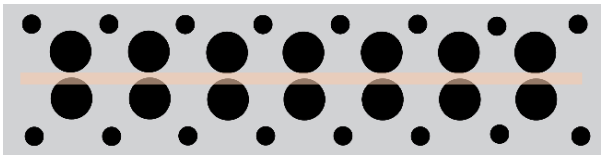

Table II.3: Schematic of the Interfacial terminations used

This underscores the robustness of TPEWs along topologically protected edges. Most existing reports on valley PTIs have explored the geometrical optimization of air holes in VPCs [29], [30], as well as the design of composite interface junctions for air-slot-like VPC waveguides with 60° bends and unchanging bearded interfaces to enable topologically protected propagation of THz waves over a 20% relative bandwidth [31]. There remains a gap in our understanding regarding a comprehensive formula for scaling topological protection utilizing these degrees of freedom. Notably, a study has demonstrated that bearded-stack VPCs with glide-plane symmetry exhibit higher uni-directional coupling efficiency compared to zigzag-stack VPCs with inversion symmetry [32].

While specific applications have been investigated with optimizations of air hole geometry and interfacial topological studies, a broader exploration of a general formula to effectively enhance topological protection for a wide range of futuristic applications remains unexplored.

Moreover, perfect topological protection can be detrimental for some applications such as photonic crystal resonant cavities and add-drop filters.

In these cases, perfect protection results in the absence of any resonant feature, and the controlled breakup of topological protection can be an asset to optimize some functionalities [33]. This significant knowledge gap necessitates further investigation and presents an opportunity for impactful scientific contributions. In our work, we also show that the partial breakup of topological protection can be an asset for the design of on-chip passive functionalities in section II.2.3. To experimentally verify the scalability of topological protection, we demonstrate the performance of terahertz (THz) topological ring resonators and THz double cavity resonators designed for operation in the 600 GHz frequency region in section II.2.3 and II.2.4. This work showcases how the scaling of topological protection can be achieved by utilizing a combination of air hole geometry and interfacial degrees of freedom, providing functional tuning of devices at the chip level. The combination of air hole geometries and interfacial ruminations we used are shown in Table II.3.

II.2.2 THz topological Waveguides

In order to study the valley modes in the 600 GHz range, we conducted simulations of straight and bent waveguides to assess the effect of sharp edges on scattering. Our waveguides were designed to be topologically protected, and were 5 mm in length. We observed that valley kink modes were able to propagate through the zigzag of VPC type A and VPC type B, as shown in Figure II.12(a). Additionally, we simulated the electric field magnitude through the straight waveguide at 600 GHz, as illustrated in Figure II.12(a). We also simulated electric field confinement in the bent waveguide at 600 GHz, as depicted in Figure II.12(b). Our results indicate that the valley modes propagated with robustness and resistance to scattering, as evidenced by the S21 transmission simulation that yielded similar levels around -5dB, as shown in Figure II.13.

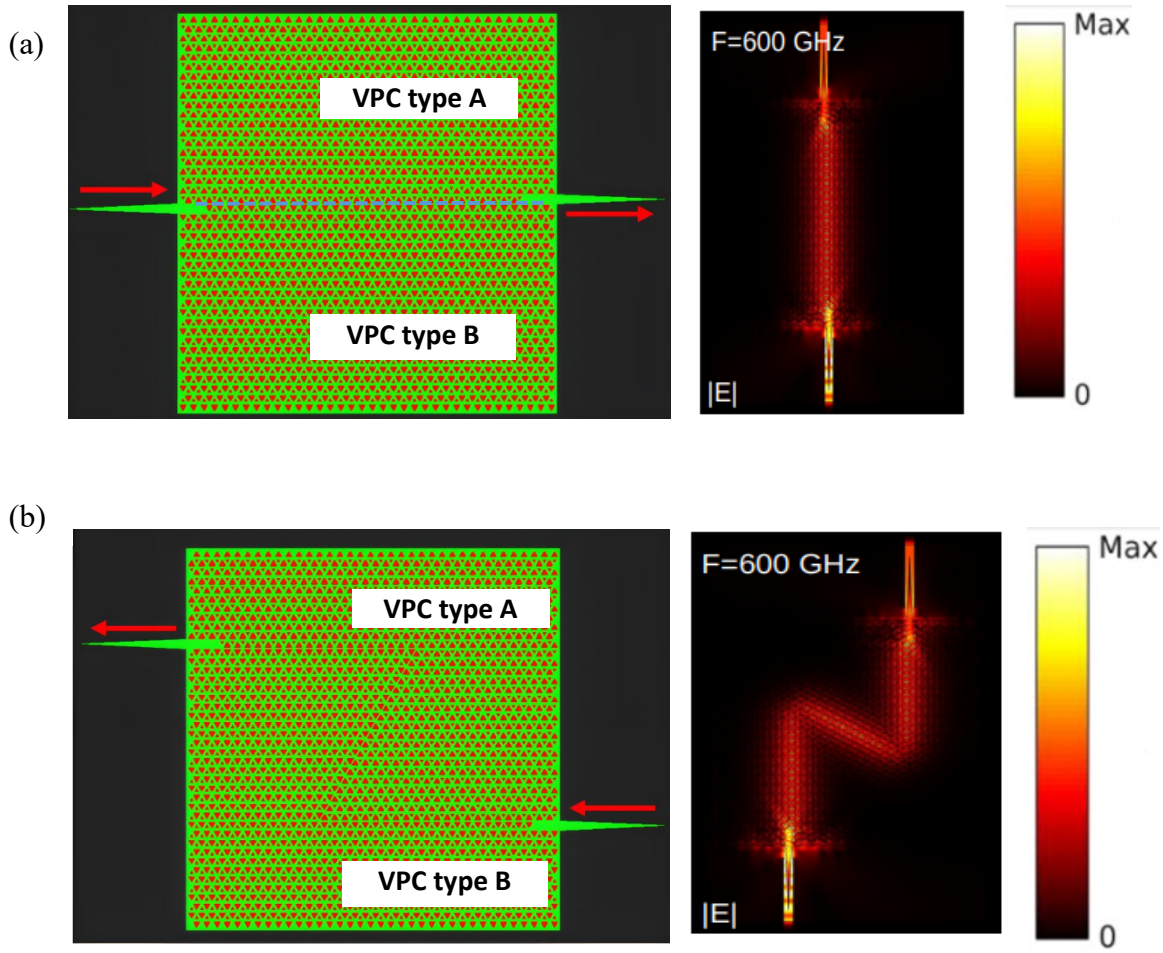

Figure II.12(a): Schematic of the bent waveguide designed using triangular holes and magnitude of the electric field confined at 600 GHz(b) Schematic of the bent waveguide designed using triangular holes and magnitude of the electric field confined at 600 GHz

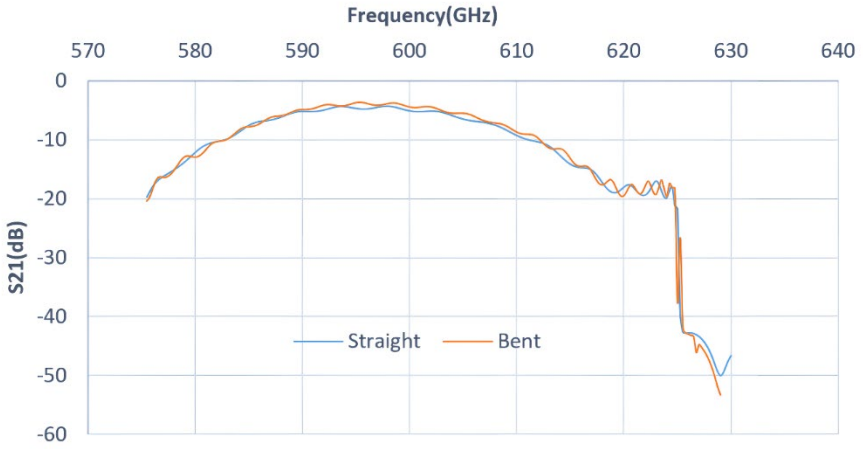

Figure II.13. Simulation for transmission through bent and straight waveguide.

II.2.3 THz topological resonator

Numerical Simulations

To analyze the degree of topological protection of the considered designs we perform finite element simulations of the electromagnetic field inside the structures. All simulations have been done using the software COMSOL Multiphysics. We will see that different hole geometries and types of topological edges can show variations in the quality of their topological protection. Indeed, an edge mode can experience conversion into the mode with opposite pseudo-spin at different locations all along a device, through back-scattering at splitters and abrupt bifurcations, or transmission along topologically forbidden directions across splitters. THz topological ring resonators, addressed at their tip though a linear topological waveguide, allows enhancing the effect of small ruptures of topological protection through the recirculation of the mode inside the cavity, which manifest themselves as sharp minima in their transmission spectra. On the contrary, if topological protection is perfect, the electromagnetic wave cannot be reflected towards the source, the reflection coefficient is then zero and the transmission coefficient must be unity for any frequency at which the edge-mode exists.

II.2.3.1 Bidimensional Simulations

We first start by investigating bidimensional topological circuits, based on either circular or triangular air holes in a silicon matrix (lossless and with dielectric constant ε_r=11.7), where light is guided along either zigzag or bearded interfaces. The triangle's corners have been cut off at a length of 10 µm, to ease the fabrication process as shown in Fig. II.14(a). In all configurations, the interface is realized between large circular or triangular holes as shown for example in Fig.~ II.10 for the 3D case. Further details about the typical numerical setup are given on Fig. II.14, illustrating the case of a THz topological triangular ring resonator with a zigzag (underlined by cyan dashed lines) and triangular holes corresponding the Fig. II.14 .

The simulation domain is surrounded by Perfectly Matched Layers that absorb outgoing waves to simulate an infinite system. The main elements of the simulations are indicated on Fig. II.14. The source is a rotating dipole located at the red star. The transmission (T) and reflection (R) power coefficients are evaluated by integrating the Poynting vector's y-component through their corresponding propagation direction (dashed line in Fig. II.12) and normalizing to the power of the edge mode propagating along a straight edge excited by the same source.

We consider TE polarization: the electric field is parallel to the plane *xy* of the lattice, and only the *z* component *Hz* of the magnetic field is non-zero. All THz topological ring resonators in this section have a side length equal to 28 lattice periods.

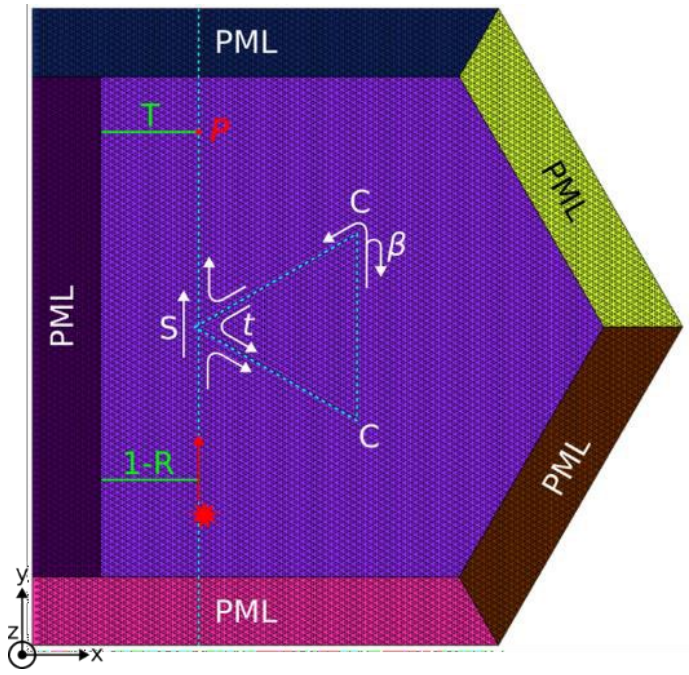

Figure. II.14: Numerical setup for finite elements simulations. PML indicate the domains or Perfectly Matched Layers; transmission (T) and reflexion (R) are computed along the corresponding the green lines. The star indicates the location of the source. Parameters t and β indicate respectively the inter-cavity transmission coefficient at the splitter S, and the back-scattering coefficient at a corner C, both in amplitude of the edge-mode.

In order to match the frequency position and width of the band gap of the device, the geometrical parameters had to be slightly adjusted in the bidimensional geometry. This does not change the general observations and conclusions of the corresponding simulations. We have simulated the dispersion diagrams, transmission coefficient *T* and associated group delay τg ($\tau g = -d\varphi/d\omega$, evaluated from the phase φ of the component Hz of the magnetic field at point *P* on Fig. II.15 (a)) for the four possible combinations between hole shapes (triangular or circular) and interface types (zigzag or bearded). Fig. II.15 (b-g) shows the corresponding dispersion diagrams of the edge modes for circular (b), triangular (e) holes, where the bearded (bd) edge mode is plotted in red, and the zigzag (zz) edge mode is in blue, while the blue-green areas indicate the bulk modes. Transmission coefficient and group delay are shown for (c), triangular holes and zigzag edge, (d), triangular holes and bearded edges, (f), circular holes and zigzag edge, and (g), circular holes and bearded edge. The geometrical parameters of the lattices are given on Table II.

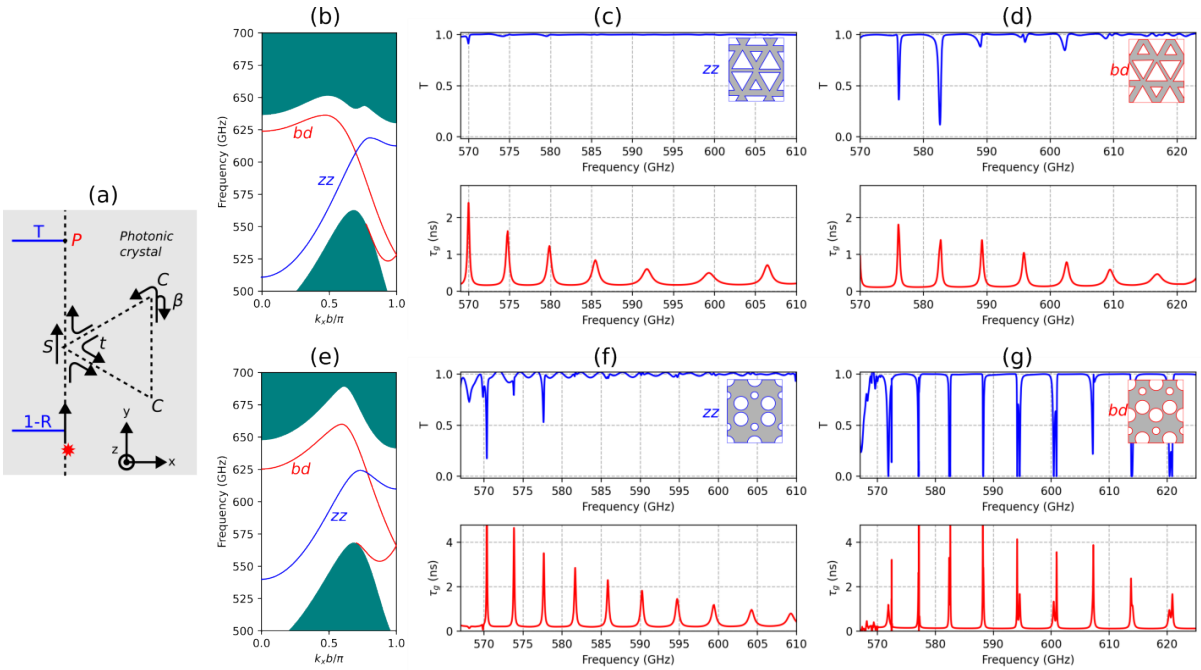

Figure. II.15: (a) Diagram indicating the main elements of the simulation. Corners are labelled C, the splitter S. Parameters t and β indicate respectively the inter-cavity transmission coefficient at the splitter S, and the back-scattering coefficient at a corner C, both in amplitude of the edge-mode. (b-g) Dispersion diagrams, transmission spectra T (top) and group delay τ_g (bottom) computed through resonators in photonics crystals with triangular (b,c,d) or circular (e,f,g) holes, for bearded (c,f) or zigzag (d,g) interfaces. On the dispersion diagrams (b,e), blue-green areas indicate the bulk modes of the lattice, the blue (resp. red) curve is for the bearded (resp. zigzag) interface.

Regardless the type of hole, shapes of the transmission spectra clearly evidence that zigzag edges Fig. II.15 (c,f) better preserve the topological protection than bearded edges Fig. II.15 (d,g). That can be seen from the number of observable narrow resonances in the computed spectra, which is larger for bearded than for zigzag interfaces, both for triangular and circular holes. Recall that the transmission through the triangular resonant ring should not show any resonant feature in case of perfect topological protection. The transmission resonance peaks visible in particular in Fig. II.15 (d), (f), (g) evidence deviations from perfect topological protection. For zigzag edges (Fig. II.15 (c), (f)), transmission minima occur only for the lowest frequencies within the band-gap, and never reach zero. For triangular holes (Fig. II.15 (c)), the transmission reaches its lowest value of 91% at F=570 GHz, and stays very close to 1 otherwise. Resonances of the structure are however clearly visible in the frequency dependence of the group delay, which presents a regular pattern of Lorentzian-type resonances throughout the whole frequency window, with lowest amplitude close to 600 GHz. Indeed, despite not

being redirected toward the source, the edge mode is reinjected at the splitter after each tour (coefficient *t* on Fig. II.15 (a)) inside the triangular resonator: this mode spends more time and is then enhanced inside the cavity, which correlates with the enhanced group delay. For circular holes (Fig. II.15 (f)), resonances appear again in the low-frequency part of the band gap (F<580 GHz) and reach 18% at F=570 GHz. The small oscillation in *T* is related to a small reflection on the PMLs, which leads to a weak Fabry-Perot effect between PMLs at the top and the bottom of the simulation domain. Again, the group delay is periodically enhanced but decreases in amplitude with frequency.

For the bearded edge, Fig. II.15 (d), more transmission minima are visible, however, the resonances are noticeable only for frequencies lower than 585 GHz, where a minimum of 12% is reached at F=582.6 GHz. The behavior of the group delay is similar to Fig. II.15 (c), but the minimum is reached close to 620 GHz. Finally, the combination of bearded edge with circular holes, Fig. II.15 (g), appears to be the one where the loss of topological protection is the largest, as a regular series of sharp resonances reaching 0 (except for F=606 GHz) is obtained in the whole range of simulated frequencies. Most of the resonances appear as split-resonances, which relate to the interference between the edge modes traveling in the direct and indirect orientations along the triangular resonator. As shown in [33], those back-reflections are mostly due to reflections of the edge modes at the corners of the cavity, with weaker contributions from the splitter. The largest double-peak splitting is obtained for resonances close to F=600 GHz and F=594 GHz, with separations of ΔF=0.43 GHz and ΔF=0.48 GHz respectively. From the value of splitting and following the method described in [33], we can estimate the back reflection at each corner of the triangular resonator to be $|\beta|^2$=2.3% in power. It can be mentioned that the group delay is always positive, and splits in double peaks as for the transmission coefficient. Overall, the group delay is larger than 2 ns at resonances, which is about twice as large as the value obtained for the bearded edge with triangular holes. The group velocity v_g of the edge mode can be evaluated from the dispersion curve, which leads to a value of $v_g=0.2c_0$ for F=597 GHz, where c_0 is the velocity of light in a vacuum. Owing to the size of the cavity, it appears that the edge mode takes about 0.2 ns to make one tour of the cavity, which indicates that it travels between 5 and 20 tours at resonances before being out-coupled. Fig. II.17 shows typical field distributions for a highly transmitted frequency (a) and at a resonant minimum (b).

The main conclusions from these simulations are: (i) zigzag interfaces are more topologically protected than bearded interfaces (ii) for both types of edges, circular holes show more and deeper transmission resonances than triangular holes.

II.2.3.2 3D Simulations

The exact three-dimension of the devices have been simulated in Comsol after direct importation of the gds (layout) files used for the fabrication,typical numerical setup shown in Fig. II.16.

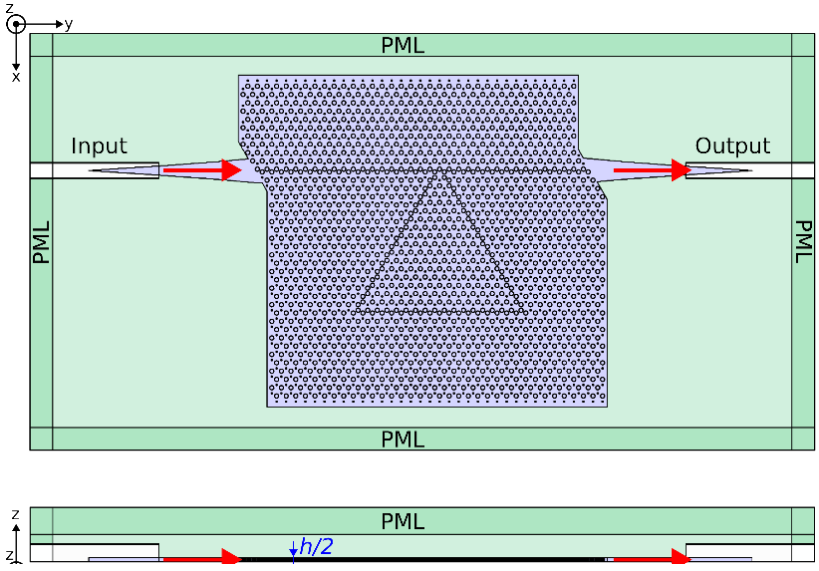

Figure. II.16: Numerical setup for finite elements simulations of the full membranal device. The thickness of the membrane is h=90µm, the dielectric constant of silicon is 11.7.

The device is fed by a waveguide whose dimensions are the same as in the experiments, ie 500-750 GHz metallic hollow- core waveguide. The transmission is computed through an output waveguide with identical characteristics. Only half of the membrane is modelled, and a symmetry plane is applied on the bottom surface (parallel to *xy*) of the simulation domain to compute symmetric modes: the magnetic field is perpendicular to that plane. In all the following simulations, a small oscillation is observed in the transmission spectra, related to reflections of the edge modes on the limits of the photonic crystal. The geometrical parameters of the lattice are given in Table II. 2. In this section, the side length of the THz topological ring resonators is equal to 16 lattice periods.

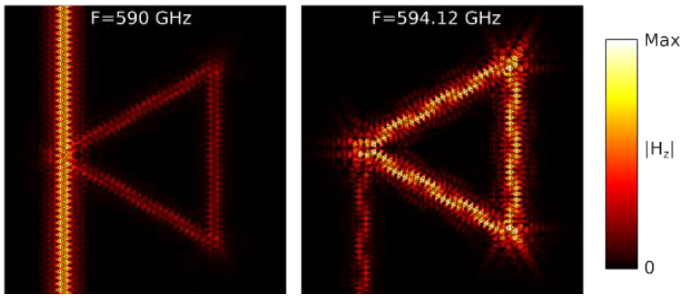

Figure. II.17 Topological ring resonator: magnetic field distributions corresponding to the spectra presented in fig. II.15, specifically for the panel (f) correspond to circular holes with zigzag edges at 590 GHz (left), at 594.12GHz, away from any resonance.

Fig. II.18 shows the numerical results for the devices with single- cavities resonators. Only two types of topological interfaces have been simulated which, within the four geometries discussed above, should correspond, to the highest degree of topological protection (triangular holes and zigzag interface, Fig. II.18 (a)) and the lowest protection (circular holes and bearded interface, Fig. II.18 (b)). In each case, band diagrams picturing the corresponding dispersion curve have been plotted, where the grey area represents the light cone, and the green surface indicates the bidimensional continuum of the lattice bulk modes. Both bidimensional (see Fig. II.15) and 3D-simulated edge modes have similar dispersion relations (except for the presence of the light cone). For the purpose of experimental verification, we have specifically focused on fabricating these two types of designs that represent high and low levels of topological protection. These selected designs serve as examples to showcase the range of possibilities and demonstrate the influence of topological protection on device performance.

As for the bidimensional case, the transmission curve for triangular holes and zigzag interface, Fig. II.18 (a), does not show noticeable resonance features, which implies that the amount of backscattering related to the loss of topological protection is negligible. However, cavity resonances are still observable in the group delay, which presents, as for the bidimensional case, a series of regularly spaced positive maxima, with amplitude reaching a minimum close to F=595 GHz. Sharp and deep transmission resonances are obtained for circular holes and bearded interface, Fig. II.18 (b), with four clear double peaks at F=576, 592, and 600 GHz. The frequency interval of the two split- resonances at 592 and 600 GHz are respectively $\Delta F=0.49$ and 0.51 GHz. Following the same procedure

as for the bidimensional case, we estimate a backscattering coefficient at the corners to be 1.7% in power. The most striking difference with Fig. II.15 is the shape of the group delay, which takes negative values (down to –5 ns) at each transmission minima of the two mentioned split-resonances, where it always keeps positive values in the bi-dimensional simulations. The reason is the shorter size of the lattice in the membrane (3D) system, related to numerical and fabrication constraints: at resonances, the field is enhanced inside the cavity and leaks in the air along the edges of the device. This introduces an anomalous evolution of the phase which results in negative group delays.

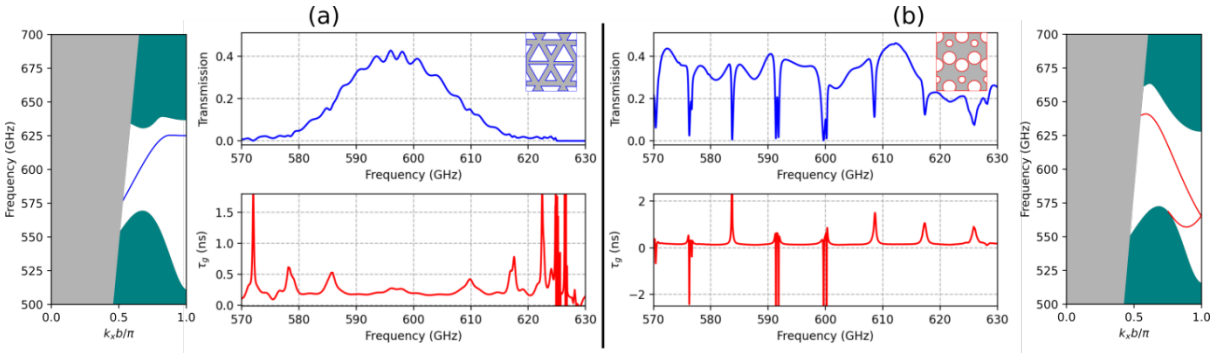

Figure. II.18: Band diagrams, transmission spectra (top) and group delay (bottom) computed through the full 3D devices with single-cavity resonators, for circular holes and zig-zag interface (a), and triangular holes and bearded interface (b). In each case, the band diagram of the interface is plotted, with the light cone in grey and lattice bulk modes in blue-green.

II.2.4 THz Double Cavity Resonator

Fig. II.19 shows the 3D simulated transmission spectrum and group delay of a double-cavity resonator, where two triangular cavities are united along a common zigzag edge, using a photonic crystal made of triangular holes, see Fig. II.15(a). This simulation is to be compared to the single cavity case on case with the same type of holes and interface displayed in Fig. II.18(a).

Two transmission features are visible on the double-cavity spectrum, Fig. 19(b): a first shallow minimum close to F=587 GHz, and a very sharp split-resonance at 597.3 GHz, whose detailed profile is seen for a reduced frequency window on Fig. II.19 (c). The frequency interval between both transmission minima is ΔF'=60 MHz, which is lower by a factor of about 8 than the value

obtained for the split resonances of the single cavities with circular holes and bearded edge. In order to interpret this resonance, we first notice that it cannot be related to back-scattering at the two corners (C1 and C2), as otherwise double peaks would be observed in the single cavity simulations. For this reason, it must be attributed to backscattering occurring at both splitters (S1 and S2), for example along the edge S1S2.

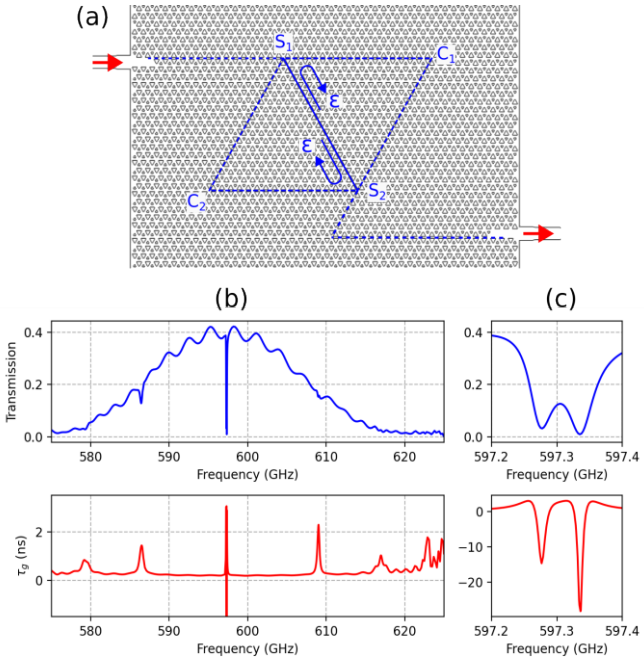

Figure. II.19: (a) Top view of the device with double-cavity resonator. Corners are labelled C1 and C2, splitters S1 and S2. The parameter ε is the reflection coefficient on the splitter, for an edge mode propagating along the common edge S1S2 of the double cavity. (b) Transmission spectra (top) and group delay (bottom) as a function of the frequency; (c) same as (b) for a frequency range closer to the split resonance at 597 GHz.

Using the same method in [33], we can estimate the amplitude of the corresponding backscattering coefficient ε to be $|\varepsilon|^2$=0.014% in power. As for the single cavity, the fact that the group velocity reaches negative values (down to –28 ns) is attributed to the leakage in air at the edge of the device. For comparison, the simulation of the bi-dimensional case is given in Fig. II.20.

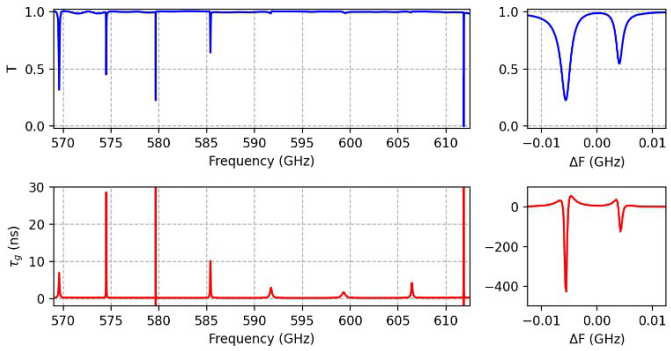

Figure. II.20: Transmission and group delay for the bidimensional double-cavity resonator. For the zoom on the split resonance at 579 GHz (right panels), ΔF=F- F0, and F0= 579.6825 GHz.

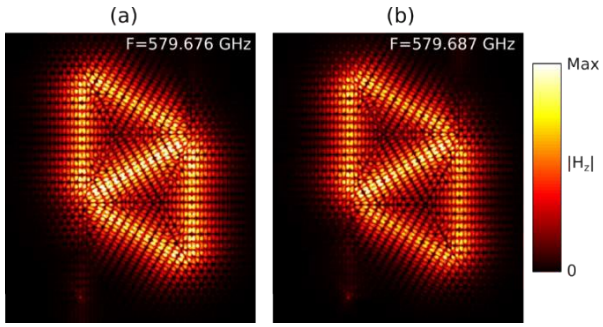

Figure. II.21: Magnetic field distributions corresponding to the split resonance shown in Fig. II.19.

The Fig.II.21 shows the magnetic field distributions corresponding to the split resonance shown in Fig. II.19. In these simulations, both split-resonances show negative group delay. The origin is the same as above: the peaks are very narrow and the enhancement of the magnetic field inside the cavity is very large. As a consequence, the cavity mode leaks in the PMLs. For a sufficiently large simulation domain (but which could not be reached numerically), the transmission should become zero, and the group delay is positive.

Conclusion of this Chapter

Chapter II, titled "THz Topological Devices: Design and Numerical Studies," presents an in-depth exploration of the emergence of topological properties of light and our detailed design and numerical simulations of our THz passive functionalities. Our designs, including normal waveguides to THz double cavity resonators, all based on Valley PTI designs specifically tailored for the 600 GHz central frequency region. The simulations conducted in this chapter have yielded highly promising results, indicating the potential efficacy of our proposed designs.

References

[1] J. Joannopoulos, S. G. Johnson, J. N. Winn, and D. M. Robert, Photonic Crystals: Molding the Flow of Light. Princeton University Press, 2008.
[2] T. Ozawa et al., “Topological photonics,” Rev. Mod. Phys., vol. 91, no. 1, p. 015006, Mar. 2019, doi: 10.1103/RevModPhys.91.015006.
[3] D. J. Thouless, M. Kohmoto, M. P. Nightingale, and M. den Nijs, “Quantized Hall Conductance in a Two-Dimensional Periodic Potential,” Phys. Rev. Lett., vol. 49, no. 6, pp. 405–408, Aug. 1982, doi: 10.1103/PhysRevLett.49.405.
[4] F. D. M. Haldane, “Model for a Quantum Hall Effect without Landau Levels: Condensed-Matter Realization of the ‘Parity Anomaly,’” Phys. Rev. Lett., vol. 61, no. 18, pp. 2015–2018, Oct. 1988, doi: 10.1103/PhysRevLett.61.2015.
[5] M. Z. Hasan and C. L. Kane, “Colloquium: Topological insulators,” Rev. Mod. Phys., vol. 82, no. 4, pp. 3045–3067, Nov. 2010, doi: 10.1103/RevModPhys.82.3045.
[6] B. Simon, “Holonomy, the Quantum Adiabatic Theorem, and Berry’s Phase,” Phys. Rev. Lett., vol. 51, no. 24, pp. 2167–2170, Dec. 1983, doi: 10.1103/PhysRevLett.51.2167.
[7] M. Nakahara, Geometry, Topology and Physics, 2nd Edition. Bristol ; Philadelphia: CRC Press, 2003.
[8] A. Bansil, H. Lin, and T. Das, “Colloquium : Topological band theory,” Rev. Mod. Phys., vol. 88, no. 2, p. 021004, Jun. 2016
[9] X.-L. Qi and S.-C. Zhang, “Topological insulators and superconductors,” Rev. Mod. Phys., vol. 83, no. 4, pp. 1057–1110, Oct. 2011, doi: 10.1103/RevModPhys.83.1057.
[10] H.-X. Wang, G.-Y. Guo, and J.-H. Jiang, “Band topology in classical waves: Wilson-loop approach to topological numbers and fragile topology,” New J. Phys., vol. 21, no. 9, p. 093029, Sep. 2019, doi: 10.1088/1367-2630/ab3f71.
[11] F. Wilczek and A. Shapere, Geometric Phases in Physics, vol. 5. World Scientific, 1989.
[12] S. Pancharatnam, “Generalized theory of interference, and its applications,” Proc. Indian Acad. Sci., vol. 44, no. 5, pp. 247–262, Nov. 1956, doi: 10.1007/BF03046050.
[13] M. V. Berry, “Quantal phase factors accompanying adiabatic changes,” Proc. Math. Phys. Eng. Sci., vol. 392, no. 1802, pp. 45–57, Mar. 1984, doi: 10.1098/rspa.1984.0023
[14] J. von Bergmann and H. von Bergmann, “Foucault pendulum through basic geometry,” Am. J. Phys., vol. 75, no. 10, pp. 888–892, Sep. 2007, doi: 10.1119/1.2757623.
[15] R. Y. Chiao and Y.-S. Wu, “Manifestations of Berry’s Topological Phase for the Photon,” Phys. Rev. Lett., vol. 57, no. 8, pp. 933–936, Aug. 1986, doi: 10.1103/PhysRevLett.57.933.

[16] D. Bisharat, R. Davis, Y. Zhou, P. Bandaru and D. Sievenpiper, "Photonic Topological Insulators: A Beginner's Introduction [Electromagnetic Perspectives]," in IEEE Antennas and Propagation Magazine, vol. 63, no. 3, pp. 112-124, June 2021, doi: 10.1109/MAP.2021.3069276.
[17] E. Cohen, H. Larocque, F. Bouchard, F. Nejadsattari, Y. Gefen, and E. Karimi, "Geometric phase from Aharonov–Bohm to Pancharatnam–Berry and beyond," Nat. Rev. Phys., vol. 1, no. 7, Art. no. 7, Jul. 2019, doi:10.1038/s42254-019-0071-1.
[18]. Lu, L., Joannopoulos, J. & Soljačić, M. Topological photonics. Nature Photon 8, 821–829 (2014). https://doi.org/10.1038/nphoton.2014.248
[19] Y. Hatsugai, "Chern number and edge states in the integer quantum Hall effect," Phys. Rev. Lett., vol. 71, no. 22, pp. 3697–3700, Nov. 1993, doi: 10.1103/PhysRevLett.71.3697.
[20] A. Mekis, J. C. Chen, I. Kurland, S. Fan, P. R. Villeneuve, and J. D. Joannopoulos, "High Transmission through Sharp Bends in Photonic Crystal Waveguides," Phys. Rev. Lett., vol. 77, no. 18, pp. 3787–3790, Oct. 1996, doi:10.1103/PhysRevLett.77.3787.
[21] Y. D. Chong, X.-G. Wen, and M. Soljačić, "Effective theory of quadratic degeneracies," Phys. Rev. B, vol. 77, no. 23, Jun. 2008, doi: 10.1103/PhysRevB.77.235125.
[22] L. Xu, H.-X. Wang, Y.-D. Xu, H.-Y. Chen, and J.-H. Jiang, "Accidental degeneracy in photonic bands and topological phase transitions in two-dimensional core-shell dielectric photonic crystals," Opt. Express, OE, vol. 24, no. 16, pp. 18059–18071, Aug. 2016, doi: 10.1364/OE.24.018059.
[23] Z. Wang, Y. D. Chong, J. D. Joannopoulos, and M. Soljačić, "Reflection-Free One-Way Edge Modes in a Gyromagnetic Photonic Crystal," Phys. Rev. Lett., vol. 100, no. 1, p. 013905, Jan. 2008, doi:10.1103/PhysRevLett.100.013905.
[24] Z. Wang, Y. Chong, J. D. Joannopoulos, and M. Soljačić, "Observation of unidirectional backscattering-immune topological electromagnetic states," Nature, vol. 461, no. 7265, pp. 772–775, Oct. 2009, doi:10.1038/nature08293
[25] C. Wang, H. Zhang, H. Yuan, J. Zhong, and C. Lu, "Universal numerical calculation method for the Berry curvature and Chern numbers of typical topological photonic crystals," Front. Optoelectron., Jan. 2020, doi:10.1007/s12200-019-0963-9.
[26] Liu, J. W., Shi, F. L., He, X. T., Tang, G. J., Chen, W. J., Chen, X. D., & Dong, J. W. (2021). Valley photonic crystals. Advances in Physics: X, 6(1). https://doi.org/10.1080/23746149.2021.1905546
[27]. Ma, T., & Shvets, G. (2016). All-Si valley-Hall photonic topological insulator. New Journal of Physics, 18(2), 025012.
[28] He, X. T., Liang, E. T., Yuan, J. J., Qiu, H. Y., Chen, X. D., Zhao, F. L., & Dong, J. W. (2019). A silicon-on-insulator slab for topological valley transport. Nature communications, 10(1), 872.
[29] K. M. Devi, S. Jana, and D. R. Chowdhury, "Topological edge states in an all-dielectric terahertz photonic crystal," Opt. Mater. Express, OME, vol. 11, no. 8, pp. 2445–2458, Aug. 2021, doi: 10.1364/OME.427069.
[30] S. Jana, K. Monika Devi, and D. Roy Chowdhury, "Effect of asymmetry on terahertz transmissions in topological photonic crystals comprising of dielectric rod structures," Optics Communications, vol. 505, p. 127589, Feb. 2022, doi: 10.1016/j.optcom.2021.127589.
[31] Y. J. Tan, W. Wang, A. Kumar, and R. Singh, "Interfacial topological photonics: broadband silicon waveguides for THz 6G communication and beyond," Opt. Express, vol. 30, no. 18, p. 33035, Aug. 2022, doi: 10.1364/OE.468010.
[32] W.-S. Ruan, X.-T. He, F.-L. Zhao, and J.-W. Dong, "Analysis of Unidirectional Coupling in Topological Valley Photonic Crystal Waveguides," Journal of Lightwave Technology, vol. 39, no. 4, pp. 889–895, Feb. 2021, doi: 10.1109/JLT.2020.3024696.
[33] G. Lévêque, Y. Pennec, P. Szriftgiser, A. Amo, and A. Martínez, "Scattering-matrix approach for a quantitative evaluation of the topological protection in valley photonic crystals," 2023, doi: 10.48550/ARXIV.2301.10565
[34] Yang, Y., Yamagami, Y., Yu, X. et al. Terahertz topological photonics for on-chip communication. Nat. Photonics 14, 446–451 (2020)

Chapter III:

Silicon Processing and Fabrication of THz topological Devices

The concept and design of various valley photonic crystals-based THz waveguides and resonators, rooted in the principles of topological phases of light, has been introduced and expounded upon in Chapters I and II. This chapter provides a detailed view of two fabrication runs, namely Topo Run 1 and Topo Run 2, detailing the creation of devices and their inline characterization. TopoRun 1- refers to or is named after the first fabrication run. We used a 4-inch SOI wafer so that many devices could be fabricated in a run. Furthermore, the first run aimed to determine whether the topological waveguides are robust in the higher frequency region. (600 GHz region). The fabrication of these devices involves the use of photolithography followed by deep reactive ion etching (DRIE). Although not within the scope of this thesis, a brief description of the DRIE etching technique is provided in a few paragraphs. Notably, the fabrication process benefits from the collaboration and support of the V-micro company and NAM6 group at IEMN. The waveguides and cavities fabrication process consists of two etching steps of a high resistivity SOI (Silicon on insulator) wafer. The SOI wafer is composed of 90 µm of HR-Si ($\rho > 10k\Omega.cm$) active layer bonded on a 400 µm thick low resistivity silicon substrate. SOI fabrication includes a 2 µm layer of SiO_2 grown by thermal oxidation between the two layers. Before jumping into the fabrication process on the SOI wafer, we did a systemic study how a Silicon wafer is created in its form for fabrication.

III.1 Study on Silicon Wafers

Silicon has long been the dominant semiconductor material for microelectronic circuits, owing to its ability to be produced in a highly pure mono-crystalline form. This crystalline structure facilitates targeted doping with foreign materials, enabling the modulation of electrical conductivity across approximately six orders of magnitude. A notable advantage of silicon, compared to other semiconductor materials like germanium or gallium arsenide, lies in its capacity to generate a chemically stable electrical insulator with a high breakdown field strength through selective thermal oxidation to SiO_2 [1]. Ranked as the seventh most abundant element in the entire universe and the second most common element on Earth, silicon is pervasive in various materials such as beach sand, quartz, flint, and agate [1]. Beyond its role in microelectronics, silicon serves as a major component in construction materials like brick, cement, and glass. Its prevalence extends to the electronic and technology sector, where it holds the top position as the most common semiconductor [2].

Silicon wafers, essential components in integrated circuits, exhibit diverse shapes and sizes depending on their intended use. These polished, mirror-like flat disks play a ubiquitous role in practically every electronic device [2]. Manufacturing method Czochralski pulling technique has been conventionally employed, with more recent methods like the Float Zone gaining popularity due to fewer defects and superior purity [5]. The widespread use of silicon wafers in chip and microchip production underscores their importance in electronic devices. Once extracted from sand, silicon undergoes a purification process before use. The initial step involves heating it until it melts into a high-purity liquid, typically exceeding 99.9999999% purity, with no defects [6]. The liquid is then allowed to solidify into a silicon rod or ingot, using fabrication methods like the Floating Zone or Czochralski process. In the Czochralski method, a small piece of solid silicon is placed in molten silicon and gradually pulled in rotation as the liquid transforms into a cylindrical ingot. Subsequently, the ingot's pyramidal ends are removed before it completely cools. Diamond saw blades are then employed to slice the ingot into thin wafers of consistent thickness, determined by the ingot's diameter [8]. The weight distribution during fabrication is crucial, as inappropriate weight placement may render the wafer susceptible to breakage under relatively low pressure. Processed wafers undergo polishing using machines and abrasive chemicals to achieve a flawlessly smooth surface, facilitating the printing of circuit layouts with ease [8].

III.1.1 Transforming Quartz into High Purity Silicon

Silicon originates from the fiery depths of massive stars, where it forms through fusion at temperatures exceeding 10^9 Kelvin, emerging from oxygen-rich cores. These elements are ejected into the cosmos during the dramatic finale of a star's life—supernova explosions. Despite the universe being predominantly composed of hydrogen and helium, silicon constitutes less than 0.1% of the total mass. In our solar system, shaped by the remnants of past stellar explosions, silicon has been notably enriched, particularly in the inner planets.

These planets, situated closer to the central sun, have lost many volatile elements over time. Earth, our home, boasts a silicon content of around 17%, ranking as the third most abundant element after iron and oxygen, closely trailed by magnesium. Within the iron-based core of our planet, silicon claims the second spot in abundance, making up approximately 7% by mass. The Earth's crust, approximately 40 km thick, contains about 28% silicon in various forms, including silicate minerals and quartz (SiO2) [9].

Additionally, silica (Si(OH)4), the second most common element after oxygen dissolved in the oceans, contributes to this abundance. While pure, elemental silicon is virtually non-existent, its prevalence and distribution play a crucial role in understanding the intricate tapestry of the universe

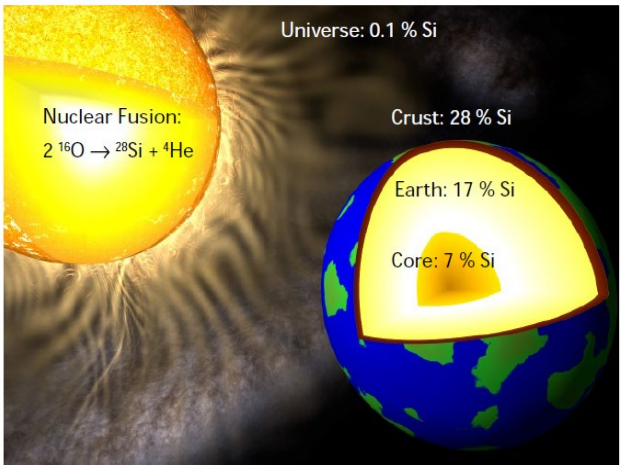

Figure III.1: The Generation of Silicon within Massive Stars and its occurrence in the entire universe and earth.

III.1.2 Synthesis and Application of Metallurgical-Grade Silicon

In the manufacturing process of elemental silicon, quartz sand (SiO2) undergoes reduction within smelting reduction kilns (refer to Fig. III.2) at temperatures approximating 2000°C, facilitated by carbon, resulting in the production of metallurgical-grade silicon (metallurgical silicon) possessing a purity range of approximately 98-99%. The utilization of pristine raw materials and electrodes enhances the purity level significantly. The predominant share of global production, totalling around 7 million tonnes in 2014, is employed as a crucial alloy component in both steel and aluminium production while also serving as a primary raw material for the synthesis of silicones. Approximately 2% of the raw silicon is used for the production of hyper-pure silicon, a process detailed in the subsequent section. Of this refined silicon, approximately 90% is allocated to the manufacturing of silicon solar cells. An annual quantity of around 100 tonnes is ultimately dedicated to the production of silicon wafers for the semiconductor sector, a thematic focus of the present section.

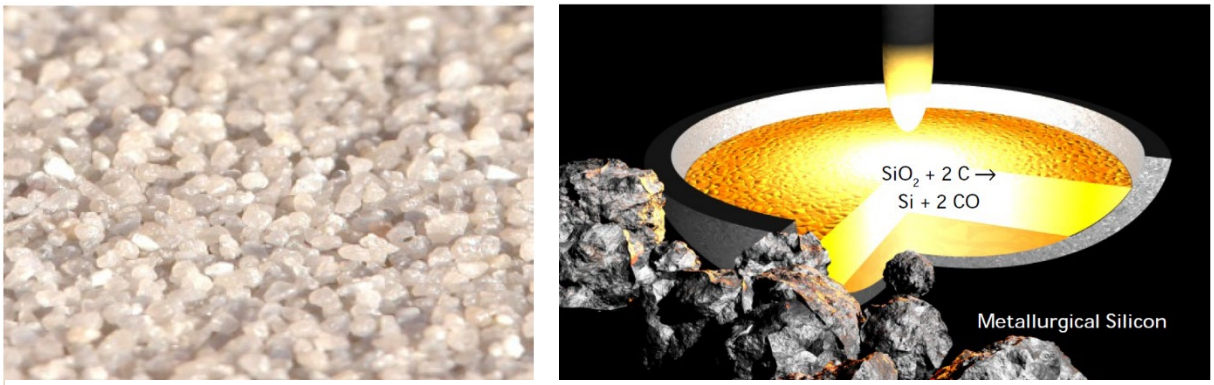

Figure. III.2: The reduction of quartz sand (above) is conducted through the utilization of graphite in a smelting reduction furnace (illustrated schematically on the right) to yield raw silicon.

III.1.3 Transformation from Metallurgical-Grade Silicon to Hyper-Pure Silicon

The initial concentration of impurities within raw silicon renders it unsuitable for application as a semiconductor in microelectronics or photovoltaics due to its significantly elevated impurity levels. To attain the requisite electronic characteristics, the metallurgical-grade silicon necessitates a purification process, transforming it into hyper-pure silicon. The initial phase towards achieving ultra-pure silicon involves the conversion of metallurgical-grade silicon into trichlorosilane (HSiCl3) through the reaction. Si + 3 HCl → HSiCl3 + H2, conducted at approximately 300°C with HCl. This step facilitates the removal of various impurities, such as iron, which remains non-volatile at these temperatures. Subsequently, trichlorosilane, blended with other gaseous chlorine compounds, undergoes multiple distillations, enhancing purity levels up to 99.9999999% ("9N"). The refined trichlorosilane is then thermally decomposed to yield poly-crystalline silicon. The formation of poly-crystalline silicon is executed through the Siemens process (refer to Fig. III.3): Purified trichlorosilane, combined with hydrogen, undergoes thermal decomposition on the surface of a heated silicon rod (approximately 1100°C). This process results in $HSiCl_3 + H_2 \rightarrow Si + 3\ HCl$, representing the reverse reaction of trichlorosilane formation.

III.1.4 Poly-crystalline and Mono-crystalline Silicon

The poly-crystalline silicon made in the Siemens process is quite pure, but it has crystal grain boundaries that create electronic imperfections. These imperfections reduce the efficiency of solar cells made from it and prevent its use in microelectronics. For making silicon wafers, the essential material for microelectronic parts, only mono-crystalline silicon is suitable.

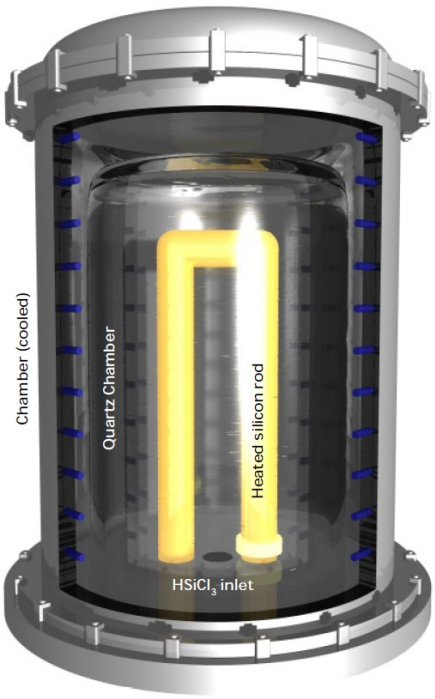

Figure.III.3: Making poly-crystalline Silicon from very pure Trichlorosilane and Hydrogen in the Siemens Process

This type of silicon is produced from poly-crystalline silicon using methods like Czochralski or Float zone, as explained in the following sections. In this process, specific and well-defined doping of the silicon with foreign atoms is also carried out. This is done to determine the electrical conductivity of the wafers made from it and to adjust it consistently across the entire crystal. Crystal Growth Using the Czochralski Method. In the Czochralski method, illustrated in Fig. 4, a silicon monocrystal is pulled from a melted silicon pool. Initially, poly-crystalline silicon (e.g., from the Siemens process), possibly with dopants, is melted in a quartz crucible at a temperature higher than 1400°C in an inert gas atmosphere like argon. The quartz crucible is placed inside a graphite crucible, which, due to its high heat conductivity, evenly transfers heat from the surrounding heater to the quartz crucible. The silicon melt temperature is kept consistently above the silicon melting point. A mono-crystalline silicon seed crystal with the desired orientation (e.g., <100>, <110>, or <111>) is dipped into the melt, serving as a starting point for crystal formation aided by heat transfer from the melt to the existing crystal. The seed crystal is slowly pulled out of the melt at a low speed (a few cm/hour), where the pulling rate determines the crystal diameter. Throughout crystal growth, both the crystal and the crucible counter-rotate to enhance the crystal's homogeneity and dopant concentration.

Before completing the crystal growth, a gradual increase in pull speed reduces the crystal diameter to zero. This precaution prevents thermal stress in the ingot, which could occur with

a sudden removal from the melt and potentially damage the crystal. The Czochralski method enables the production of large crystal diameters (currently up to 18 inches or 46 cm) and, in comparison to the Float-zone technique described later, incurs lower production costs per wafer. A drawback of the Czochralski method is the introduction of impurities, such as oxygen (typically 1018 cm-3) and carbon (typically 1017 cm-3), from the quartz and graphite crucible. These impurities reduce the minority carrier diffusion length in the final silicon wafer. Another disadvantage is a comparably low homogeneity of the axial and radial dopant concentration in the crystal caused by oscillations in the melt during crystal growth. This makes it difficult to attain high-ohmic CZ wafers with a resistivity exceeding > 100 Ohm cm. A magnetic field ("Magnetic Czochralski", MCZ) can retard these oscillations and improve the dopant homogeneity in the ingot.

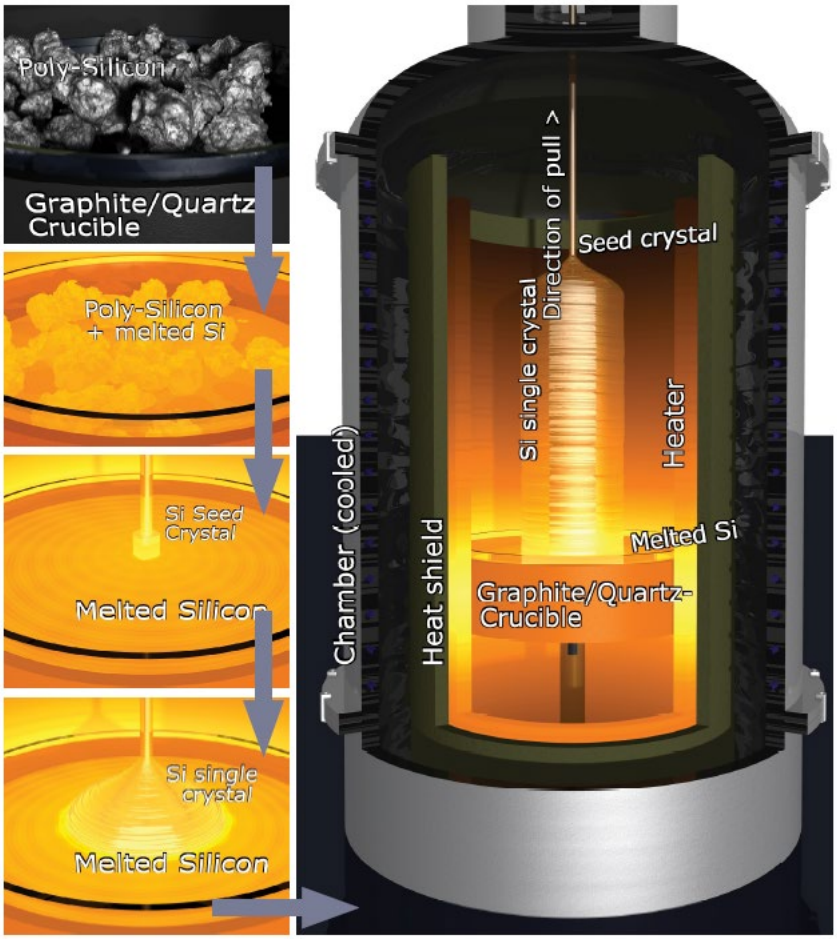

Figure. III.4: A Schematic diagram of the Czochralski technique: Top left: A quartz crucible filled with poly-crystalline silicon fragments from the Siemens process. Left 2nd from above: The silicon fragments are melted together with doping material Left 3rd from above: A mono-crystalline seed crystal is dipped into the molten silicon Bottom left: The seed crystal pulls a doped single crystal from the melt large image on the left: The schematic structure of a chamber for the crystal growing process in the Czochralski technique [9]

III.1.5 Crystal Growth using the Float-zone Method

In the float-zone (FZ) method, a single-crystal silicon seed contacts one end of a poly-crystalline silicon ingot, as shown in Fig. 5. Using an RF coil, a small region of the polysilicon is melted. Upon cooling, it transforms into single-crystalline silicon with the crystallographic orientation of the seed crystal (e.g., <100>, <110>, or <111>). The RF coil and the molten zone traverse the entire ingot. Because most impurities are less soluble in the crystal than in melted silicon, the molten zone carries impurities away. These impurities accumulate near the crystal's end, where they can be easily removed. This process can be repeated to further decrease the remaining impurity concentration. Doping occurs during crystal growth by introducing dopant gases like phosphine (PH_3), arsine (AsH3), or diborane (B_2H_6).

The float-zone technique's primary advantage lies in the very low impurity concentration in the silicon crystal. Notably, oxygen and carbon concentrations are significantly lower compared to CZ silicon, as there is no contact with a quartz crucible, and no hot graphite container is used. Furthermore, the dopant concentration in the final crystal is uniform and controllable, allowing for high-ohmic (1 - 10 k Ohm cm) wafers and those with a narrowly specified electrical resistivity. However, a drawback of the FZ method is its relatively higher cost compared to the Czochralski technique, typically three to four times more for the finished wafer. Due to technical constraints, the monocrystal's diameter is limited, allowing for FZ wafers measuring a maximum of eight inches with current technology [9].

III.1.6 Further Processing

The production journey of a silicon wafer from its initial state as a monocrystal grown through techniques like Czochralski or Float-zone involves a series of fine steps to achieve the desired quality and specifications. First, these monocrystals are ground to attain the necessary diameter and then cut into shorter, manageable cylinders using tools like a band saw. Orientation flats are incorporated to indicate the crystal orientation, while larger wafers measuring 8 inches in diameter or more utilize a single notch to convey orientation, independent of the doping type.

Two primary wafer dicing techniques are employed: the Inside Hole Saw (Annular Saw) and the Wire Saw, as shown in figure 5. The Inside Hole Saw involves sawing wafers inside a circular blade filled with diamond splinters, resulting in relatively flat and smooth surfaces after cutting. However, this method allows for the cutting of only one wafer at a time, making

it less efficient and relatively more expensive compared to wafers cut using a wire saw. In contrast, the Wire Saw method utilizes multiple parallel wires to cut many wafers simultaneously. A high-grade steel wire with approximately 100 - 200 µm diameter is wrapped around rotating rollers, cutting the mounted silicon cylinder into single wafers. The wire is coated with diamond splinters or wetted with a suspension of abrasive particles, such as diamonds or silicon carbide grains, and a carrier like glycol or oil. While this technique allows for cutting multiple wafers at once, the resulting surface is less smooth, requiring additional time for subsequent wafer lapping.

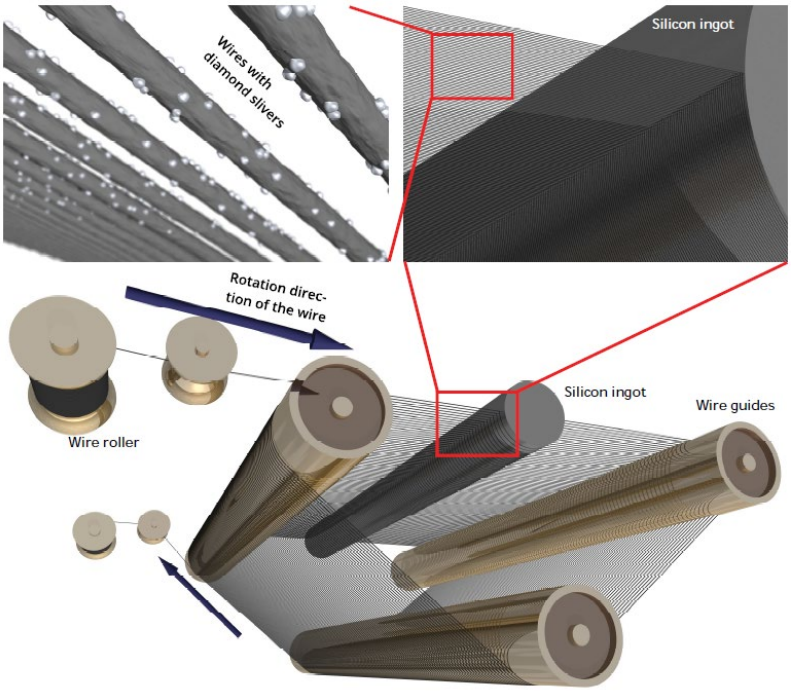

Figure. III.5: Diagram of the wire saw process. The two detailed enlargements above show the proportions between the Si-cylinder, wire spacing and wire diameter approximately to scale.[10]

Following wafer dicing, the wafers undergo a lapping process on both sides. This step serves to remove surface silicon damaged during the slicing process and achieve the desired wafer thickness. Lapping involves placing several wafers between two counter-rotating pads, utilizing a slurry with abrasive grains like Al_2O_3 or SiC with a defined size distribution. Wafer surfaces are then etched using KOH- or HNO3/HF-based etchants to eliminate damage caused by dicing and lapping processes. After etching, the wafer surfaces resemble the rear side of a finished single-side polished wafer. To attain a super-flat, mirrored surface with an atomic-

scale roughness, the wafers undergo a polishing process. This multi-step procedure employs an ultra-fine slurry containing grains of 10 - 100 nm size, such as Al_2O_3, SiO_2, or CeO_2. The combination of pressure and rotational movement between two pads works to erode and mechanically and chemically smooth the wafer surfaces. The final stage involves thorough cleaning of the wafers using ultra-pure chemicals. This step is crucial for removing residual polishing agents, ensuring the wafers are free from contaminants, and meeting stringent particle specifications. In conclusion, transforming a silicon ingot into a cleaned and polished silicon wafer involves precision at every step, resulting in high-quality wafers ready for integration into various technological applications.

III.1.7 SOI Wafers (Silicon on Insulator)

The wafer bonding method, particularly utilized in the fabrication of Silicon-On-Insulator (SOI) wafers, is a crucial technique in semiconductor manufacturing [11]. This method relies on the principle of van der Waals forces, which cause two clean and flat wafers, typically silicon, to adhere to each other when brought into contact, even at room temperature. However, the initial adhesion is relatively weak, necessitating annealing at elevated temperatures to achieve sufficient mechanical strength.

The process of producing SOI wafers via wafer bonding involves several key stages. Initially, two silicon wafers are chosen, with at least one being oxidized. These wafers are brought into close contact and subjected to annealing. Subsequently, one of the bonded wafers is thinned down through a series of mechanical grinding, polishing, and chemical etching steps until the desired thickness of the silicon film is attained, while the other wafer serves as a mechanical support.

This specific technique for SOI wafer fabrication is referred to as Bonded and Etch back Silicon-On-Insulator (BESOI). In the BESOI process as shown in Fig III.6, the thickness and uniformity of the silicon film are typically controlled by introducing an etch stop layer, commonly composed of Boron (B) or Germanium (Ge) rich material, before the wafer bonding step. This layer acts as a marker, guiding the thinning process to achieve the desired silicon film thickness accurately.

Schematically, the BESOI process involves preparing two wafers, bonding them together, thinning one wafer to the desired silicon film thickness while preserving the other as a support,

and finally, potentially incorporating an etch stop layer to control the thinning process accurately. Despite its utility, the BESOI method has a notable drawback: it requires two wafers to obtain a single SOI wafer. This characteristic increases material costs and complicates the manufacturing process compared to other methods. Nonetheless, its ability to produce high-quality SOI wafers with precise thickness control and uniformity makes it a valuable technique in semiconductor fabrication. We used a 4 inchhigh resistivity wafer for our fabrication of devices.

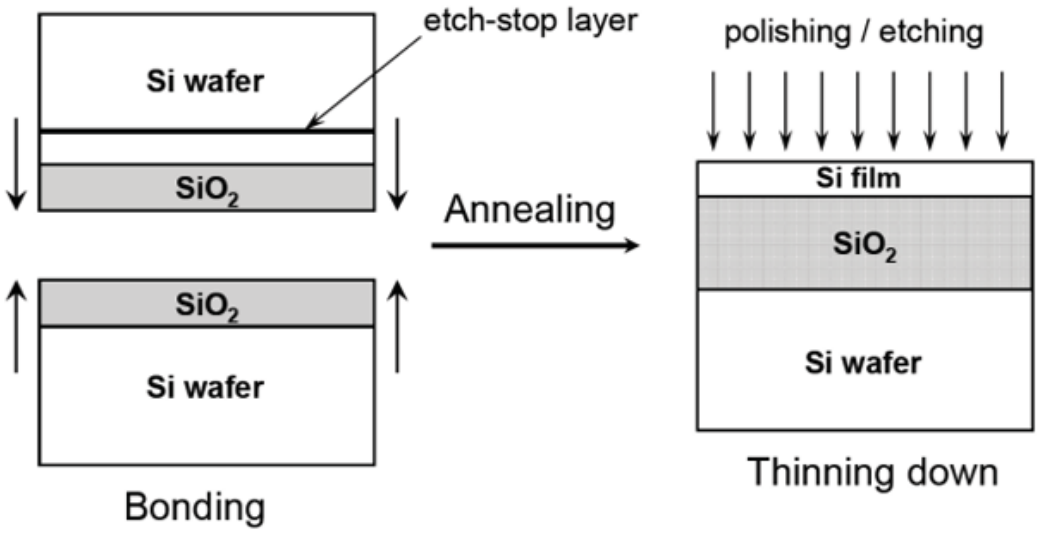

Figure. III.6: Schematic Illustration of B-SOI method

III.2 Fabrication Process

Now that we have finished studying the steps involved in processing and manufacturing Silicon wafers for SOI, it's time to focus on photolithography and Silicon Etching techniques. These techniques will be used to create the samples listed in Table 1. We have created a GDS file in the layout editor with all the 24 samples mentioned in Table 1 for the Photomask made of chrome glass. Chrome glass photomasks are an essential component in the complex process of photolithography. They are particularly crucial in the production of semiconductors and other microfabrication applications. These photomasks act as templates, helping to transfer intricate patterns onto materials like silicon wafers with high precision. A typical chrome glass photomask comprises a glass substrate with a thin chrome layer. The chrome layer is patterned using lithographic techniques to create complex designs, such as circuit patterns necessary for semiconductor devices. The chrome glass photomask is illuminated with ultraviolet (UV) light

during the photolithography process. The light passes through or is obstructed by the patterned chrome layer, generating a detailed image of the semiconductor wafer. This image guides the selective addition or removal of various materials, like photoresist, in subsequent steps of the fabrication process. Chrome glass photomasks are critical in defining the layout and geometry of integrated circuits and other microelectronic devices. The precision in creating these photomasks directly influences the quality and performance of the final semiconductor components that emerge from manufacturing. The utilized SOI wafers consist of a high-resistivity (HR-Si) silicon device layer with a thickness of 90 µm. This silicon layer is followed by a 2 µm layer of SiO_2 at the bottom, all situated on a substantial silicon substrate with a thickness of 400 µm, positioned at the extreme bottom. The Figure III.7(a) shows the cross sectional view of SOI wafer, SiO2 repersented in orange colour which is sandwitched between HR-Si(dark blue) on top and thick silicon substrate(light blue) in the bottom.

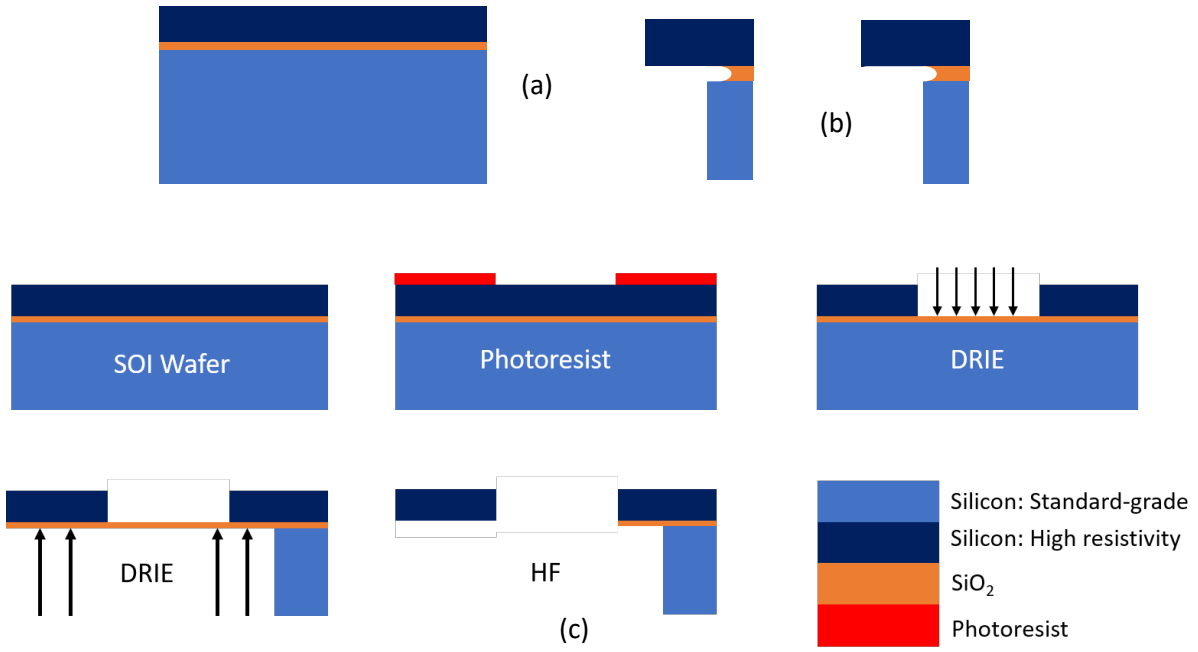

Figure III.7: Waveguide and VPC fabrication process steps (a) Silicon wafer side view (b) Device chips after the fabrication (c) Step-by-Step Schematic illustration of the fabrication process

A schematic of the topological Silicon device after fabrication is shown in the figure III.7(b) , and the whole fabrication steps are shown in FigIII.7(c). The thick Silicon handle is kept to

400 µm handle the extremely fragile silicon device layer of 90 um.The Fabrication consisted of 3 major steps:

I. Device Layer processing consisted of photolithography and silicon DRIE
II. Back Side Processing – Photo Lithography and Silicon DRIE Etching
III. Liberation of Device Chips using HF

III.2.1 Photo Lithography

Device Number	Topology Design	Function
201	Triangular holes, zigzag interface	Straight Waveguide 11 mm
202	Triangular holes, zigzag interface	Straight Waveguide 16 mm
203	Triangular holes, zigzag interface	Straight Waveguide 22 mm
204	Triangular holes, zigzag interface	Waveguide with 2 bends
205	Triangular holes, zigzag interface	Double cavity resonator
206	Triangular holes, zigzag interface	Triangular Cavity Resonator
207	Round Holes	No Waveguide structure
208	Round Holes, Bearded Interface	Straight Waveguide 11 mm
209	Round Holes, Bearded Interface	Straight Waveguide 16 mm
210	Round Holes, Bearded Interface	Straight Waveguide 22 mm
211	Round Holes, Bearded Interface	Cavity Resonator

Table III.1: List of devices in Photomask

Photolithography is a technology that creates integrated circuits by transferring a pattern from an optical mask to a substrate surface using a beam of photons.

Process Flow					
Steps	**Parameters**				
1. De-Oxidation	Dilute HF		1-2 minutes		
2. Prebake			200°C	5 "	
3.Spin Coating			Speed(rpm)	Acceleration	
	HMDS	Cover -Open	2000	1000	15"
	AZ10XT	Cover -Closed	2800	2800	20"
		Cover -Open	1500	1500	10"
	Edge Bead remover		800	1000	10"
		Cover -Open	1000	1000	10"
4.Soft bake			110°C		3'
5. Exposure	UV365 nm	D= 300mJ/cm²	Mode vacuum	contact	
6. Development		AZ400K: EDI (1:3,5)		Drop in DI water every 30 seconds	2-3"

Table III.2: Photolithography Process flow

This process is critical for miniaturization, a trend known as Moore's Law. The lithography sequence involves several steps, including cleaning and heating the wafer, depositing an adhesion promotor, spinning a liquid polymer called photoresist on the surface, and thermal bake-out. The substrate is then exposed to a light beam through a mask in an optical projection tool. The photoresist material undergoes chemical reactions when exposed to light, making it either more or less acidic. The resist is then developed and "hardbaked" to solidify it. This resist can be used as an etching, deposition, or implantation mask. The smallest device size that can be fabricated depends on the optical resolution of the lithography system, which is limited by the wavelength of the light and the lens system's ability to capture enough diffraction orders. The process flow we used for our fabrication is shown in the table III.2

III.2.2 Major Steps of Photolithography

III.2.2.1 De Oxidation HF cleaning of Silicon Wafer

A brief submersion in a DHF (dilute hydrofluoric acid) solution is commonly employed to eliminate the surface oxide layer and passivate surface defects. The underlying principle of surface passivation has advanced from F termination [12] to the more efficacious H termination [13,14]. As early as 1986, it was reported that the surface of silicon, when cleansed with HF after oxidation, becomes enveloped with covalent Si-H bonds, resulting in a near absence of

surface dangling bonds [14]. In the context of intrinsic amorphous silicon films, they are typically deposited as a chemical passivation layer subsequent to HF cleaning. This practice serves to reduce the defect density caused by the direct deposition of doped amorphous silicon films onto crystalline silicon [15]. In our process for cleaning of SOI (Silicon-On-Insulator) wafers, we utilized a 2% HF cleaning solution. Given the rapid action of HF in inducing hydrophobicity on the surface, we dip the wafer to a 2-minute immersion. Subsequently, I immersed the wafer in deionized (DI) water for a while.

III.2.2.2 Prebake

When surfaces like silicon, glass, quartz, or certain metals get heated to temperatures above 150°C, the bonds involving oxygen and hydrogen (OH bonds) break. These bonds typically create a surface good at attracting water (hydrophilic) but not so great for making a resistant coating stick well.

In our case, for the SOI wafer surface we're working on, we heated it to 200°C for 5 minutes beforehand. After that, we applied HMDS. This process helps improve the surface for the next step of photoresist coating. Deposition HMDS and resist coating on the prebaked and cleaned wafer is explained in the next section, subtitled as "Spin Coating."

III.2.2.3 Spin Coating

Spin coating is a widely employed method for uniformly applying a thin film, typically ranging from a few nano-meters to micrometres, onto a substrate. The process involves casting a solution, or "ink," onto a rotating substrate, with the centrifugal force and surface tension guiding the liquid coating into an even layer. The subsequent evaporation of the solvent leaves behind the desired material on the substrate.

The spin-coating process unfolds in four key steps: deposition, spin-up, spin-off, and evaporation, shown in FigureIII.8. Initially, the solution is deposited onto the substrate, and whether the substrate is already in motion (dynamic spin coating) or starts spinning after deposition (static spin coating), the centrifugal motion spreads the solution. As the substrate reaches the desired rotation speed, excess solution is expelled, and the fluid becomes level.

Thinning occurs dominantly due to viscous forces, marked by observable colour changes in the Fig.III.9.

Once the color stabilizes, it indicates the film is mostly dry. Thinning then transitions to solvent evaporation, with non-uniformities potentially arising from varying evaporation rates. Advantages of spin-coating include rapid processing times (typically 10-20 seconds), allowing for short cycle times suitable for industrial production. The resulting resist films exhibit smooth surfaces, precise thickness control, and excellent thickness homogeneity, particularly on circular substrates like wafers. However, challenges arise with non-circular substrates, as air turbulences at edges and corners can accelerate drying, impeding resist spin-off. Textured substrates may also compromise thickness homogeneity, leading to unintended resist film variations. Despite these limitations, the efficiency and precision of spin-coating make it a favored technique, especially in semiconductor manufacturing, where low photoresist yields (typically a few percent) have minimal impact on overall costs, especially for higher-priced end products.

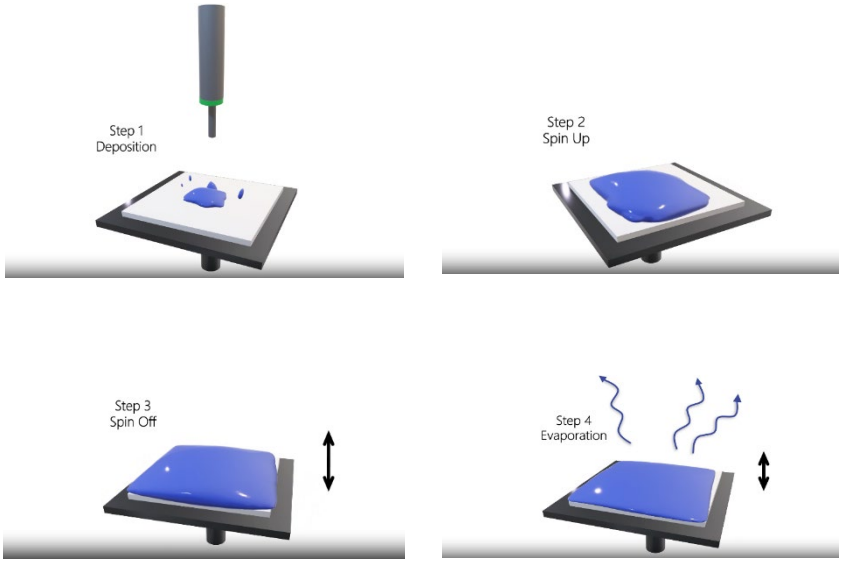

Figure III.8: Schematic of 4 critical steps of deposition [16]

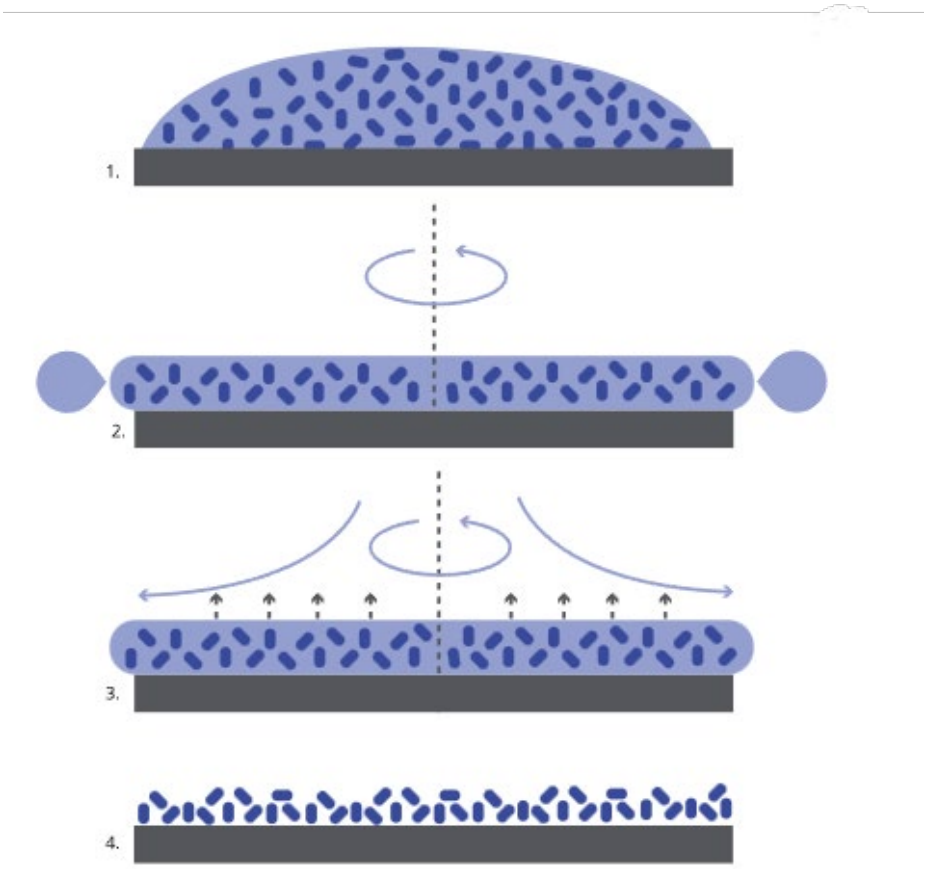

Figure III.9: Diagram illustrating the spin coating process for a small molecule in a solution using a static dispense. Initially, the surface is covered with a solution (ink) that holds the molecules in a solvent (Step 1). Following this, the surface is set into rapid rotation, causing most of the solution to be thrown off to the side (Step 2). Subsequently, airflow aids in drying up most of the solvent, resulting in a flexible film (Step 3). Finally, as the film completes its drying process, only the molecules are left on the surface (Step 4).[16]

III.2.2.4 Deposition of HMDS

For the deposition of HMDS and AZ 10 XT (thick positive tone photoresist for high resolution), we used RCD8 Coater from Suiss Microtec, as shown in the figure. Hexamethyl disilizane (HMDS) is used before the resist coating. On surfaces without water, HMDS chemically attaches its Silicon atom to the oxygen present on oxidized surfaces. This process results in the release of ammonia (NH3). The methyl groups from the HMDS fragment create a hydrophobic surface, enhancing the wetting and adhesion properties of the resist material. HMDS was applied by dispensing sufficient drops using a pipette, followed by a spin coating process at 2000 rpm with an acceleration of 1000 rpm/s for 15 seconds, as shown in table III.2. The spin speed of 2000 rpm, representing a moderate rotation pace, facilitates the uniform distribution of HMDS across the substrate through centrifugal force. The spin acceleration of 1000 rpm/s

denotes a swift speed increase, ensuring an efficient coating process within the brief spin duration. The spin is done in Cover - Open mode so that the excess HMDS evaporates.

III.2.2.5 Deposition of AZ10XT (Positive Resist)

We used AZ-10XT as our photoresist. It is a positive photoresist. AZ10XT resists have a lower optical absorption. This simplifies the exposure of (also very) thick resist films. AZ-10 XT is also a specialized photoresist designed for plating applications, offering significant improvements over typical thick DNQ-type materials. It excels in creating better sidewall profiles, aspect ratios, and photo speed. This photoresist is versatile, working seamlessly with both MIF and IN developers. A notable advantage is that it doesn't require a post-exposure bake, streamlining the fabrication process. With a wide range of single coat thickness options, from 4.0 to over 20µm, AZ-10 XT provides flexibility to meet various application needs. In simple terms, it's a high-performance solution for plating that is easy to use and adapt to different requirements. We aimed for a thickness of approximately 6µm for our photoresist. The thickness of the photoresist is determined by the small dimensions of our VPC holes in the design. The specifications for resist thickness depend on the specific device or component being created. For instance, resist layers for certain packaging requirements can be much thicker compared to those used in integrated circuit manufacturing. In microtechnology, resist thickness varies based on the micromachining process, such as bulk or etch, the component, and even the aspect ratio of the components. Achieving the final photoresist thickness involves considering its viscosity and the spin speed of the chuck during the coating process [17]. We used spin-up acceleration and speed of 2800 rpm/s and 2800 rpm, respectively, to reach our 6µm thickness target. Acceleration, the rate at which the spinning speed increases, and speed, the angular velocity of the spinning substrate, are critical factors affecting coating uniformity. Maintaining the correct resist thickness is crucial for creating precise patterns, as a thin film can either be anti-reflective or reflective. The spin coating process, when done at optimal speed, results in a uniform resist thickness.

Excess resist is thrown off at maximum spin speed, and the chuck continues spinning until most of the solvents in the resist evaporate After the spin up acceleration in cover closed mode to ensure homogeneity and avoiding contamination, we did spin off with an acceleration and speed of 1500 rpm/s and 1500 rpm. The Spin off step is done in Cover Open mode to ease the

evaporation of excess particles and solvent. During this process, acetone is sprayed on the wafer's bottom edge to eliminate resist "beading" (EBR = edge bead removal). The relevant spin speed and acceleration details are provided in Table III.2. The RCD8 Spin coater we used from Suiss-Microtec is shown in the Fig.III.10

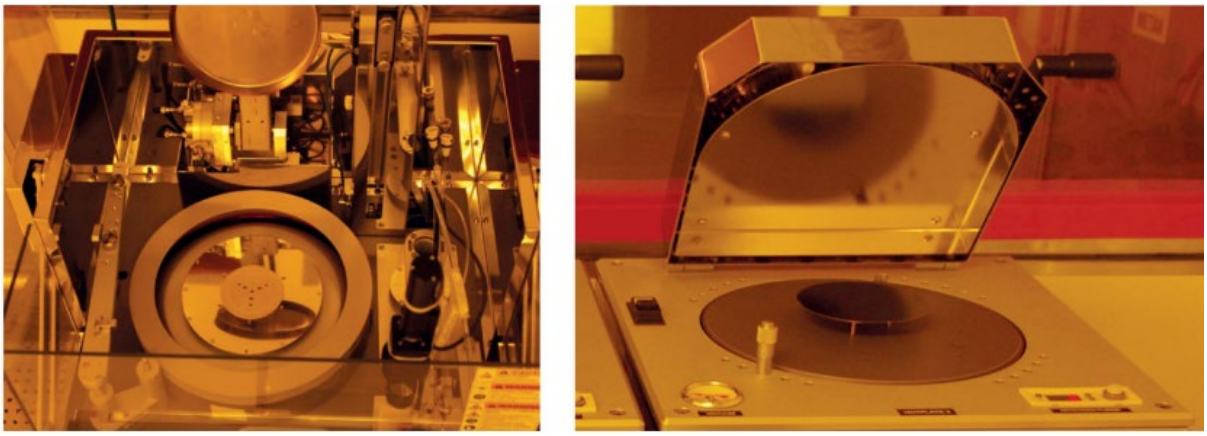

Figure. III.10:The view of RCD8 automatic Spin coater platform we used.[18]

III.2.2.5 .1 Particles or Air Bubbles in the Resist Film

Radial, streaked irregularities within the resist film commonly stem from particles or gas bubbles present in the applied coating. Detecting the source of these defects, such as through a defective photo mask, can be challenging due to the typically microscopic size of the particles.. After Spin coating of our wafer with AZ 10XT resist some defects were formed and it's shown in the Fig.III.11. In summary, a mask with dust that has undergone exposure may result in spots with dust particles that have not been exposed, and undergone subsequent development leading to defects in the final output.

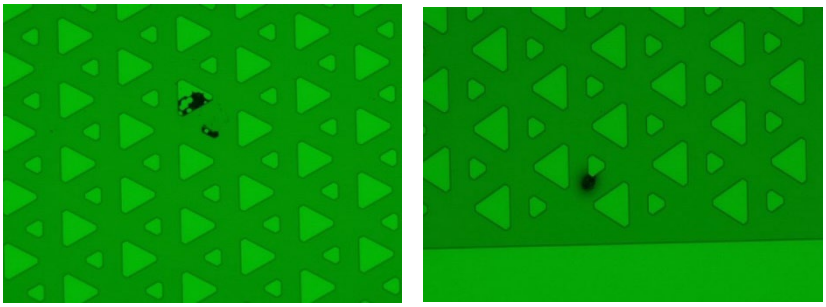

Figure.III.11:The Image captured from optical microscope after AZ 10XT coating.

III.2.2.6 Soft Bake

After applying the resist coating, we conducted a critical 3-minute soft bake at 110 degrees Celsius on a hotplate. This process is vital as it plays a key role in diminishing the remaining solvent concentration within the resist film. The soft bake is indispensable for preventing issues such as mask contamination, adhesion to the mask, resist popping or foaming during exposure, improving adhesion to the substrate, reducing dark erosion in development, averting the dissolution of one resist layer in subsequent multiple coatings, and avoiding bubbling in subsequent thermal processes like coating and dry etching.

III.2.2.7 Exposure

The preceding sections have outlined the essential procedures required to coat a substrate with a photoresist layer that is sensitive to exposure. As implied by its name, photolithography emphasizes the subsequent step of exposing the photoresist, which is a crucial process in the fabrication workflow. During this exposure phase, chemical reactions take place within the resist film, causing an increased solubility (in the case of positive resists) in the developer solution. This heightened solubility allows for the creation of a structured resist mask. Our exposure was with i-line UV365nm with an Energy = 300mJ/cm², using a vacuum contact mode in the exposure machine. Following exposure, we proceeded to prepare the development solution for further processing.

III.2.2.8 Development

The AZ 10XT photoresists work well with MIF (TMAH) or inorganic developers, and recommended options include AZ 435MIF, AZ 400K 1:3, or AZ 400K 1:4. We chose to use AZ 400K 1:3.5 and completed the development process. Development time duration is very critical sometimes. We optimized the time duration as 3 minutes after many trials.

III.2.3 Silicon Etching

Deep Reactive Ion Etching of Silicon (DRIE), also known as Deep Silicon Etching (DSiE), is a strongly anisotropic etching technique employed to generate deep, sharply defined holes and trenches in wafers or substrates, usually with elevated aspect ratios.

Our utilization of a DRIE etching machine is specifically designed for silicon. The waveguides, their tapered ends, and the VPC holes are created in a single etching process called Deep Reactive Ion Etching (DRIE). We use a special plasma process with SF6 and C4F8 gases, alternating between etching and passivation, stopping at the buried oxide layer. This allows us to achieve a depth of 90 µm with only a 6 µm resist mask. The technique was developed through collaboration between Vmicro and IEMN-NAM6 for the M-FAB pilot line dedicated to MEMS. This collaboration involved long-term recipe development to address challenges in silicon etching, including:

- Ensuring a smooth stop when reaching the bottom of the device layer without creating notches.
- Managing the effects of etching that depend on the aspect ratio, both in recipes and design.
  Handling the heat generated during processing with high aspect ratio structures, which is more challenging than standard silicon etching.
- Controlling the sidewall slope and achieving a smooth surface. Vmicro has expertise in these aspects during the steps before and after DRIE.

III.2.2.4 HF Etching

Using hydrofluoric acid (HF) is the best way to etch amorphous SiO_2, quartz, or glass quickly. However, HF is not only strong and corrosive but also very toxic in higher concentrations. It can cause serious harm like tissue damage and even death in extreme cases. To stay safe, always wear protective gear, handle only the concentration you need, and prefer pre-diluted solutions to making your own.

In Topo RUN 1, we immersed the wafer in a solution of 50% HF for 19 hours (overnight) to completely remove the SiO_2 layer laterally. Once we were done with that, we carefully picked up the entire device with tweezers and cleaned it by placing it in water for 2 minutes. After that, we cleaned it with isopropanol (VLSI) and briefly kept it on a hot plate for 2-3 minutes to dry it. Throughout the process, our top priority was to ensure safety while handling the HF solution. In the Topo Run 2, we directly put it to the HF for 7 hours after DRIE step in III.2.3 and we liberated the devices succesfully using the tweezers.

III. 3 SEM images for Topo Run 1 and Topo Run 2

The SEM images for a straight waveguide with the VPC design with triangular holes and zigzag interface are in the figureIII.12:

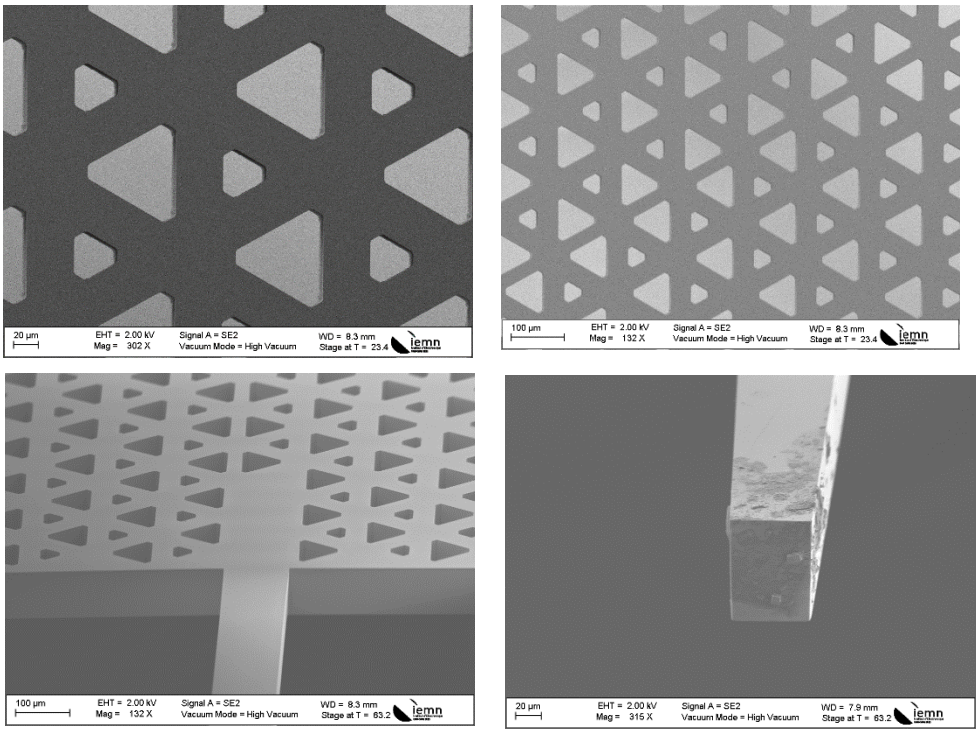

Figure: III.12 :The SEM images for VPC with triangular holes and zigzag interface the fabricated devices in TopoRun 1.

We measured the dimensions of the triangular holes and compared them to the values in GDS files for the photomask, finding that they were closely aligned. The period or lattice constant of the VPC unit cells is 137 µm, and the side length of the larger triangle is 89 µm, while the smaller one is 48 µm. The measured values from the SEM images are also within the expected range, with a maximum possible error of ±1 µm, which may occur due to technical or systemic errors. Additionally, SEM images of VPC designs with circular holes and a bearded interface are shown in Fig: III.13

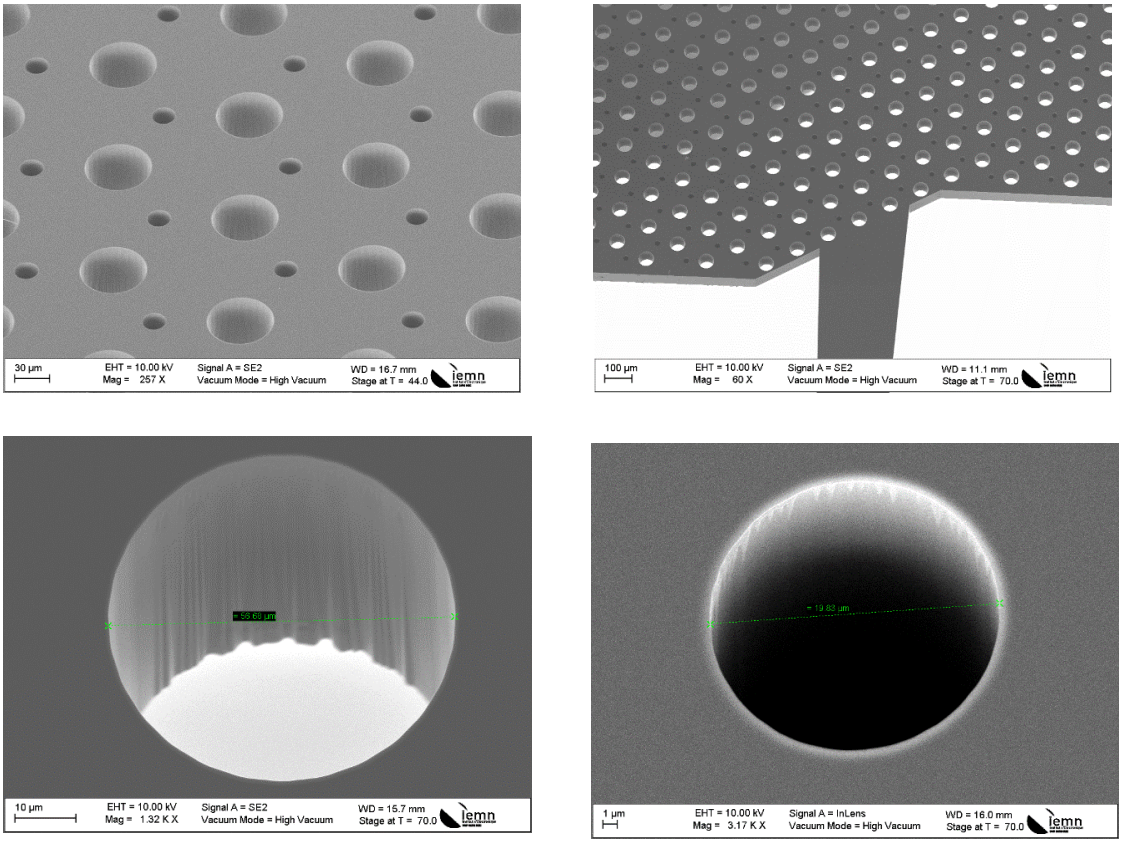

Figure.III.13: The SEM images for VPC with circular holes and the fabricated devices in TopoRun 1

The lattice constant or period of the VPC design with round holes and a bearded interface is 127 µm. The diameters of the larger and smaller round holes, as per the GDS files, are 54 µm and 18 µm, respectively, falling within the range of ±1 µm when compared to the SEM images. This alignment is promising for further progress in fabrication.

In the second fabrication run, the goal was to integrate passive silicon functional VPC devices with metallic blocks to facilitate VNA measurements. Inserting inverted tapers into the WR 1.5 is always challenging in VNA characterization. TopoRun2 followed the same steps of photolithography and silicon DRIE as outlined in the previous sections. Unlike the first run, PVA Tepla cleaning was removed in TopoRun2 as a very new SOI wafer was used. The SEM images obtained from TopoRun 2 wafer -1 are presented in Figure: III.14 .The SEM images showed some scallop shaped structures insides the VPC holes. We later identified them as silicon scallops which are the remains from silicon etching process (DRIE) of the device layer [19].

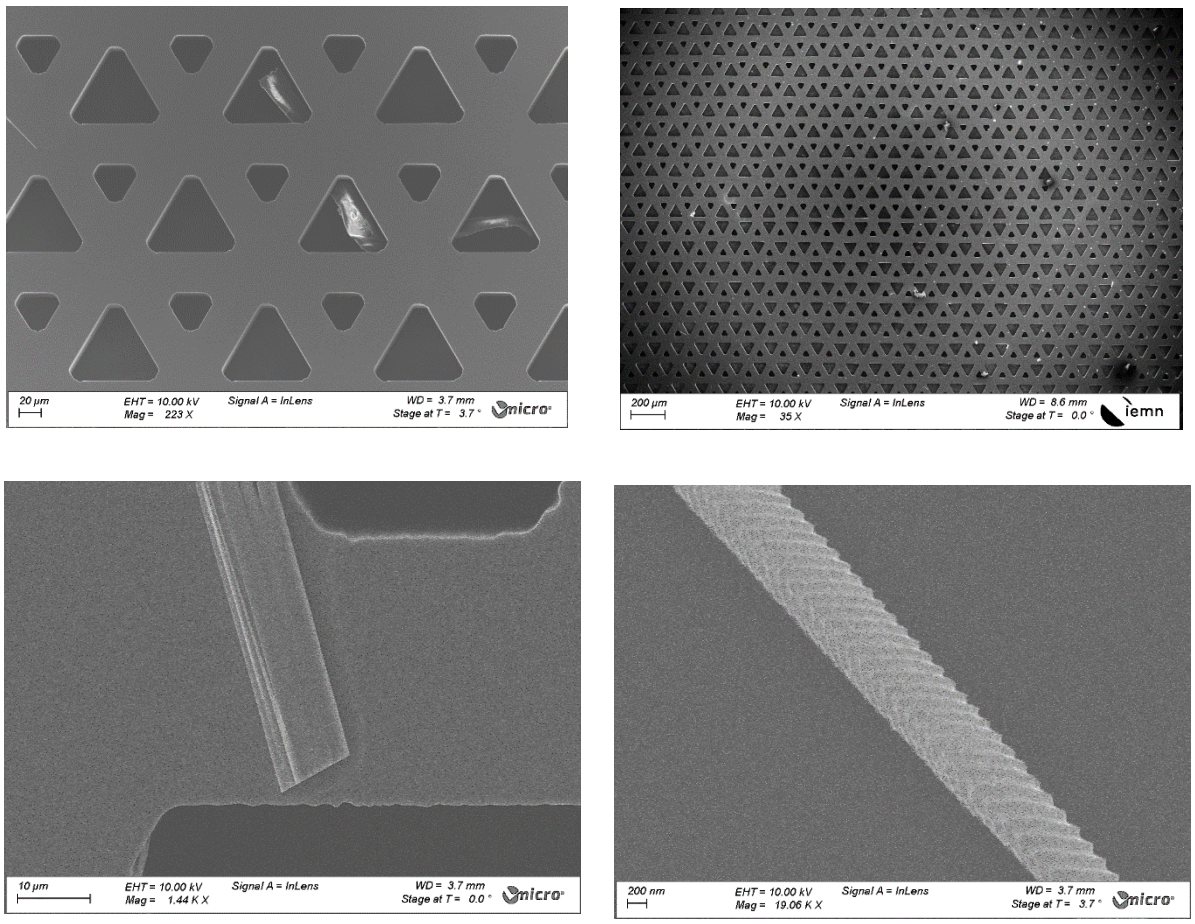

Figure: III.14 :The SEM images for VPC with triangular holes and the fabricated devices in TopoRun 2

We also measured the thickness of the device layer using SEM. The thickness of the device layer separated from the first SOI wafer is measured as 89.16 um on average. The SEM images Wafer 2 for the VPC designs with round holes with bearded interface again shown in Fig: III.15. VPC designs with round holes and bearded interfaces show strong alignment with measurements taken from GDS files. The SEM images are shown in FigIII.16: Silicon scallops are also visible in some holes of the VPC unit cells.

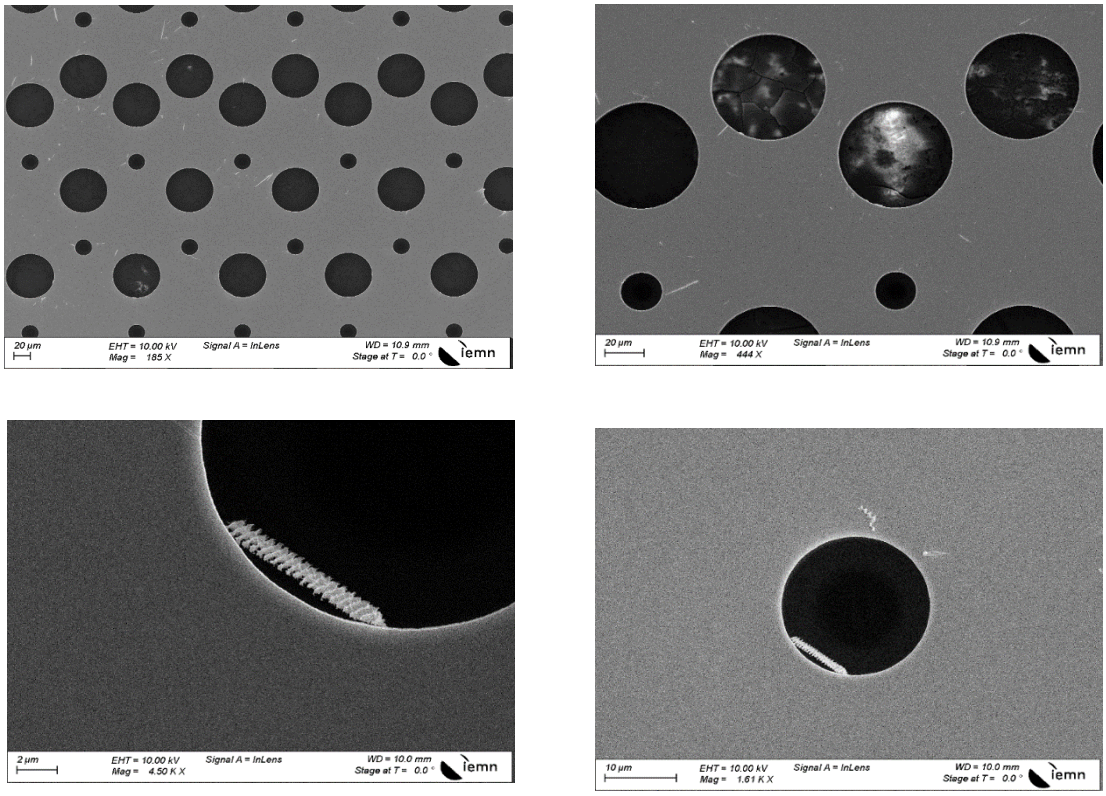

Figure: III.15 : The SEM images for VPC with circular holes and the fabricated devices in TopoRun 2

Conclusion of this Chapter

This chapter presented the Silicon processing and Fabrication technology used for the proposed VPCs designs and 2 rounds of fabrication and its successful endeavor is showcased. In the second part, we briefly described the technological process used by us in collaboration with Vmicro (our collaborator in the TOPOTERA project) for the fabrication of these THz components and the final VPC designs. We presented all the processes involved in photolithography in detail used for the fabrication of both TopoRun 1 and TopoRun 2. In the final part, we showcased the SEM images of all the fabricated samples to analyze the perfection to proceed to further Experimental characterization and application experiments. All the devices fabricated were more or less ready for characterization from SEM images. The results of the measurements based on these experimental setups and techniques are presented in the next chapter.

References

1. Pappas, S. (2018). "Facts about Silicon." Live Science. Available at: https://www.livescience.com/28893-silicon.html [Accessed 12th November 2021].
2. Brian, M. (2021). "How Semiconductors work." HowStuffWorks Electronics. Available at: https://electronics.howstuffworks.com/diode.htm [Accessed 12th November 2021].
3. "Semiconductor Technology A to Z(na): Everything about semiconductors and wafer fabrication." Halbleiter.org. Available at: https://www.halbleiter.org/en/fundamentals/doping/ [Accessed 12th November 2021].
4. Hummel, R. (2012). Electronic Properties of Materials (4th ed.). New York, NY: Springer.
5. "The Silicon Wafer Manufacturing Process." SVM. Available at: https://svmi.com/service/silicon-wafer-manufacturing-process/.
6. PNAS (2015). "Nanopurification of silicon from 84% to 99.999% purity with a simple and scalable process." Proceedings of the National Academy of Sciences, 112(44), 13473-13477. https://doi.org/10.1073/pnas.1513012112
7. "News tagged 18-inch wafer." Digitimesasia (2021). Available at: https://www.digitimes.com/tag/18-inch_wafer/0015757.html [Accessed 12th November 2021].
8. Addison Engineering (na). "About Wafers." Available at: hu [Accessed 12th November 2021].
9. Microchemicals. (n.d.). Czochralski & Floatzone Silicon Ingot Production. Retrieved from https://www.microchemicals.com/technical_information/czochralski_floatzone_silicon_ingot_production.pdf
10. MicroChemicals. (n.d.). Silicon Wafer Production Specification. Retrieved from https://www.microchemicals.com/technical_information/silicon_wafer_production_specification.pdf
11. Rudenko, T.E., Nazarov, A.N., & Lysenko, V.S. (2020). The advancement of silicon-on-insulator (SOI) devices and their basic properties. Semiconductor Physics, Quantum Electronics & Optoelectronics, 23(3), 227-252. V. Lashkaryov Institute of Semiconductor Physics, NAS of Ukraine, 45, prospect Nauky, 03680 Kyiv, Ukraine. https://doi.org/10.15407/spqeo23.03.227
12. Weinberger B.R., Deckman H.W., Yablonovitch E., Gmitter T.J., Kobasz W., Garoff S. The passivation of electrically active sites on the surface of crystalline silicon by fluorination. J. Vac. Sci. Technol. A. 1985;3:887–891. doi: 10.1116/1.573340. [CrossRef]
13. Chabal Y.J., Higashi G.S., Raghavachari K., Burrows V.A. Infrared spectroscopy of Si(111) and Si(100) surfaces after HF treatment: Hydrogen termination and surface morphology. J. Vac. Sci. Technol. A. 1989;7:2104–2109. doi: 10.1116/1.575980. [CrossRef]
14. Yablonovitch E., Allara D.L., Chang C.C., Gmitter T., Bright T.B. Unusually Low Surface-Recombination Velocity on Silicon and Germanium Surfaces. Phys. Rev. Lett. 1986;57:249–252. doi: 10.1103/PhysRevLett.57.249.
15. Tanaka M., Taguchi M., Matsuyama T., Sawada T., Tsuda S., Nakano S., Hanafusa H., Kuwano Y. Development of New a-Si/c-Si Heterojunction Solar Cells: ACJ-HIT (Artificially Constructed Junction-Heterojunction with Intrinsic Thin-Layer) Jpn. J. Appl. Phys. 1992;31:3518–3522. doi: 10.1143/JJAP.31.3518.
16. Ossila Ltd. (n.d.). Introduction to Spin Coating. Retrieved from https://www.ossila.com/pages/spin-coating#introduction-to-spin-coating
17. Cullmann, & Topper. (January 2001). Thick photoresist patterning for WLP applications. EET India.
18. SUSS MicroTec AG. (n.d.). RCD8 - Spin Coater for high volume production. Retrieved from https://www.suss.com/en/products-solutions/coater-developer/rcd8
19. Lin, Y., Yuan, R., Zhang, X. et al. Deep Dry Etching of Silicon with Scallop Size Uniformly Larger than 300 nm. Silicon 11, 651–658 (2019). https://doi.org/10.1007/s12633-018-9948-3]

Chapter IV :

Characterization: Methods and Results

IV.1 Experimental Setups

IV.1.1 Vector Network Analysis

A Vector Network Analyzer (VNA) is a measuring system that examines how a component or a network reacts to high-frequency signals. It measures the power of these signals going into and coming back from the component or network. Unlike voltage and current, power waves can be accurately measured at high frequencies. At each frequency point, the VNA records both the amplitude and phase of the signal. Using a set of microwave/waveguide circuits, the VNA calculates important parameters like return loss and insertion loss of the tested network. It can display these results in various formats like real/imaginary, magnitude/phase, or Smith chart. For testing high-speed systems, VNAs are crucial for analyzing multi-port networks containing components such as connectors, filters, amplifiers, and transmission lines. The measurement bandwidth and frequency points across the selected range are adjustable settings for a VNA measurement. The VNA operates by applying a continuous wave signal at each frequency and adjusting the magnitude as needed. To ensure accurate measurements and minimize errors, the VNA must cover frequencies up to the second harmonic for timing margin error reduction and up to the fourth harmonic to reduce voltage margin error.

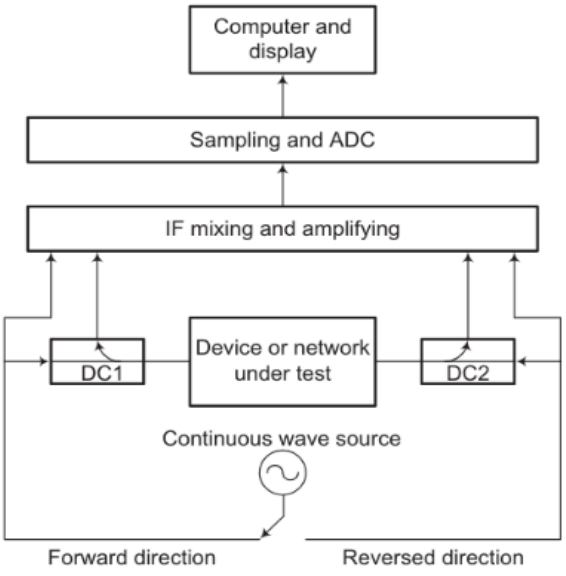

Figure IV.1: The Block diagram for VNA architecture [1]

The architecture of a VNA involves several components including RF sources, directional couplers, frequency converters, reflectometers/power detectors, A/D converters, and an internal computer shown in Fig IV.1 [1]. The continuous wave signal for testing is generated by an RF source and swept over the specified bandwidth in small frequency steps. A portion of this signal serves as a reference, while the main fraction is directed to the device under test (DUT). Reflected and transmitted signals are processed and converted to digital format for analysis. Return loss, which indicates the mismatch at the input port of the DUT, is calculated from the ratio of reverse reflected power to incident power. Insertion loss, representing the gain or loss of the DUT, is determined by the ratio of transmitted power to incident power. Additionally, VNAs can calculate other parameters such as phase, standing wave ratio, group delay, and impedance.

IV.1.1.1 S parameters extraction using Vector Network Analyzer

S-parameters refer to the scattering matrix components that connect the various inputs and outputs of a system with N ports. In an optical system, this is equivalent to the relationship between the incident light and the reflected and transmitted light that passes through a medium. Figure IV.2 shows a schematic of a two-port S-matrix and its optical equivalent. This type of system is represented by the expression below:

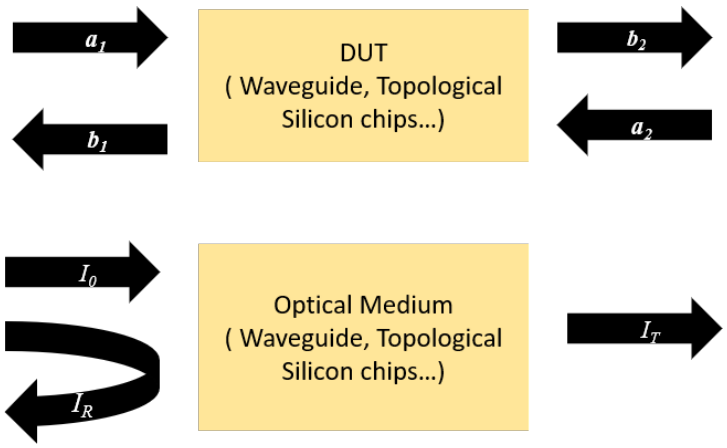

Figure IV.2: Two-port S parameters model (top) and its scalar equivalent for an optical transmission system (bottom)

The parameters S11 and S22 represent the complex wave reflections at ports 1 and 2, respectively. Whereas, S21 and S12 correspond to wave transmission from ports 1 to 2 and 2 to 1, respectively. In the RF and mmW region, VNAs are tools that can measure both the phase and amplitude of these parameters. With the help of Vector Network Analyzer extenders

(VNAX), it is now possible to make these measurements in the THz region for frequencies up to 1.5 THz [2]. In our experiments, we used a Rohde & Schwarz VNA with two extenders (VNAX) coupled to metallic waveguide WR-1.5 ports between 500-750 GHz to make two-port measurements. This technique has several advantages.

- With its broad dynamic range of 80 dB, this device can measure the resonant modes of PhC cavities that have very low transmission within the bandgap.

- Additionally, its high resolution and speedy sweep capabilities enable the measurement of cavities with high Q factors, with a frequency step size of less than 10 MHz within a short amount of time.

-The VNAX ports are equipped with MWGs at their outputs, making coupling to Silicon waveguides highly efficient with very low insertion losses while conserving the single mode behavior of the Si waveguide. An exact silicon waveguide to metallic waveguide assembly has also been used in a previous project in our lab [3]. The inverted taper structure and its mode analysis coupling efficiency are detailed in Section II.2.3, Ref [3].

The view and the schematic of the experimental setup are shown in Figure IV.3. Polarization twisters are added to the WR-1.5 waveguides ports to match the required Ex polarization of the Si waveguides input and output tapers. The measurements were calibrated using a waveguide TRM (Thru, Reflect, Match) method [4], in the plane of silicon WG injection, to correct and remove the impairments from the measurements. To achieve low insertion losses, the Si waveguide's taper must be inserted 1 mm inside the WR-1.5 port, as illustrated [3]. To ensure proper alignment, we used an optical lens with f = 50 mm or a camera to visualize the input of the WR-1.5 ports. All samples are mounted on an X, Y, and Z micropositioner translational stage to achieve precise control over the sample alignments. Such experimental arrangement enabled close to 10µm precision for the sample positioning. This method is highly sensitive and accurate for extracting waveguide loss and characterizing cavities. However, it is not possible to analyze the modal dispersion of this waveguide using this method, as it has a narrow frequency band and single-mode behavior.

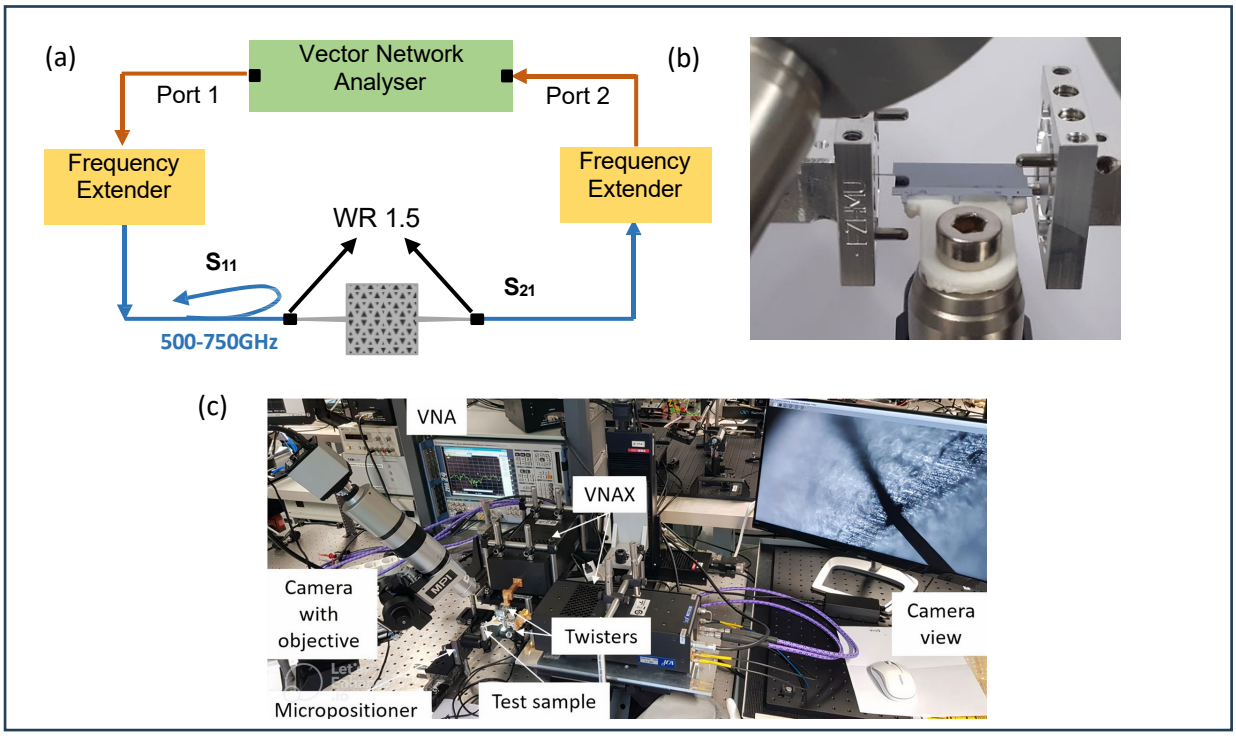

Figure IV.3 : Experimental Setup (a) S parameters measurements experimental setup schematic (b) View of the coupling of the topological devices to hollow-core waveguide measurement interfaces. (c)View of the total experimental setup in the laboratory

IV.1.1.2 Group Delay

In a Vector Network Analyzer (VNA), the group delay refers to the time it takes for a signal to pass through the device being tested or the network being examined. It indicates how much the phase of a signal changes with frequency, essentially indicating how the different frequency parts of the signal are delayed as they travel through the network. In simpler terms, group delay is like looking at how much time it takes for different parts of a signal to get through a device or network when we're studying it with a VNA. It's useful because it helps us understand how the phase of the signal changes over different frequencies, which is important in things like communication systems and signal processing. Mathematically as in equation IV.1, the group delay (τg) is defined as the derivative of the phase (ϕ) of the network for angular frequency (ω), expressed as:

$$\tau_g = \left|\frac{-d\phi}{d\omega}\right| \qquad \text{(IV.1)}$$

Beyond the VNA technique, the THz-Time Domain Spectroscopy (THz TDS) is a great complementary tool for waveguide time domain analysis.

IV.1.2 THz Time-Domain Spectroscopy (THz-TDS)

Terahertz Time-Domain Spectroscopy (THz-TDS) is a well-known spectroscopic technique that operates in the terahertz frequency range. THz-TDS has extensive applications in the characterization of materials, molecular identification, and exploring various interactions involving matter within the THz spectrum. Typically, THz-TDS uses a photoconductive antenna (PCA) or non-linear crystals to emit and detect THz frequencies. The operational principles of THz-TDS are depicted in Figure IV.4. In this setup, a femtosecond pulsed optical laser is directed onto the semiconductor material of the PCA, facilitating the generation of photocarriers. These carriers are then accelerated by a direct current (DC) bias field applied to the dipole antenna, thereby generating a THz pulse.

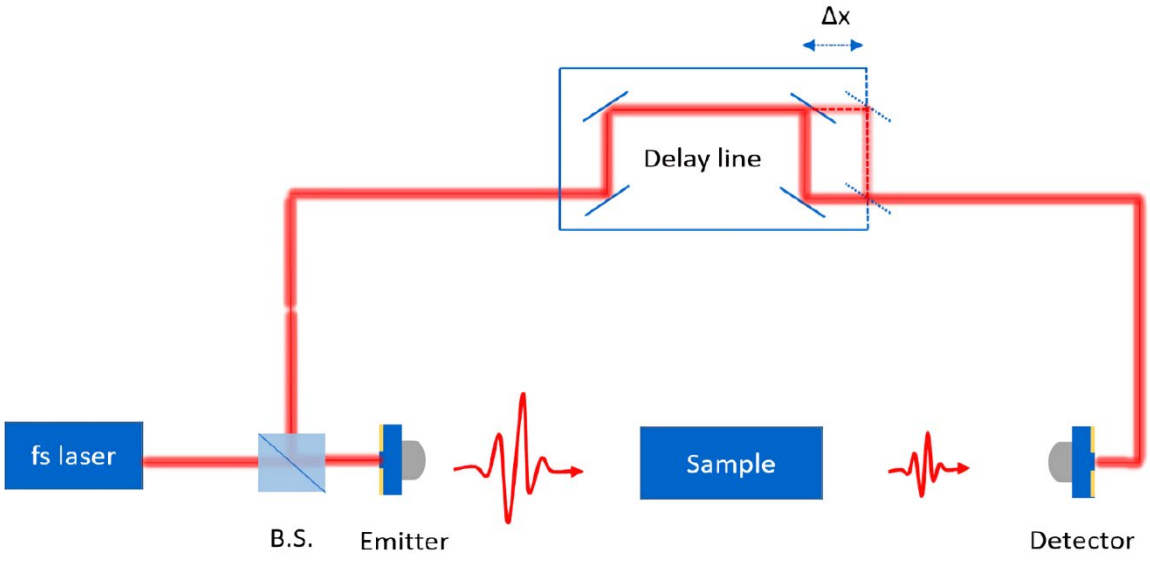

Figure IV.4 : Experimental scheme of a THz-TDS [3]

The femtosecond beam is divided into two optical paths. The first portion activates the emitter, while the second propagates via a mechanical time delay line towards the detector (PCA). The detector, illuminated by these femtosecond pulses and exposed to the THz pulse, enables the measurement of an induced photocurrent at time t.

By manipulating the translational stage in the delay line pathway, the profile of the THz electric field E(t) in the time domain is sampled (1 point being related to a specific location of the delay-line).

Subsequently, employing Fourier transform techniques enables the determination of the amplitude and phase of the electric field in the frequency domain. The key advantage of this methodology lies in its broad bandwidth, delineated by the emitter and detector carrier lifetimes, as well as the minimal physical displacement Δx in the delay line. However, compared to a VNA technique, the frequency resolution is limited by the delay-line maximal available delay. Moreover, its coherent nature affords a high signal-to-noise ratio (SNR), achieved by exclusively detecting THz radiation while mitigating the influence of blackbody and other thermal radiations[3].

IV.1.3 Data Communication Experimental Setup for Topological Devices

Beyond characterization of the waveguides using VNA, ie using a CW swept signal or using TDS to get the impulse response with several THz bandwidths, a third type of measurement can be carried out in the THz range. In this case, a modulated signal is used instead of a single tone, to inject any device with a wideband signal and assess the overall response. In such a case, it gives a first level of validation of the passive device (of any type) integrated with a whole communication testbed.

To present this part, let's remind that we have considered advanced designs for silicon chips that use topological Valley Photonic crystals and have several passive functions. These designs work at a frequency of 600GHz and are ideal for high-speed communication systems. We conducted data communication experiments to measure the device's performance in terms of EVM, BER, SNR for a fixed data-rate. In this work, we used a THz transmitter based on a uni-travelling carrier photodiode working in the 600GHz band [5]. At the receiver end, we used a subharmonic mixer using GaAs Schottky technology with 10+/-1dB conversion losses. The testbed includes a pair of optical tunable laser sources in the 1.55 µm optical window (C-band), and one of the lasers is modulated using a wideband I/Q optical modulator. The baseband data from an arbitrary waveform generator is filtered using 0.1 root-raised cosine to shape the optical and associated THz spectra. The second laser, which is not modulated, is mixed with the first one before an optical amplification stage. After photomixing, THz waves are generated using a UTC-PD.To evaluate the performance of the topological devices with modulated signals propagating into it, we first measure the back-to-back performance, by directly connecting the transmit and receive circuits. This is done by connecting the UTC-PD output and WR1.5 input of the SHM. Here, we used QPSK and QAM16 modulation schemes. QPSK and QAM are digital modulation techniques that are widely used in various communication

technologies that require high bandwidth efficiency. The primary goal of these modulation techniques is to increase the number and speed of transmitted bits within a given bandwidth while minimizing the error rate. QPSK achieves this by altering the angle of the carrier in four distinct angle values while keeping the amplitude constant. On the other hand, QAM maintains the frequency of the carrier while adjusting the amplitudes of the in-phase and quadrature components. We measured the error vector magnitude (EVM) against the relative power emitted at the transmitter side. EVM (Error Vector Magnitude) is the Root Mean Square (RMS) of the error vectors computed and expressed as a percentage of the EVM Normalization Reference. Then, the device under test (DUT) is inserted between Tx and Rx, and the EVM is measured again with transmit power. The power shift between the two curves is typically the power penalty induced by the presence of the DUT. In a first approximation should correspond to the transmission of the device, in the case of a pure lossy and non-dispersive DUT, as in this case, the DUT can be considered as a lossy delay line.

To do this, we insert the topological device input port taper into a probe extender, which is connected to the UTC-PD using a metallic hollow-core WR 1.5 waveguide at the transmitter side. The topological device output port taper is then interfaced with the GaAs Schottky sub-harmonic mixer (SHM). The down-converted signal is amplified by 30 by an IF amplification stage (SHF-810 [9]) and detected by a wideband oscilloscope for modulated signal analysis, namely error vector magnitude (EVM), thanks to the use of the vector signal analysis (VSA) tool [10] and bit error rate (BER) measurement.

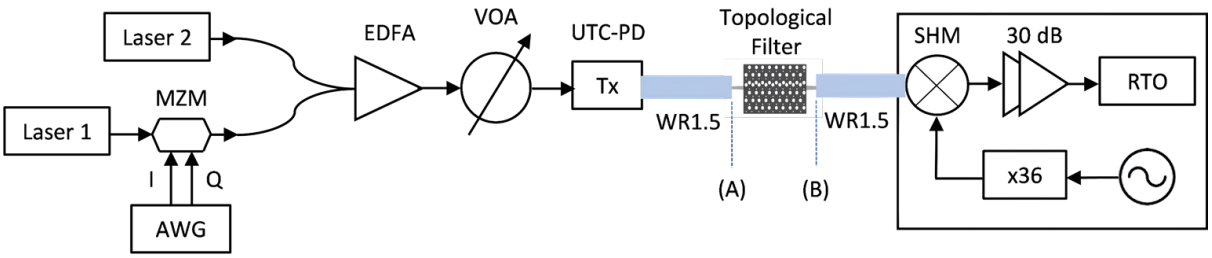

Figure.IV.5:Experimental testbed. AWG: Arbitrary Waveform Generator, MZM: Mach-Zehdner Modulator, EDFA: Erbium Doped Fiber Amplifier, VOA: Variable Optical Attenuator, UTC-PD: Unitravelling carrier Photodiode, SHM: Sub-Harmonic Mixer. The SHF 810 has a 30 dB gain for the IF frequencies used. RTO: Real-time Oscilloscope. The topological filter is inserted between the 2 WR1.5 waveguide sections. Back-to-back (B2B) performance is measured when Plane (A) and (B) are connected.

IV. 2 Results

This section presents the results of the VNA characterization of THz topological devices. The measurements mainly focus on the S21 (transmission) and associated group delay. Table III.1 lists the topological devices with different functions. Two designs of straight waveguides, with one of the waveguides, also behaving like a bandpass filter, ring resonators, and double cavity resonators.

IV.2.1 THz Topological Straight Waveguides

We designed straight waveguides with triangular holes and Zigzag terminations at three lengths. Taper waveguides described in Section II. 2 are coupled to the topological waveguides. Two port S parameters measurements are done using VNA with frequency extenders VNAX in the 500-750 GHz frequency band. A PLA (Polylactic acid) 3D printed holder was used to easily handle these structures shown in light ash color. These structures are glued enough away from the topological waveguide, as illustrated in Fig IV.6.

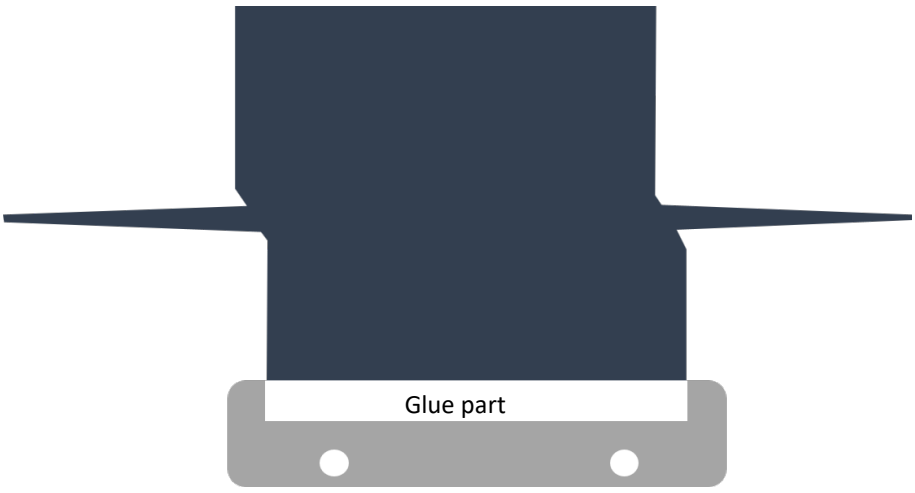

Figure IV.6: The schematic of the device glued with PLA (Polylactic acid) 3D printed holder to ease the handling.

The sample under test is mounted on an X, Y, and Z translational micrometer stage with 2µm sensitivity for precise alignment. A camera with an objective is used to enlarge the visualization at the MWG input of port 1. The waveguide taper is then introduced by 1 mm inside the port and aligned by controlling its central position in the XY plane. The second port is mounted on a translational stage that allows alignment with the second taper.

S21 and S12 represent the transmitted normalized power in dB scale from port 1 to 2 and 2 to 1, respectively. These two parameters are fundamentally equal and can be written as:

$$S_{21} = 10\log_{10}\left(\frac{I_{\text{Transmitted}}}{I_0}\right) \qquad (IV.2)$$

Similarly, the reflected normalized power S11 or S22 are represented by:

$$S_{11} = 10\log_{10}\left(\frac{I_{\text{Reflected}}}{I_0}\right) \qquad (IV.3)$$

where $I_{\text{Transmitted}}$, and Ireflected correspond respectively to the transmitted and reflected intensity, and I0 the incident one.

Since losses in a waveguide proportionally increase with its length augmentation (after substration of input/ouput taper coupling and intrinsic losses), we initally expected it would be possible then to extract the propagation losses from the linear dependence between waveguide losses and lengths. This is known as the cut-back method.

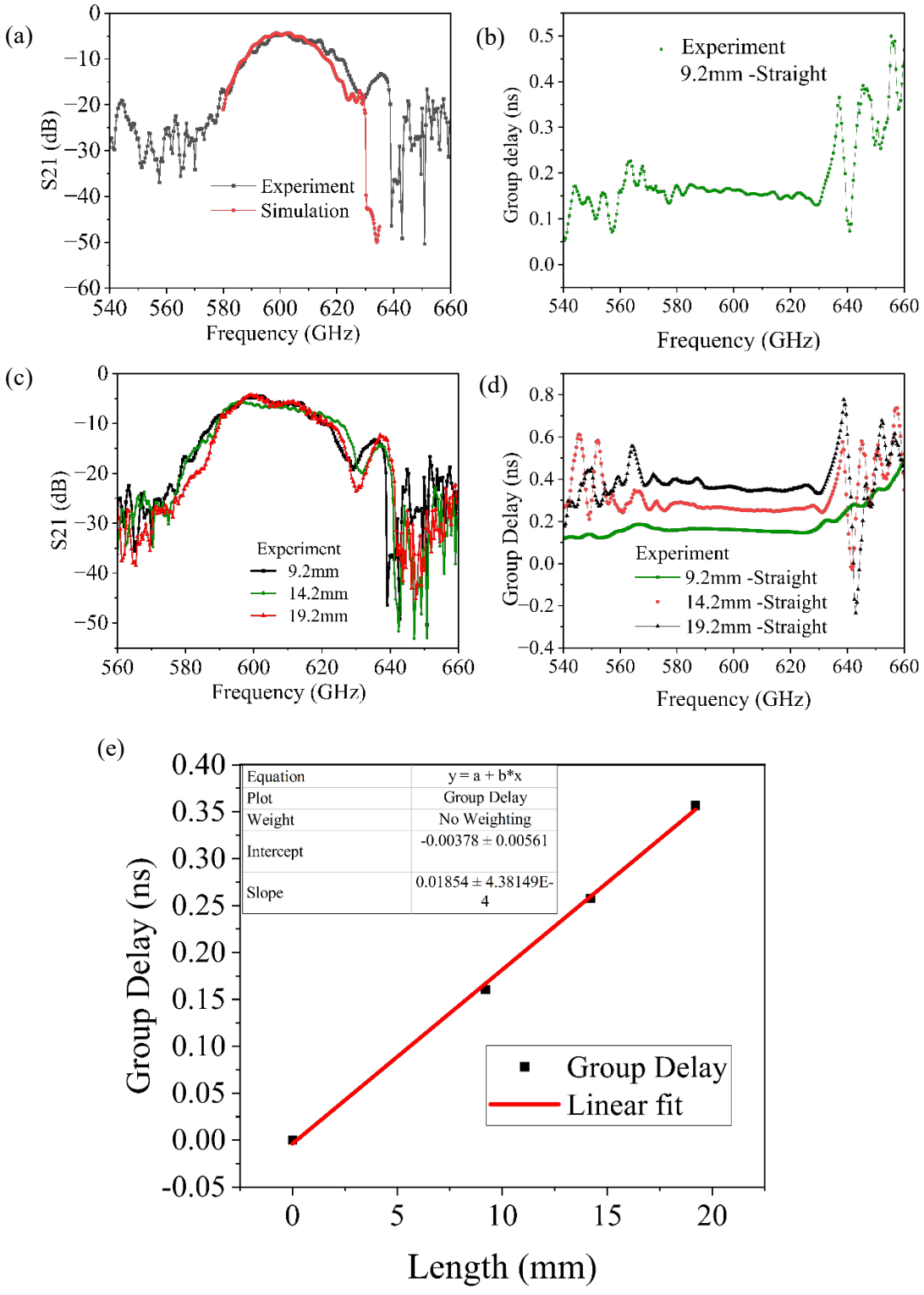

Figure IV.7: Transmission and Group Delay of straight topological waveguides with triangular holes (a) S21 calculated by simulation (red) and extracted from VNA characterization (black) (b) group delay extracted from VNA characterization for 9.2 mm straight waveguide (c)S21 from VNA for straight waveguides with 3 different lengths 9.2 mm,14.2 mm,19.2 mm (d) Group Delay from VNA for straight waveguides with different lengths 9.2 mm,14.2 mm, 19.2 mm (e) Group delay vs length at 600 GHz show a linear increase to length of the waveguide.

Fig IV.7.a shows the Transmission measured with the experiment and simulated one for the design Both are closely aligned and show promise. A minor frequency shift in the experimental curve is expected, typically around 9.8 GHz, which is less than 2% of the central frequency. Such deviations are common in real-world scenarios, like variations on dielectric constant or wafer thickness.

Fig IV.7.b shows the group delay for the same frequency range. 580 GHz to 620 GHz gives the group delay, which is less than 0.2 ns. As the group delay is clearly increasing with waveguide length, the energy is guided and propagates within the topological device as shown in Fig IV.7 (e). Even though we expected a length increase like 9.2 mm, 14.2mm, and 19.2 mm, we could not distinguish a clear S21 decrease among using the transmission curves. This means that the overall losses are dominated by the injection losses from the input and output tapers. Compared to the non-topological silicon waveguides, which give a clear distinction in the transmission even in slight variations in length [6]), for topological straight waveguides, 5.2 mm does not provide much distinction in transmission level as shown in Fig IV.7.(c), which may be due to the effect of topological protection offered by the zigzag terminations. But for the group delay, a linear increase concerning length is noted, as shown in Fig IV.7.(e).

To verify the robust nature valley kink states or edge modes are created at the interface of VPC types as shown in Figure IV.8 (top-left and top-right), We also designed one bent waveguide and compared the transmission and group delay with the straight one. The S21 and group delay are shown in Figure IV.8 bottom- left and bottom-right. Low loss and low dispersion areas were spotted in 590-620 GHz. The results prove that topological valley kink states are promising for THz communication applications enabling high-speed 6G data transfer systems.

We have also designed topological straight waveguides that incorporate VPCs with round holes, and bearded termination between VPC type A and Type B as shown in Fig.IV.9(a). The transmission and group delay data are shown in Figure IV.9(b). The spectrum displays sharp ends and a wide bandwidth of 570-650 GHz at the edges. To determine the cause, we conducted further simulations to see if it was due to the topological design. We discovered that the design is very similar to uncladded waveguides, with the only difference being asymmetry in the hole structures and terminations. The sharp edges and wide bandwidth are not a result of the topological property, but rather the photonic crystal design, as illustrated in Figure IV.10. But it's an advantage in topological design that the modes are immune to defects and robust in the

wide bandwidth compared to the normal photonic crystal design with line defects that gives wide bandwidth.

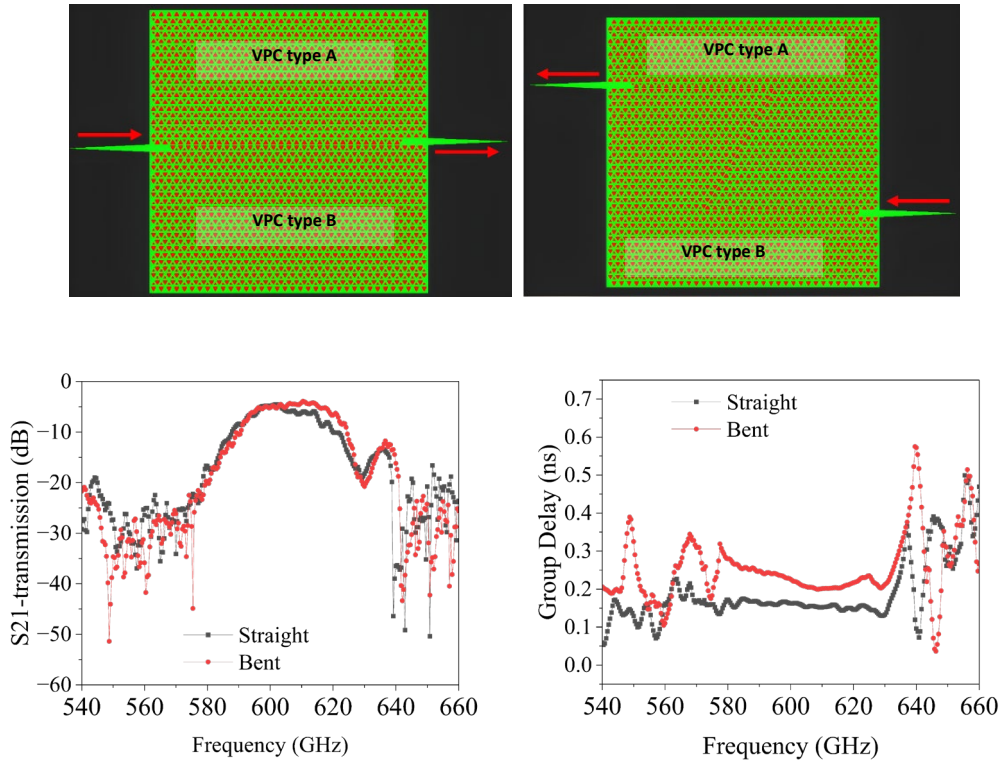

Figure IV.8: Schematic of straight and Bent waveguides. The transmission (bottom left) and Group Delay (bottom right) compared for straight topological and bent topological waveguides

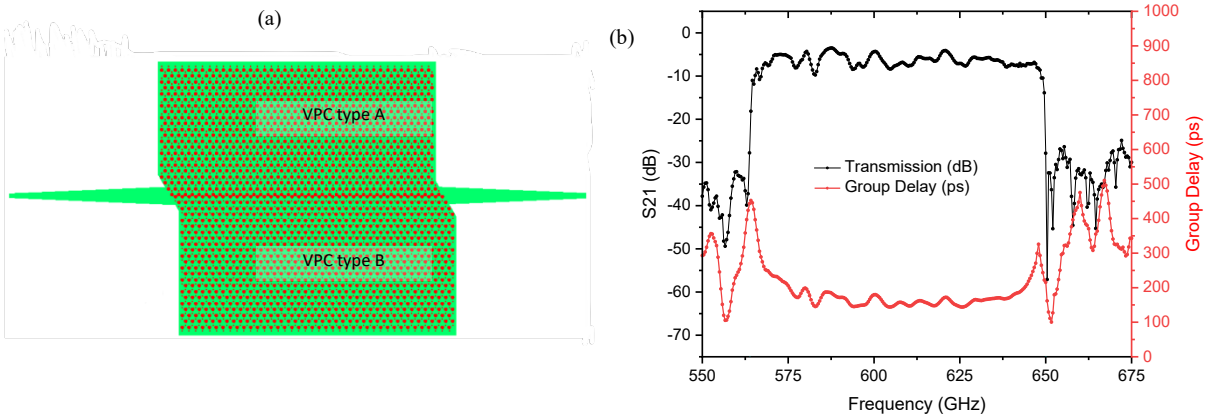

Figure IV.9:(a) Schematic of the device (b) Transmission and Group Delay measured from VNA of topological waveguides with round holes and bearded interface

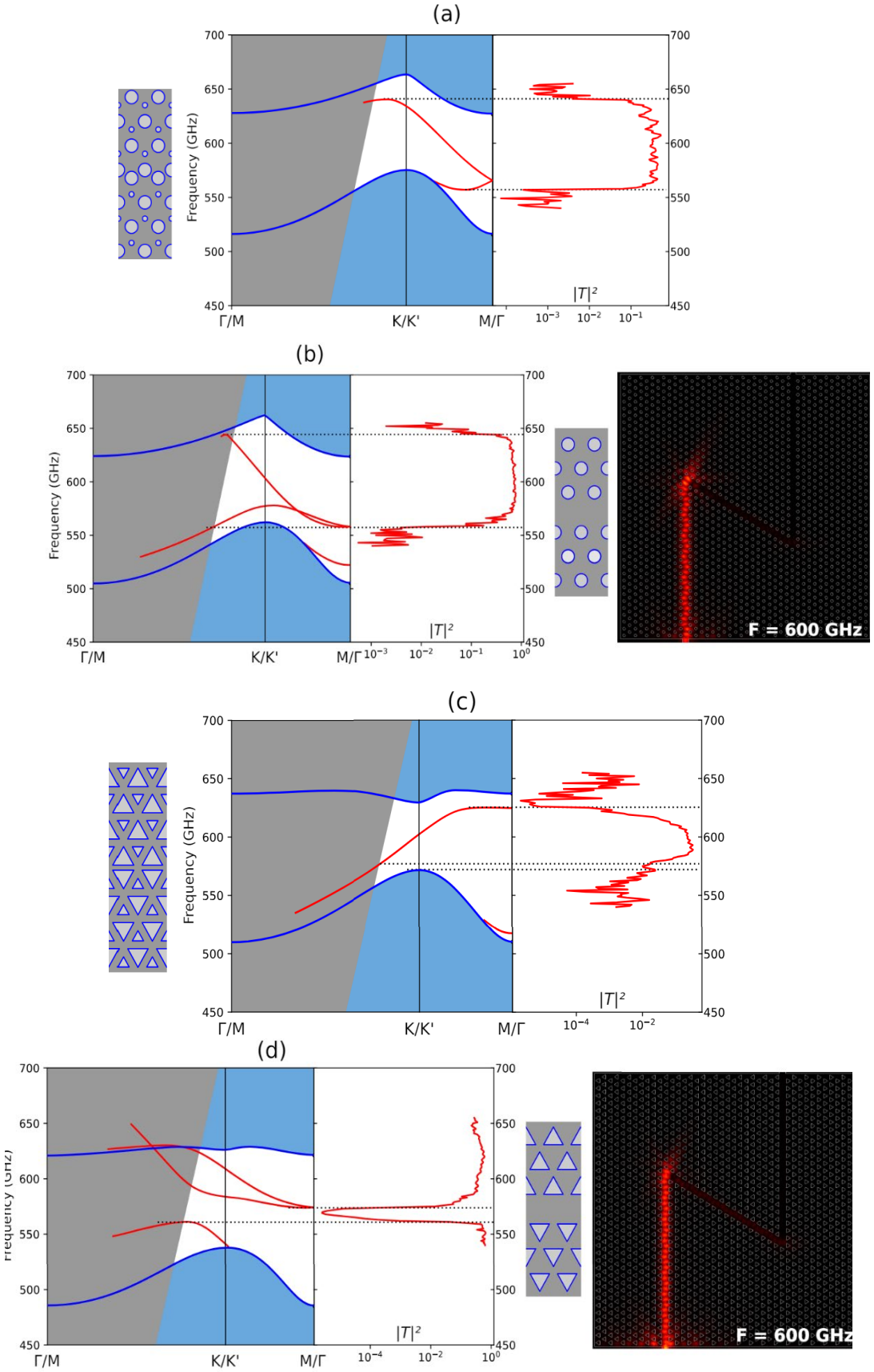

Figure IV.10: (a) Simulated transmissions for topological waveguides with round holes and (b) photonic crystal waveguides with periodic round holes in hexagonal lattice with line defect as waveguiding part. (c) Simulated transmissions for topological waveguides with triangular holes and (d) photonic crystal waveguides with periodic triangular holes in hexagonal lattice with line defect as waveguiding part.

IV.2.2 Photonics-enabled 1.04-Tbit/s Aggregated Data rate in the 600-GHz-band.

In this section, we showcase the effectiveness of a waveguide-integrated THz photodiode in the 600 GHz band, combined with a waveguide-based receiver. This combination allows for wide available bandwidth and enables us to achieve an aggregated data rate beyond 1 terabit per second. Moreover, we were able to maintain a bit-error-rate performance that complies with the standard error-correction limits. This achievement sets a new milestone for THz communications. Later on, we utilized this Waveguide integrated THz photodiode to measure the Datacom of our Topological Functions.

IV.2.2.1 Transmitter and Receiver Description

The THz transmitter used here is based on a unitravelling carrier (UTC) photodiode integrated for the 600-GHz-band [5]. The structure of the lab-made photomixer was previously reported in [7]. Fig. IV.11 shows typical performance of this photomixer, measured with a waveguide power-meter (PM5 from VDI [8]) and associated with a waveguide taper from WR1.5 to WR10. This photomixer has a 3-dB bandwidth beyond 250 GHz. The receiver part is composed of a subharmonic mixer using GaAs schottky technology, with typical conversion losses of 10-12 dB. Fig. IV.11. shows the conversion losses of the mixer used in the receiver that shows a large overlap with the intrinsic bandwidth of the UTC-PD based transmitter. The testbed we used is detailed in section IV.1.3 in back -to-back configuration.

IV.2.2.2 Frequency Allocation Plan and Spectrum Measurement

In this section, the performance of the overall association is tested. In this configuration, a back-to-back configuration (transmitter and receiver directly connected each other) is tested to assess the maximum performance of the association. As per the results shown on Fig. IV.11, a frequency allocation plan is proposed to use the full bandwidth of the system, described in Table IV.I, with the carrier frequencies, baud-rate (BR) and occupied bandwidth (OBW).

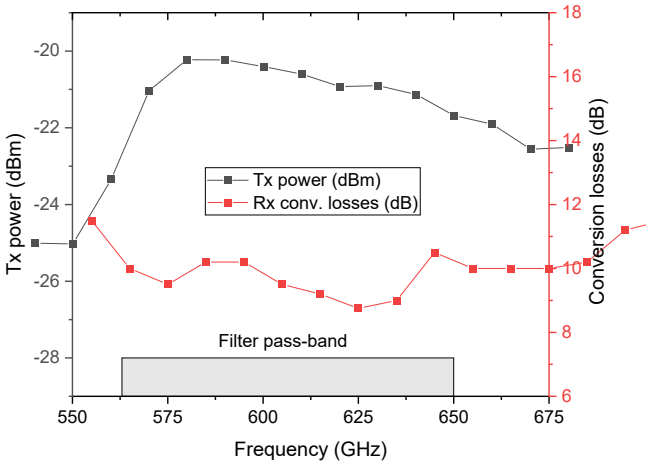

Figure. IV.11. Power performances of the transmitter and receiver conversion losses in the frequency of interest. Filtering pass-band window measured from VNA is set as a reference.

F	Frequency, GHz		OBW	BR
GHz	Min	Max	GHz	GB
500	496.5	503.5	7	3.5
508	504	512	8	3.5
520	513.75	526.25	12.5	12
535	528.75	541.25	12.5	12
550	541.75	558.25	16.5	15
569	559	579	20	19
590	580	600	20	19
610	600	620	20	18.5
632	620.5	643.5	23	20
655	645	665	20	18
675	665	685	20	19
695	685.5	704.5	19	19
712	704.5	719.5	15	14
724	720.5	727.5	7	6

TableIV.1: 600 GHz band Frequency Allocation Plan

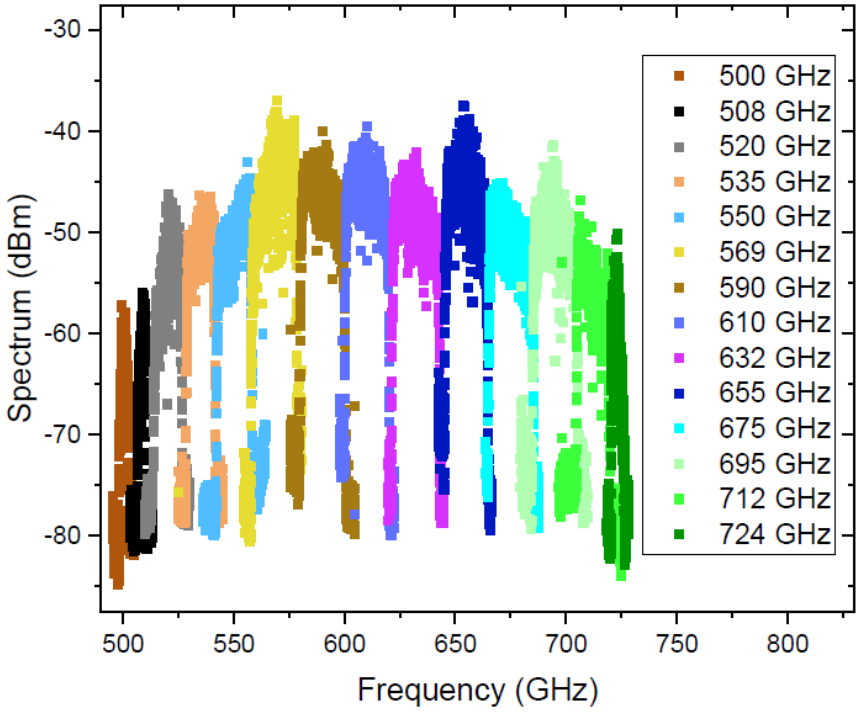

Figure. IV.12. Measured spectra, from IF analysis, at oscilloscope input.

Fig.IV.12 presents the measured spectrum, measured each carrier at a time, the overall spectrum is then aggregated to check the isolation between channels.

IV.2.2.3 BER/EVM Performances

Each channel was tested with different modulation formats. Considering the bit error-rate limits for soft-decision forward-error correction (SD-FEC) of 2E-2 (0.02), and hard decision (HD) FEC of 2E-3 (0.002), the system was settled to reach a performance below SD-FEC and HD-FEC. The results are shown in Tables II and III, respectively. The overall data rate of the system is 1.04 Tbit/s (SD-FEC compatible) and 887.5 Gbit/s (HD-FEC compatible). These figures are corresponding to the Fig. IV.13 and Fig. IV.14, respectively.

F	Case 1	BER	Mod. Type	EVM
GHz	DR	SD-FEC comp.	-	%
500	14	0.0042	QAM-16	12
508	14	0.0069	QAM-16	12.3
520	48	0.00049	QAM-16	10
535	72	0.0083	QAM-64	5.8
550	75	0.0008	QAM-32	6
569	95	0.00068	QAM-32	5.9
590	114	0.006	QAM-64	5.5
610	111	0.008	QAM-64	5.7
632	120	0.0076	QAM-64	5.7
655	108	0.0073	QAM-64	5.8
675	95	0.001	QAM-32	6.2
695	95	0.0029	QAM-32	6.8
712	56	0.0007	QAM-16	10.2
724	24	0.000303	QAM-16	9.5
1.041 Tbit/s aggregated data-rate				

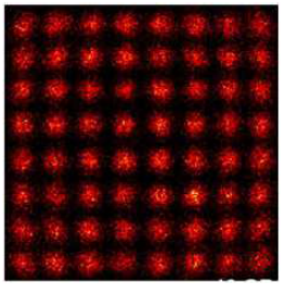

CH.4
535 GHz
72 Gbit/s

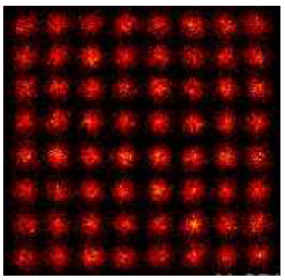

CH.9
632 GHz
120
Gbit/s

Table IV.2: BER/EVM Performance, SD-FEC Compatible

F	Case 2	BER	Mod. Type	EVM
GHz	DR	HD-FEC comp.	-	%
500	-	-	-	-
508	-	-	-	-
520	48	0.00049	QAM-16	10,0
535	60	0.00037	QAM-32	5.7
550	75	0.0008	QAM-32	6,0
569	95	0.00068	QAM-32	5.9
590	95	0.00026	QAM-32	5.5
610	92.5	0.00056	QAM-32	5.6
632	100	0.00045	QAM-32	5.7
655	90	0.00039	QAM-32	5.8
675	76	0.0000035	QAM-16	6.8
695	76	0.000018	QAM-16	7.9
712	56	0.0007	QAM-16	10.2
724	24	0.000303	QAM-16	9.5
887.5 Gbit/s aggregated data-rate				

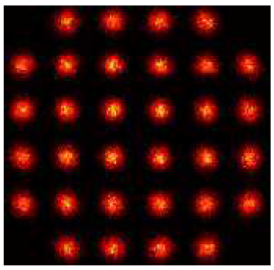

CH.10
655 GHz
90 Gbit/s

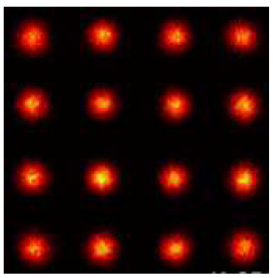

CH.12
695 GHz
76 Gbit/s

Table IV.3: BER/EVM Performance, HD-FEC Compatible

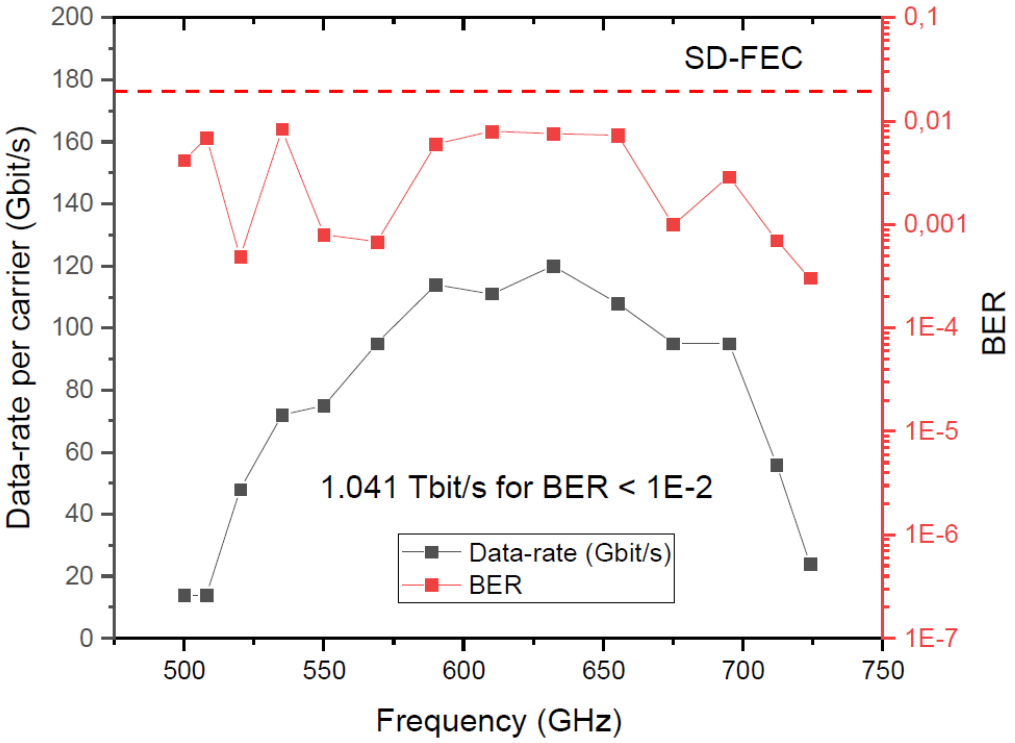

Figure. IV.13: System performance, with a SD-FEC compliance (ie all BER < 1E- 2) and aggregated data-rate of 1.041 Tbit/s.

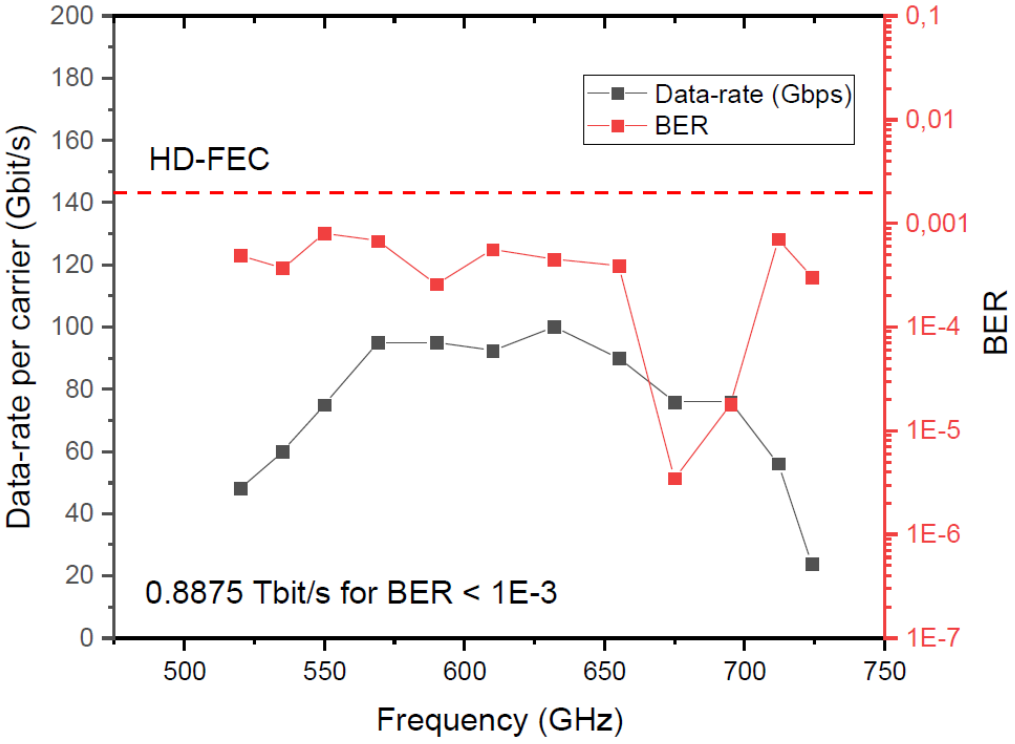

Figure. IV.14: System performance, with a HD-FEC compliance (ie all BER < 1E-3) and aggregated data-rate of 0.8875 Tbit/s.

IV.2.2.4 Single Channel Analysis at 632 GHz

From the measurement shown in Fig. IV.10, the best carrier frequency of the association of the UTC-PD and the SHM receiver was 632 GHz. For this channel, a single carrier analysis, with ultra-wideband modulation was tested. Thanks to the wide bandwidth of the testbed, the system was tested up to 185 Gbit/s (46.25 GBaud, QAM-16) and 200 Gbit/s (40 GBaud, QAM-32). Corresponding BER values are shown by Fig. IV.15, and Fig.IV.16 shows the I/Q map of the fastest QAM-32 tested.

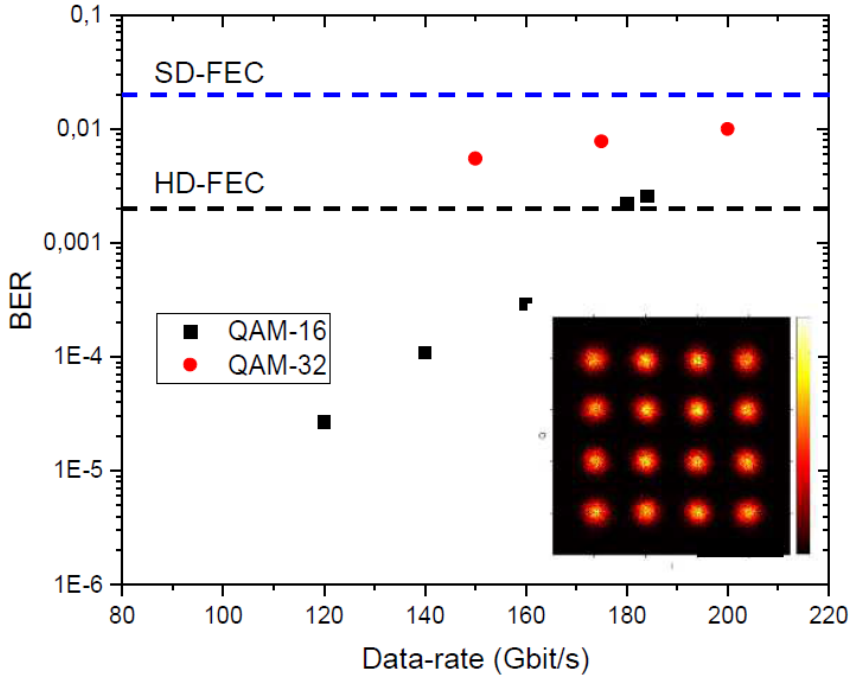

Figure. IV.15: Ultra-wideband single channel performance in the 600 GHz band: HD-FEC 180 Gbit/s using QAM-16, and SD-FEC compliant 200 Gbit/s. UTC-PD current is in that case 7.5 mA for all measurements. Inset shows 160 Gbit/s QAM-16, 2.9E-4 BER.

The combination of a wideband optical testbed optimized for THz communications, a > 250-GHz bandwidth UTC-PD in the 600-GHz-band and state-of-the art electronic receiver is proposed. Leveraging the linear and wideband nature of the whole testbed, we demonstrated a multi-channels approach to open new research opportunities for THz communications beyond the 300-GHz-band.

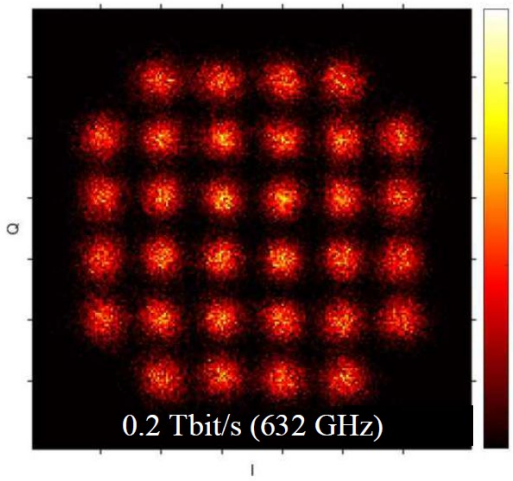

Figure IV.16: I/Q map of single channel 0.2 Tbit/s at 632 GHz. BER is 1E-2, below SD-FEC limit.

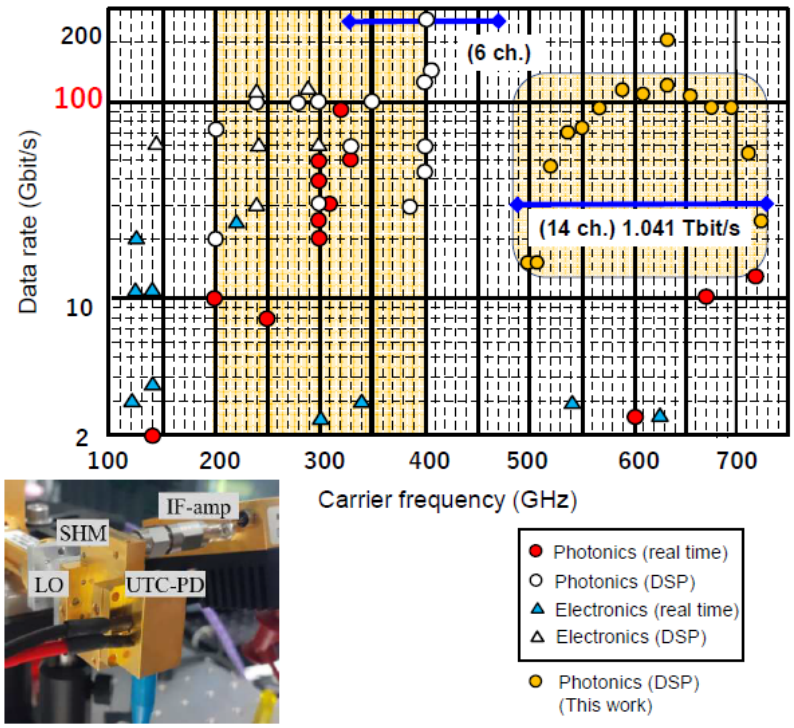

Figure.IV.17: Benchmark of the data-rate demonstrated using single carrier frequencies in the range 100-750 GHz. The photonics-electronics association in the WR1.5 shown here open new research routes for the use of the 600 GHz band. Inset: view of the UTC-PD module connected to the SHM.

This is, to the best of our knowledge, the highest ever reported data-rate in the 600-GHz-band, and the first aggregated data-rate beyond 1 Tbit/s using a THz system while maintaining a FEC compliant performance. The use of photonics approach also enabled here to showcase the highest ever reported single channel data, as high as 0.2 Tbit/s for a carrier frequency of 632 GHz. The perspective of this work is to use of this system within a wireless link.

IV.2.3 120 Gbit/s aggregated channel transmission in the 600 GHz band using topological waveguide.

We have measured data com experiments using topological waveguides with Sharp edges VPCs with round holes and bearded interface since it provides wide bandwidth from 570-650 GHz. We have used the same experimental setup shown in Fig IV.4. The THz transmitter and the receiver used the same as in the previous section *IV.2.2.* We demonstrate a THz 3x40 Gbit/s data transmission within the 600 GHz band. Bit-error-rate performance is compliant with standard error-correction techniques limits, setting building blocks for THz communications in the 600 GHz region. The transmission is realized through a silicon-on-insulator platform with a Valley photonic crystal design at a bearded interface. Furthermore, the realized sample shows very sharp passband filter features, paving the way for new THz signal processing functionalities.

IV.2.3.1 Back-to-back and filtered signals performances

To assess the filter performance with modulated signals, the back-2-back performance is first measured. This corresponds to the direct connection of the WR1.5 waveguides, ie at UTC-PD output and WR1.5 input of the SHM. For QPSK and QAM16, the error vector magnitude (EVM) is measured versus the relative power emitted at the transmitter side, corresponding to Fig. IV.20 and Fig. IV.21. respectively. The topological filter's input port taper was inserted into a probe extender that connected to the UTC-PD via metallic hollow-core WR 1.5 waveguide at the Tx side. The VPC output port taper was interfaced to the GaAs Schottky sub-harmonic mixer (SHM). The down-converted signal is amplified (30 dB, SHF-810 [9]) and detected by a wideband oscilloscope for modulated signal analysis, namely error vector magnitude (EVM) thanks to the use of the vector signal analysis (VSA) tool [10] and bit error rate (BER) measurement.

The Fig. IV.18 shows the frequency allocation plan. The 3 channels are used to test the filter inside the bandwidth. For each frequency (585, 610, and 635 GHz), 2 modulation formats were tested: Quadrature Phase Shift Keying (QPSK) and quadrature amplitude modulation with 16 symbols (QAM16), using 10GB. The whole testbed is presented in Fig. IV.5. And the view of the testbed is shown in Fig.IV.19.

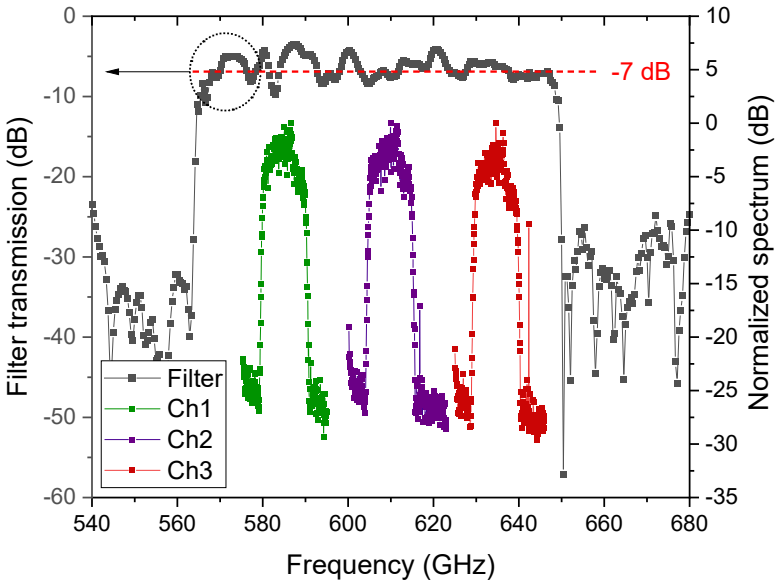

Figure.IV.18: Spectrum shows the frequency allocation plan. The 3 channels used to test the filter inside the bandwidth. With central frequency 585, 610 and 635 GHz, inside the broad transmission window of topological waveguide.

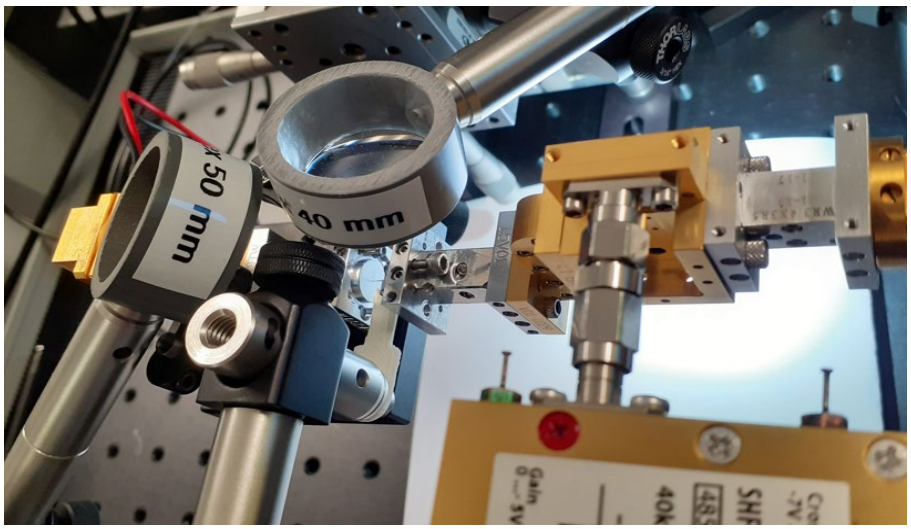

Figure. IV.19: Experimental View of the 600GHz datacom testbed

Ch	Freq (GHz)	QPSK Penalty	QAM16 Penalty
1	585	6.8 dB	6.8 dB
2	610	4.7 dB	5.6 dB
3	635	7 dB	7.3 dB

Table IV.4: Measured power penalties for all tested channels, in QPSK and QAM16 cases.

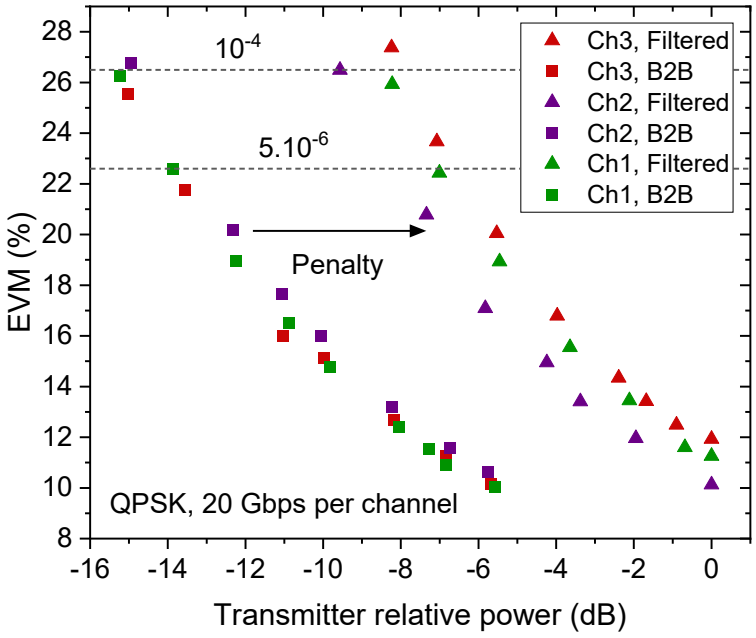

Figure IV.20: EVM power curves for B2B and filtered wideband channel, in QPSK 10 GB (20 Gbit/s) per channel

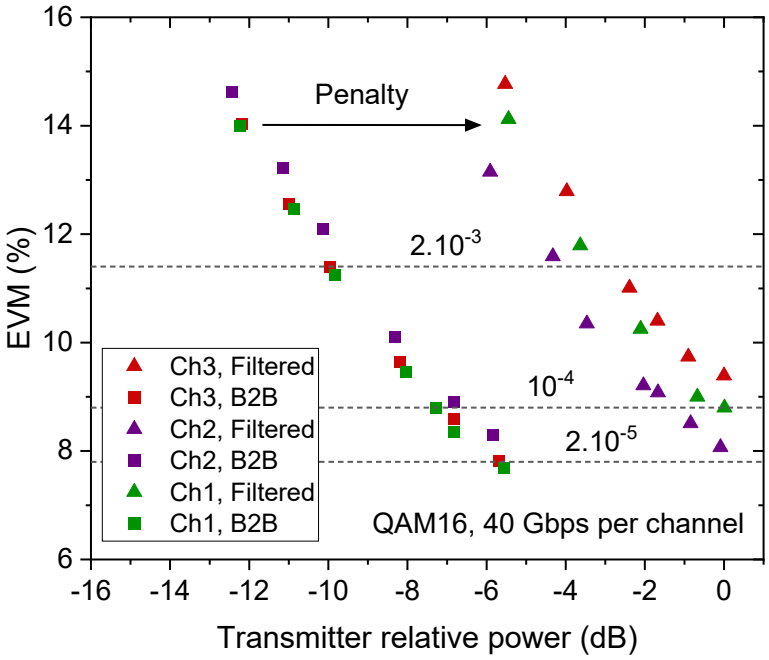

Figure.IV.21: EVM power curves for B2B and filtered wideband channel, in 10 GB QAM16 (40 Gbit/s) per channel.

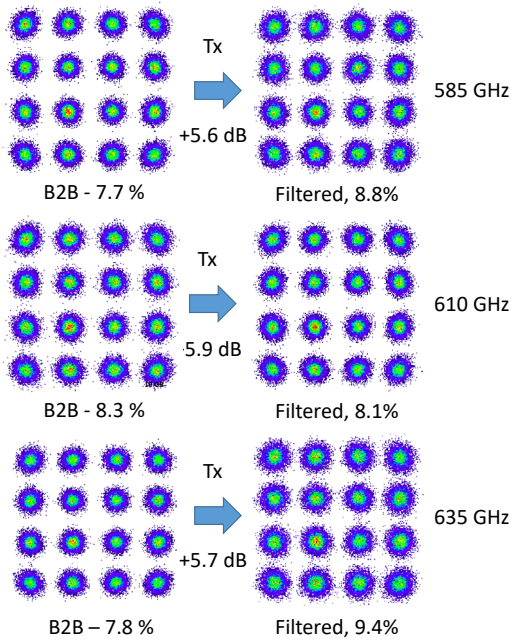

Figure. IV. 22: QAM16 constellations examples for 585, 610, and 635 GHz, 40 Gbit/s, in B2B and filtered configurations

The study evaluates the performance of three frequency channels, Ch1, Ch2, and Ch3, under back-to-back and filter configurations using QPSK and 10 GB QAM16 modulation schemes. The symbol rate remains constant at 10 GBd throughout the experimentation. Fig IV.20 displays the EVM vs Power curves for QPSK modulation, showcasing the relationship between error magnitude and power across various photocurrent levels. Additionally, Fig IV.21 presents the data points obtained with tuning photocurrents for the three channels under both back-to-back and filter configurations for 10 GB QAM16 modulation. These curves provide critical insights into signal quality and modulation scheme performance under different setups. The dashed lines give some Bit Error Rate levels for some specific EVM values.

The achieved data rates are 20 Gbit/s per channel for QPSK modulation and 40 Gbit/s per channel for QAM16 modulation. Constellation diagrams for all three channels, depicted in Fig IV.22, further elucidate the modulation schemes' performance by illustrating the arrangement of the symbols in the complex plane (IQ map). Table IV.4 comprehensively overviews the measured power penalties for all tested channels, considering both QPSK and QAM16 cases. These penalties are assessed based on the -7dB transmission window measured from VNA characterization, providing valuable insights into signal degradation and system performance across different configurations and modulation schemes. In summary, the study thoroughly analyzes the performance of multiple frequency channels under varying configurations and modulation schemes. We experimentally show that up to 3x40 Gbit/s can be manipulated in the proposed structure. The use of a topology approach for the 600 GHz band seems to be promising for future 600 GHz band communication systems. Through EVM vs. Power curves, constellation diagrams, and power penalty assessments, the research sheds light on signal quality, throughput, and system optimization possibilities, laying a foundation for further advancements in high-speed communication systems.

IV.20.4 THz topological ring Resonator

To experimentally demonstrate breaking topological protection in valley photonic crystals enables tunable passive functions, we fabricated and topological ring resonator with the two extreme designs of topological protection simulation shown in Fig II.14. Here we explain

experimental measurements, that is the transmission and group delay of the fabricated designs in detail.

IV.2.4.1 Transmission and Group Delay- triangular holes

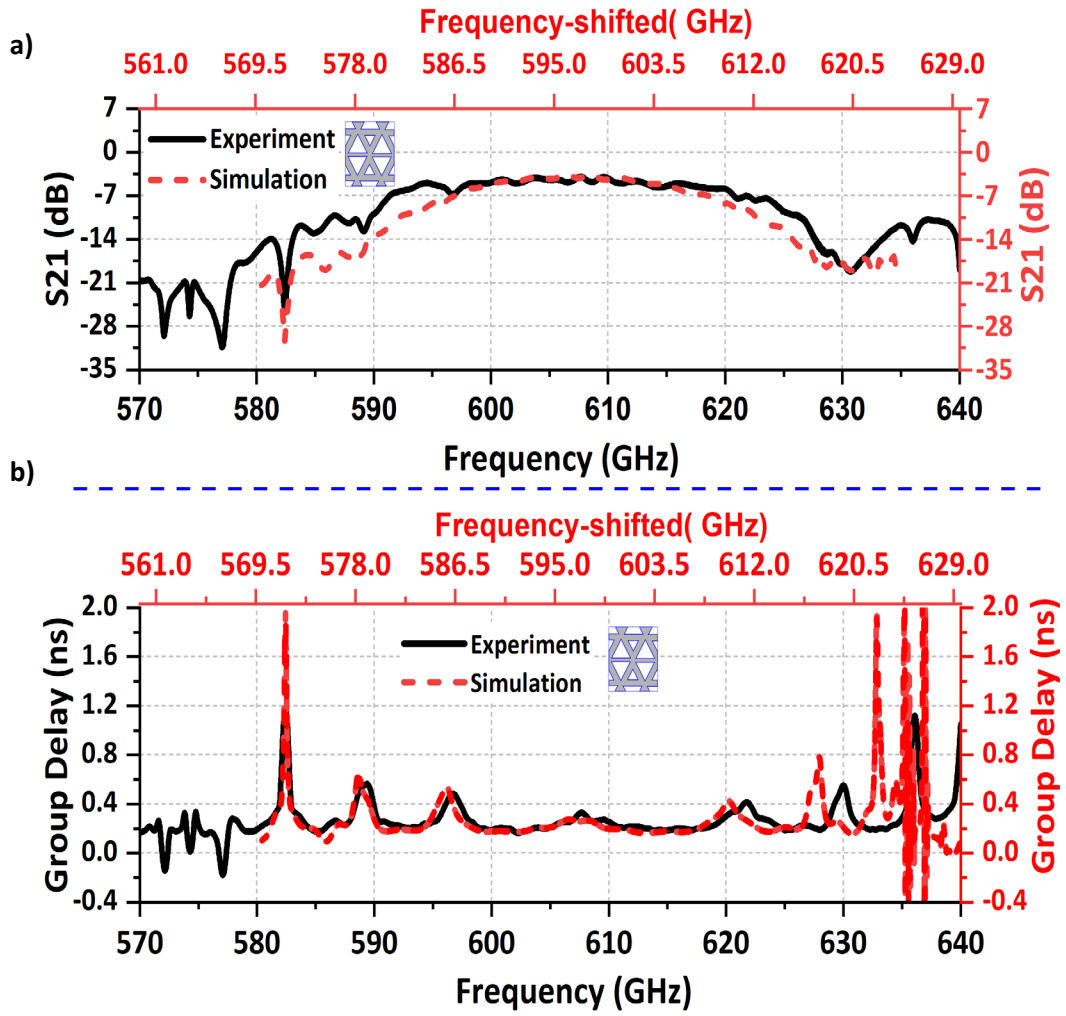

Figure. IV.23(a) Transmission (black) from Vector Network Analyzer (VNA) measurement and simulation (red) for THz topological ring resonator fabricated using triangle holes and zigzag interface (b) Group delay from VNA measurement for the same design.

The measured S_{21} transmission and group delay for the devices are shown in Fig. IV.23(a), for both THz topological ring resonator designs with zigzag and bearded interfaces using triangular holes. The transmission and group delay curves in all cases include simulation curves, which have been aligned with experimental curves by plotting them with a constant 10 GHz frequency shift. Fig. IV.23. displays the frequency-shifted x-axis at the top (red axis).

The S21 transmission exhibits sharp dips (peaks) at 582.38 GHz and several broader dips with a relatively low Q factor. The smooth profile of the S21 over the 590-610 GHz range implies that this design provides relatively high topological protection and resilience towards backscattering at the corners. The computed group delay from complex phase data measured on VNA for these devices is shown in Fig. IV.23(b). A peak of 1.5 ns is spotted corresponding to the dip of 582.38 GHz in the transmission spectrum. Other small peaks are revealed in this measurement at frequencies corresponding to the eigenfrequencies of the topological cavity. The data shows low dispersion in the 600-620 GHz spectrum, confirmed by simulation Fig. II.14(a), while group delay remains quite flat within the 590-610 GHz range. Despite a 10 GHz low-frequency shift, the numerical and experimental results align well. This means that the fabrication imperfections are negligible and the observed resonances arise from the triangular hole geometry. The average value of time delay in the central frequency of the spectrum center at 610 GHz is 0.25 ns. The relatively low dispersion in the central part of the frequency spectrum is due to the topological protection scaled up by the VPC design.

IV.2.4.2 Transmission and Group Delay- Circular holes

We now study triangular resonators fabricated using circular holes with bearded domain interfaces. Fig. IV.24(a) shows several sharp transmission dips at specific frequencies which include 573.4, 579.64,593.36, 601, 610, and 618.2 GHz. Notably, the transmission dip at 593.36 GHz exhibits a Q factor of approximately 34900. The observed double peaks at 601 and 610 GHz are a result of backscattering at the corners of the triangular resonator, displayed in more detail in Fig. IV.25. The frequency difference between the two splits in the double peaks is $\Delta F' = 0.43$ GHz for the peaks at 601 GHz, and $\Delta F'' = 0.6$ GHz for the peaks at 610 GHz. The double peaks are accurately replicated in the simulated data, perfectly matching the experimental verification, except for the constant 10 GHz low-frequency shift and for the resonance at 593 GHz which shows negative τ_g in the experiment but positive τ_g in the simulation. We now discuss the origin of these two discrepancies. The constant low-frequency shift of about 10 GHz between the numerical results and the experiments can be attributed to small differences in the membrane thickness and silicon dielectric constant, but most probably to the simulation mesh, whose size has to be limited by the resources needed for those simulations (about 10^7 degrees of freedom, a typical RAM of 180GB and between 5 to 10 days of computation for one spectrum). Despite this constraint, the number and shape of the peaks

is well reproduced, together with the frequency evolution of the group delay τ_g, whose values are almost the same as in the experiments.

The Free Spectral Range (FSR), which is the frequency spacing between two adjacent resonances, is a crucial parameter in the design of such resonators. The FSR of approximately 8 GHz is calculated for the dips in the central part of the spectral window which is also the case in the simulated spectrum. The central part of the spectrum displays a sharp negative delay of -2.6 ns corresponding to the high Q factor dip at 593.36 GHz.

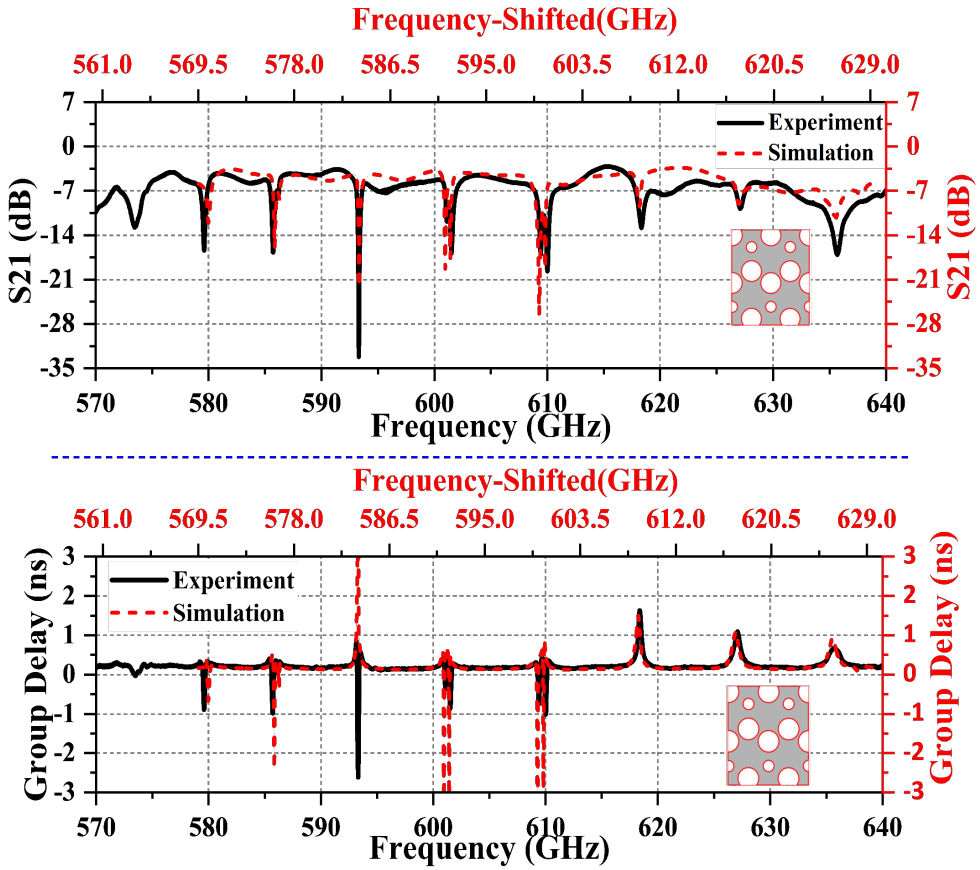

Figure. IV.24 a) Transmission (black) from VNA measurement and simulation (red) for THz topological ring resonator fabricated using VPC design with the bearded interface and circular holes (b) Group delay from VNA measurement.

The double delay peaks at 601 and 610 GHz frequencies are also refined from the simulation figure. The overall group delay in the transmission regions without peaks closely approaches zero as on Fig. IV.24(b) aligning with the simulation data where zero delay is also observed. By utilizing a bearded interface and circular air holes combination in the THz topological ring resonator can achieve high Q factor peaks through the downscaling of topological protection. This design is well-suited for highly compact and efficient sensors, optical switches, filters, modulators, and quantum information processing due to its ability to provide narrow peaks

with a high Q factor. Thus, we can confirm that scaling down topological protection as a parameter enhances the Q factor, making it advantageous for sensing and filtering applications.

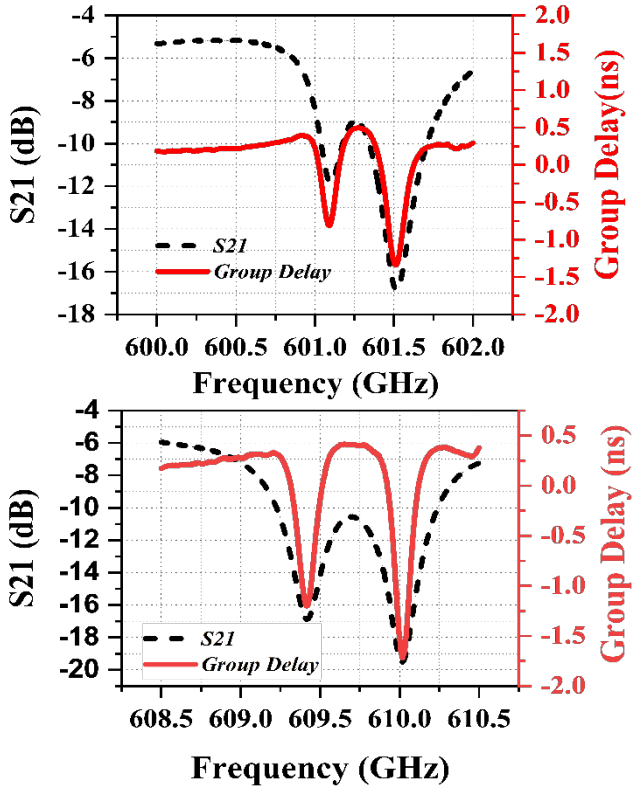

Figure. IV. 25: Transmission and group delay for the Double peaks at 601 GHz and at 610 GHz from VNA measurement for THz triangular ring resonator with bearded interface and circular holes.

The measured negative delay of -2.6 ns corresponding to the high Q factor dip at 593.36 GHz is not present in the simulation. The reason is that experimental imperfections make that resonance very deep (see Fig. IV.24(a)) with a high amount of energy stored, also part of it leaks out through the sides of the device. Over all we seen that by utilizing a bearded interface and circular air holes in the ring resonator, we can implement high Q factor peaks through the downscaling of topological protection. This design is well-suited for highly compact and efficient sensors, optical switches, filters, modulators, and quantum information processing due to its ability to provide narrow peaks with a high Q factor. Thus, we can confirm that scaling down topological protection as a parameter enhances the Q factor, making it advantageous for sensing and filtering applications.

IV.2 THz topological double cavity Resonator

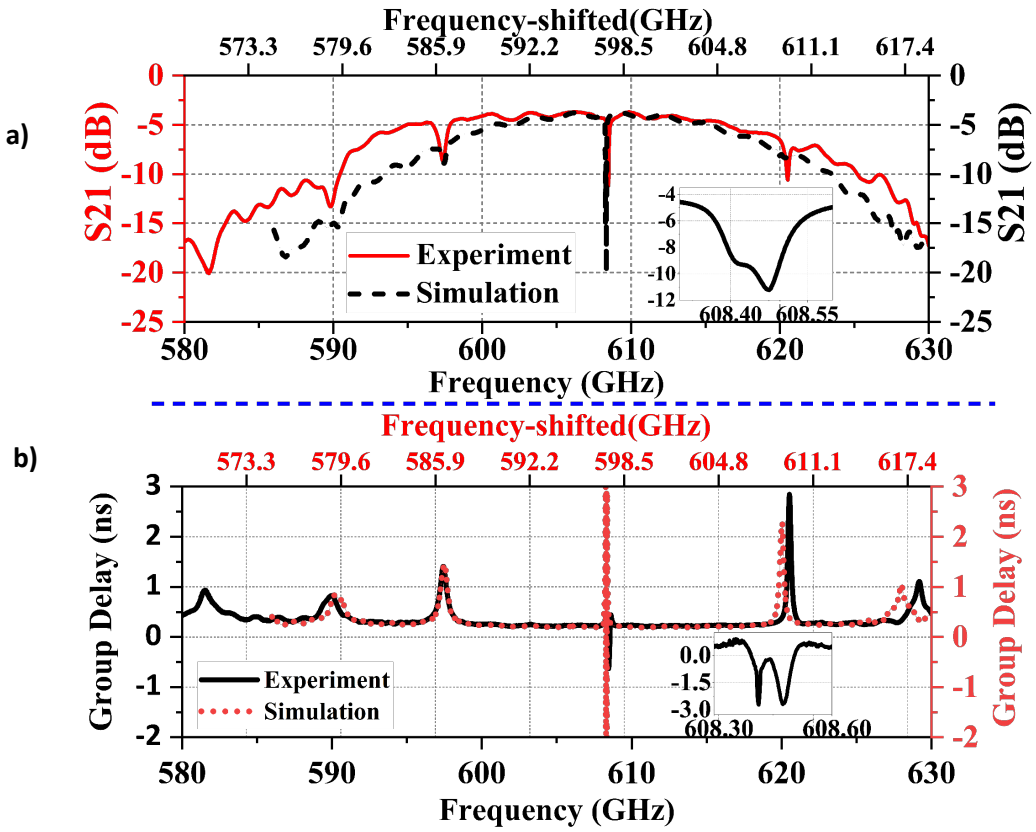

Figure. IV.26 (a) Transmission from VNA measurement for the topological double cavity resonator. Inset shows the double peak at 608 GHz (b) Group delay from VNA measurement for the topological double cavity resonator. Inset shows the double peak at 608 GHz

Fig. IV.26 shows the experimental validation of the double cavity device The design and Simulation results of the Double Cavity resonator are shown in section II.2.4. Again, the comparison with the experiment shown in Fig.IV.26(a) is very good, despite the frequency shift of about 10.2 GHz. However, the width of the peaks of the split resonances is larger in the experimental transmission. The reason is that the two underlying peaks overlap: the lowest-frequency peak appears as a shoulder of the high-frequency peak, but the frequency interval is consistent with simulations. Similarly, the experimental group delay is in good agreement for the single peak resonances but strongly differs in amplitude for the double peak, where it reaches about –2.7 ns. Those differences are the signature of additional losses in the experimental device, which could be attributed to the small homogeneities of the shape of holes, or to a lower resistivity of the of silicon, which was not taken into account in the simulations.

Conclusion of this chapter

The chapter presents experimental results on robust topological waveguides, which include designs with triangular and round hole configurations. The results show that straight waveguides featuring round holes act as band gap filters, and these designs are effective in data communication (Datacom) experiments. The chapter also explains how the degree of topological protection can be used to scale passive functionalities within photonic crystal designs. This concept is demonstrated through the examination of two distinct topological ring resonator designs. In designs featuring zigzag interfaces and triangular air holes, the robustness of edge modes is demonstrated, whereas designs incorporating circular air holes and bearded interfaces exhibit relaxed protection. The diminished topological protection observed in triangular topological cavities with circular air holes and bearded interfaces presents an opportunity for engineering high Q factor resonances, which holds promise for filtering and sensing applications. Furthermore, the chapter marks the first experimental validation of passive functionalities within the 600 GHz band, which paves the way for advancements in high-speed 6G data communication technology.

References

[1] Zhang, H., Krooswyk, S., & Ou, J. (2015). High speed digital design: design of high speed interconnects and signaling. Elsevier.
[2] "Vector Network Analyzer Extension Modules (VNAX)." https://www.vadiodes.com/en/spectrum-analyzer-extension-modules-sax.
[3]Akiki, E. (2021). Integrated SOI photoacoustic gas sensor at THz frequencies for food quality control application (Doctoral dissertation, Université de lille).
[4] M. A. Pulido-Gaytán, J. A. Reynoso-Hernández, J. R. Loo-Yau, A. Zárate-de Landa and M. d. C. Maya-Sánchez, "Generalized Theory of the Thru-Reflect-Match Calibration Technique," in IEEE Transactions on Microwave Theory and Techniques, vol. 63, no. 5, pp. 1693-1699, May 2015, doi: 10.1109/TMTT.2015.2417860.
[5] T. Nagatsuma, T. Kurokawa, M. Sonoda, T. Ishibashi, M. Shimizu, and K. Kato, '600-GHz-band Waveguide-output Uni-traveling-carrier Photodiodes and Their Applications to Wireless Communication', in 2018 IEEE/MTT-S International Microwave Symposium - IMS, Philadelphia, PA: IEEE, Jun. 2018, pp. 1180–1183. doi: 10.1109/MWSYM.2018.8439226.
[6] Tsuruda, K., Fujita, M., & Nagatsuma, T. (2015). Extremely low-loss terahertz waveguide based on silicon photonic-crystal slab. *Optics express*, *23*(25), 31977-31990.
[7] T. Kurokawa et al., "Over 300 GHz bandwidth UTC-PD module with 600 GHz band rectangular-waveguide output". Electron. Lett., vol. 54:pp. 705-706, 2018. https://doi.org/10.1049/el.2018.0932.

[8] J. Webber et al., "Terahertz Band Communications With Topological Valley Photonic Crystal Waveguide," IEEE-JLT, vol. 39, no. 24, pp.7609-7620, 15 Dec.15, 2021, doi: 10.1109/JLT.2021.3107682.

[9] SHF-810, available on-line: accessed June 29th, 2023. https://www.shfcommunication.com/wp-content/uploads/datasheet_shf_810.pdf
[10] VSA/Pathwave software. Available on-line, accessed March 9th,2024 https://www.keysight.com/zz/en/lib/resources/software-releases/89600-vsa-2023.html

Conclusion and perspectives

Topological photonics is an emerging field that focuses on engineering the flow of light through novel means. With the help of topological protection, the surface modes of topological photonic systems have intriguing properties, such as unidirectional propagation, and robust transmission against defects and disorders. These properties meet the growing demands for information processing. In this thesis, we introduce a design for passive functionalities that operate in the terahertz (THz) frequency range of 600 GHz. These functionalities have promising applications in future technologies such as augmented reality and virtual reality enabling 6G data communication and beyond.

Silicon based valley photonic crystals (VPCs) are topological photonic systems that not only support protected surface modes but are also compatible with micro-nano fabrication. This makes them ideal for constructing high-performance photonic devices or even photonic integrated circuits [1]. In our thesis, we explore the degree of topological protection experienced by the robust edge modes in valley photonic crystals. We focus on interfacial topological interfaces, which is a relatively new perspective worth exploring. We use CMOS-compatible HR-Si for fabricating our VPC designs to ensure the feasibility of manufacturing and integrability towards highly integrated THz integrated Circuits.

We started by demonstrating straight waveguides at 600 GHz using the same fabrication procedure used at 300 GHz [2]. This was done to ensure the robustness of valley edge modes at higher frequency ranges. To experimentally verify the scalability of topological protection, we demonstrated the performance of THz topological ring resonators and THz double cavity resonators designed for operation in the 600 GHz frequency region. This work showcased how the scaling of topological protection can be achieved by utilizing a combination of air hole geometry and interfacial degrees of freedom. This provides functional tuning of devices at the chip level. We also demonstrated how straight topological waveguides act like sharp-edged filters in the 570-640 GHz band. We used this wide bandwidth to validate datacom. To the best knowledge, we were the first to report the validation of topological devices for THz communication in the 600 GHz frequency range. The achieved results related to each of these devices and measurement results are summarized in the coming paragraphs.

Waveguides with compact sizes are necessary to transmit electromagnetic energy over long distances with low losses. Such components may be required for any application in the THz domain. After a detailed review of THz waveguides, it has been realized that topological waveguides with Valley kink states, characterized by linear dispersion and single-mode operation, have surpassed the performance of typical photonic crystal waveguides in terms of operational bandwidth and overall loss. This was confirmed by record data rates of 108 Gbit/s that were reported in 2021 by Webber et al. for 10-mm topological waveguides [3]. This underscores the potential of topological structures for high-data-rate communication applications at chip level, fabricated in a CMOS-compatible HR-Si platform. In our work, we successfully demonstrated topological straight waveguides with valley edge modes at 600 GHz using the VPC unit cells with triangular air holes and the zigzag interface between two types of VPCs using the HR-Si platform [4]. Transmission measured with the experiment and simulated one for the designs are closely aligned and promising. Some frequency shift in the experimental curve is found, typically around 9.8 GHz, which is less than 2% of the central frequency. Such deviations are quite common in real-world scenarios, like variations on dielectric constant or wafer thickness. Group delay measurements were taken for the frequency range of 580 GHz to 620 GHz and the values obtained were less than 0.2 ns. It was also found that the group delay increases with waveguide length. Similarly, although we expected a length increase of 9.2 mm, 14.2mm, and 19.2 mm, we could not distinguish a clear transmission decrease by using the transmission curves. This means that the overall losses are dominated by the injection losses from the input and output tapers. The results proved that topological valley kink states are promising for THz communication applications enabling high-speed 6G data transfer systems.

We have designed topological straight waveguides that incorporate VPCs with round holes and bearded termination between VPC type A and Type B. We measured the transmission and group delay data and found that the spectrum displayed sharp ends and a wide bandwidth of 570-650 GHz at the edges, which was surprising. To determine the cause, we conducted further simulations and discovered that the design is very similar to Effective medium-cladded dielectric waveguides which were already reported for wide band-width [5], with the only difference being asymmetry in the hole structures and terminations. Hence, we realized that the sharp edges and wide bandwidth were not a result of the topological property but rather the photonic crystal design. However, it's an advantage in topological design that the modes are immune to defects and robust in the wide bandwidth compared to the normal photonic crystal

design with line defects that give wide bandwidth. Hence, we decided to utilize this wide bandwidth to demonstrate datacom measurements for the first time in this frequency region. We used a waveguide-integrated THz photodiode in the 600 GHz band, combined with a waveguide-based receiver system. Uni-traveling-carrier photodiodes (UTC-PDs) are packaged with WR-1.5 rectangular metallic waveguides to ensure 600-GHz band operation.

Leveraging on the high bandwidth provided by the module we considered the association of a photonics-based THz source and an electronic receiver, showing an aggregated data rate beyond 1 Tbit/s. To the best of our knowledge, this is the first-ever reported experiment for a Tbit/s THz system with FEC-compliant performances [6]. The photonics approach also enabled showcasing the highest ever-reported single-channel data, as high as 0.2 Tbit/s for a carrier frequency of 632 GHz. Then, as an application of the module, we successfully measured the topological filters for the 600 GHz band. After design and fabrication on SOI, the filter was fully characterized and validated inside a 600 GHz communication system. We experimentally showed that up to 3x40 Gbit/s can be manipulated in the proposed structure. Hence, we confirmed the use of a topological approach for the 600 GHz band seems to be promising for future 600 GHz band communication systems.

Ring resonators are essential components of integrated photonic circuits because they can perform multiple functions such as acting as filters, sensors, and delay lines as well as enhancing nonlinear optical effects [7]. By using different VPC air hole geometries, such as triangular and round air holes permuted with two interface terminations - zigzag and bearded - between VPC type A and B, we simulated edge modes in all four cases. Based on our findings, we proposed that a partial breakup of topological protection can be useful in designing on-chip passive functionalities. We observed that VPC composed of the permutation of triangular air holes with zigzag termination provides more topological protection, while round holes with bearded interface provide the least topological protection. We did membrane simulations for these combinations and fabricated these two structures and also fabricated those structures to validate experimentally. The S21 transmission of the triangular holes with a zigzag interfaced resonator exhibits sharp dips (peaks) at 582.38 GHz and several broader dips with relatively low Q factor. The smooth profile of the S21 over the 590-610 GHz range implies that this design provides relatively high topological protection and resilience toward backscattering at the corners. Other small peaks are revealed in this measurement at frequencies corresponding to the eigenfrequencies of the topological cavity. Despite a 10 GHz low-frequency shift, the

numerical and experimental results align well. This means that the fabrication imperfections are negligible, and the observed resonances arise from the triangular hole geometry. The average value of time delay in the central frequency of the spectrum center at 610 GHz is 0.25 ns. The relatively low dispersion in the central part of the frequency spectrum is due to the topological protection scaled up by the VPC design.

We also studied triangular resonators fabricated using circular holes with bearded domain interfaces. We found several sharp transmission dips at specific frequencies, including 573.4, 579.64, 593.36, 601, 610, and 618.2 GHz. The transmission dip at 593.36 GHz exhibits a Q factor of approximately 34900. The observed double peaks at 601 and 610 GHz are a result of backscattering at the corners of the triangular resonator. Therefore, it is clear that using a bearded interface and circular air holes combination in the THz topological ring resonator can achieve high Q factor peaks through the downscaling of topological protection. This design is well-suited for highly compact and efficient sensors, optical switches, filters, modulators, and quantum information processing due to its ability to provide narrow peaks with a high Q factor. Scaling down topological protection as a parameter enhances the Q factor, making it advantageous for sensing and filtering applications.

The simulated transmission spectrum and group delay of the THz topological double-cavity resonator reveal two distinct features: a shallow minimum near 587 GHz and a sharp split resonance at 597.3 GHz. The frequency interval between these minima is significantly lower than that of single-cavity resonances. This split-resonance is attributed to backscattering occurring at both splitters along the edge. The negative group delay observed in simulations is due to leakage in air at the edge of the device. Experimental validation shows good agreement, despite slight frequency shifts and differences in peak width and group delay amplitude, likely due to small inhomogeneities in hole shapes or lower silicon resistivity not accounted for in simulations. These findings underscore the need for further investigation into device fabrication and material properties to optimize performance in practical applications. Even though we used a highly topologically protected combination that is triangular air holes with zigzag terminations for the design, the newly created edge contributed to the split-resonances

which is visible in the experiment also. This double cavity resonator is a clear validation to use of topological protection as a lobe to tune passive functionalities.

Hence this thesis aimed and actually contributed to research on the use of topological phases of light for future THz applications and contributed to applications related to THz and photonics community in various perspectives as explained in earlier paragraphs.

References

[1] J.-W. Liu et al., 'Valley photonic crystals', Advances in Physics: X, vol. 6, no. 1, p. 1905546, Jan. 2021, doi: 10.1080/23746149.2021.1905546.

[2] Y. Yang et al., 'Terahertz topological photonics for on-chip communication', Nat. Photonics, vol. 14, no. 7, pp. 446–451, Jul. 2020, doi: 10.1038/s41566-020-0618-9.

[3] J. Webber et al., 'Terahertz Band Communications with Topological Valley Photonic Crystal Waveguide', J. Lightwave Technol., JLT, vol. 39, no. 24, pp. 7609–7620, Dec. 2021, Accessed: Apr. 23, 2024. [Online]. Available: https://opg.optica.org/jlt/abstract.cfm?uri=jlt-39-24-7609

[4] A. S. Mohammed et al., 'THz topological Waveguides in 600 GHz frequency Region', in 2023 48th International Conference on Infrared, Millimeter, and Terahertz Waves (IRMMW-THz), Sep. 2023, pp. 1–2. doi: 10.1109/IRMMW-THz57677.2023.10298871.

[5] W. Gao, X. Yu, M. Fujita, T. Nagatsuma, C. Fumeaux, and W. Withayachumnankul, 'Effective-medium-cladded dielectric waveguides for terahertz waves', Opt. Express, OE, vol. 27, no. 26, pp. 38721–38734, Dec. 2019, doi: 10.1364/OE.382181.

[6] T. Nagatsuma, T. Kurokawa, M. Sonoda, T. Ishibashi, M. Shimizu, and K. Kato, '600-GHz-band Waveguide-output Uni-traveling-carrier Photodiodes and Their Applications to Wireless Communication', in 2018 IEEE/MTT-S International Microwave Symposium - IMS, Philadelphia, PA: IEEE, Jun. 2018, pp. 1180–1183. doi: 10.1109/MWSYM.2018.8439226.

[7] W. Bogaerts et al., 'Silicon microring resonators', Laser & Photonics Reviews, vol. 6, no. 1, pp. 47–73, Jan. 2012, doi: 10.1002/lpor.201100017.

List of Publications

JOURNAL PUBLICATIONS

- Mohammed, A. S., Lévêque, G., Lebouvier, E., Pennec, Y., Faucher, M., Amo, A., Szriftgiser, P., & Ducournau, G. (2024). Breaking topological protection in valley photonic crystals enables tunable passive functions for THz 6G communications and beyond. *Journal of Lightwave Technology*, manuscript submitted (March, 2024), under revision, (May 2024).

- Abacıoğlu, E., Mohammed, A. S., Tebart, J., Grzeslo, M., Neerfeld, T., Fernández Estévez, J. L., Ducournau, G., & Stöhr, A. (2024). 100 Gbit/s IEEE 802.15.3d and Beyond THz Communication Links Using a Broadband Waveguide-Integrated MUTC-Photodiode. *IEEE Journal of Lightwave Technology*, manuscript submitted.

- Surya Revanth Ayyagari, Andreas K. Klein, Simonas Indrišiūnas, Vytautas Janonis, Daniil Pashnev, Abdu Subahan Mohammed, Guillaume Ducournau, Andreas Stöhr, and Irmantas Kašalynas, "Broadband high-contrast-grating-type waveplates for the terahertz range," Opt. Express 32, 15870-15881 (2024).

ORAL PRESENTATIONS AND POSTERS

- Guillaume Ducournau, Pascal Szriftgiser, Yuma Kawamoto, Weijie Gao, Abdu Subahan Mohammed, et al. Photonics-enabled 1.04-Tbit/s Aggregated Data rate in the 600-GHz-band. 2023 Asia-Pacific Microwave Conference (APMC 2023), Dec 2023, Taipei, Taiwan. pp.327-329. 10.1109/APMC57107.2023.10439923, hal-04506661.
- Abdu Subahan Mohamed, Edouard Lebouvier, Gaëtan Lévêque, Yan Pennec, Marc Faucher, et al. THz topological Waveguides in 600 GHz frequency Region. 2023 48th International Conference on Infrared, Millimeter, and Terahertz Waves (IRMMW-THz), Sep 2023, Montreal, Canada. ⟨10.1109/IRMMW-THz57677.2023.10298871⟩. ⟨hal-04277479⟩
- E. Abacıoğlu, M. Grzeslo, T. Neerfeld, A. S. Mohammed, J. L. Fernández Estévez, G. Ducournau, and A. Stöhr, "500 GHz Operational Bandwidth MUTC-Photodiodes with Milliwatt Terahertz Output Power Levels," in 49th European Conference on Optical Communications (ECOC), October 2023.
- Mohammed, A. S., Lebouvier, E., Lévêque, G., Amo, A., Pennec, Y., Szriftgiser, P., Ducournau, G., & Faucher, M. (2022). Low Loss Topological Silicon Valley Photonic Crystal Waveguides in Terahertz Regime. In APROPOS 18 Conference 2022, Vilnius, Lithuania.